JOINT EUROPEAN TORUS

JET–P(96)33

Many Authors

JET Papers presented at the 23rd EPS Conference on Plasma Physics and Controlled Fusion (Kiev, Ukraine, 24-28 June 1996)

JET Papers presented at the 23rd EPS Conference on Plasma Physics and Controlled Fusion (Kiev, Ukraine, 24-28 June 1996)

Many Authors

JET-Joint Undertaking, Culham Science Centre, OX14 3DB, Abingdon, UK

Preprint of Paper to be submitted for publication in
the proceedings of the 23rd EPS Conference on Plasma Physics and Controlled Fusion

Plasma movement at ELMs in JET

S. Ali-Arshad, A. Edwards, J. Lingertat, S. Puppin, J. Wesson

JET Joint Undertaking, Abingdon, Oxon. OX14 3EA, UK

INTRODUCTION

In JET giant ELMs can give rise to a sustained degradation of plasma confinement, and in some cases control of the vertical position of the plasma is lost following a giant ELM, leading to a major disruption. An example of such a case is given in fig. 1.

A variety of measurements suggest that during the ELM the scrape-off layer and bulk plasmas move rapidly. This paper presents these observations, and addresses implications for the vertical stability of the plasma.

DATA ANALYSIS

Magnetic diagnostics show a short-lived perturbation appearing during the ELM, typically in the range 10-100 Gauss. The example in fig. 2 shows the amplitudes of the modes with toroidal mode number n=0,1,2,3, calculated from a toroidal array of coils at a poloidal position of θ~60°. The poloidal structure of the perturbation is shown in fig. 3 at two time slices. A dominant m=1 structure is seen. The amplitude of this structure is a factor of ~3 larger than the level of perturbation observed on each of the coils in the toroidal array at θ~60°, suggesting a principal mode with m=1, n=0. Thus during the ELM the plasma shifts downwards, reaching its lowest position in several hundred microseconds, and then it moves upwards reaching its highest position in about a millisecond. Interpretation of soft X-ray data during ELMs is complicated by transient, highly local radiation sources. However, supporting evidence for the plasma movement is given by lines of sight not intercepting such sources. The position of the plasma current centroid, as determined from the current moment method, is shown in fig. 4. This supports the observation of a downward movement followed by an upward movement, and indicates the size of the movement is ±1cm. Fig. 4 also shows that during the downward movement little poloidal flux penetrates through the vessel. The plasma boundary displacement can therefore be calculated from flux compression between the plasma boundary and the wall: $\delta z_{down} \approx \Delta Z_0 \, \delta B_\theta / B_{\theta 0}$, where ΔZ_0 =initial plasma-wall distance, δB_θ = change in B_θ at top of vessel, $B_{\theta 0}$ = equilibrium field at top of vessel. The upward movement can also be estimated by this method, but is only accurate to a factor of ~2, due to partial flux penetration (see fig. 4). Such estimates give agreement with the centroid calculation, so that the perturbation might be approximated with a 'rigid body' displacement. In addition, this procedure allows the

movement to be determined from more abundant dB_θ/dt data. Fig.5 shows such estimates for several ELMs plotted against the D_α light intensity. These suggest that larger ELMs can produce larger displacements, and that the upward overshoot is typically larger than the downward movement, by a factor of ~2.

Fig.6 shows infra-red camera data on the divertor target before and during an ELM, showing an increase in the strike zone separation during the ELM. The change is too large to be a result of the bulk plasma movement described above, so the existence of SOL currents is suggested. This is supported by Langmuir probe measurements of SOL currents of order 10kA, intercepted by the divertor target during ELMs [1]. A toroidal current of order 10kA, transferred from the main plasma current is also predicted by consideration of spilling of hot electrons into the SOL during an ELM [2].

INTERPRETATION

The vertical speed of the JET plasma is stabilised by a control system. A simplified model for this has been given [3], [4]. This has the form $I_pZ_p \approx \frac{C_1V_R}{s(s-\gamma)} + \frac{C_2f_z(s+1/\tau_{eff})}{s-\gamma}$, Z_p = plasma current centroid vertical position; V_R = voltage to radial field coil, proportional to plasma speed, allowing for amplifier characteristic (±10kV max., 9 levels); γ = natural instability growth rate; τ_{eff} = effective radial field penetration time with divertor configuration; f_z = arbitrary vertical force applied to plasma. For an ELM with a 1:2cm down:up movement ratio, the model suggests a force waveform f_z as in fig. 7 (The plasma position is restored by a position control system on a time-scale of several milliseconds. This is not included in the simulation.) Scaling up this f_z waveform by a factor of ~3 produces a vertical instability in the model as shown in fig. 8. The forces on the plasma might arise from toroidal current transferred to the SOL during an ELM. Away from the X-point, to first order, this does not produce a force on the plasma. However, in the X-point region a downward force would be produced, as illustrated in fig. 9. If the SOL current then decays faster than the current recovers in the confined plasma, e.g. due to an impurity influx, an upward force could be generated due to the weaker poloidal field near the X-point compared with the top of the plasma.

FUTURE WORK

Further work is needed in diagnosing the SOL currents, understanding the resultant forces and the effect on the strike zones. The ELM database studied needs to be expanded, and data from soft X-ray and infra-red cameras, Langmuir probes and magnetics need to be correlated. A multi-machine scaling study of the movement would be valuable to assess implications for ITER.

ACKNOWLEDGEMENT:

ACKNOWLEDGEMENT:

The authors would like to thank Dr. P. Noll for discussions on the vertical stabilisation system.

REFERENCES

[1] J. Lingertat et. al., Studies of giant ELM interaction with the divertor target in JET, J. Nucl. Mater., to be published.

[2] J. Wesson, SOL Current During ELM, Private communication (1995).

[3] P. Noll and M. Garribba, Review of Fast Radial Field Amplifier, Private communication (1989).

[4] P. Noll, A simplified model of the stabilisation system, JET divisional note JDN/G(91)025, (1991).

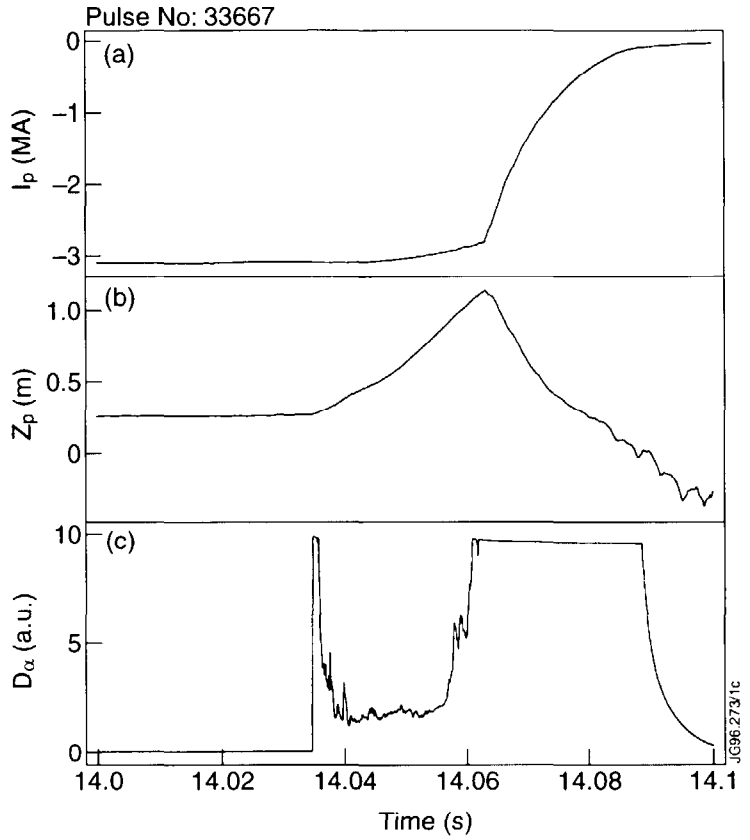

Fig. 1: Disruption of a 3MA plasma after loss of vertical stability following a giant ELM

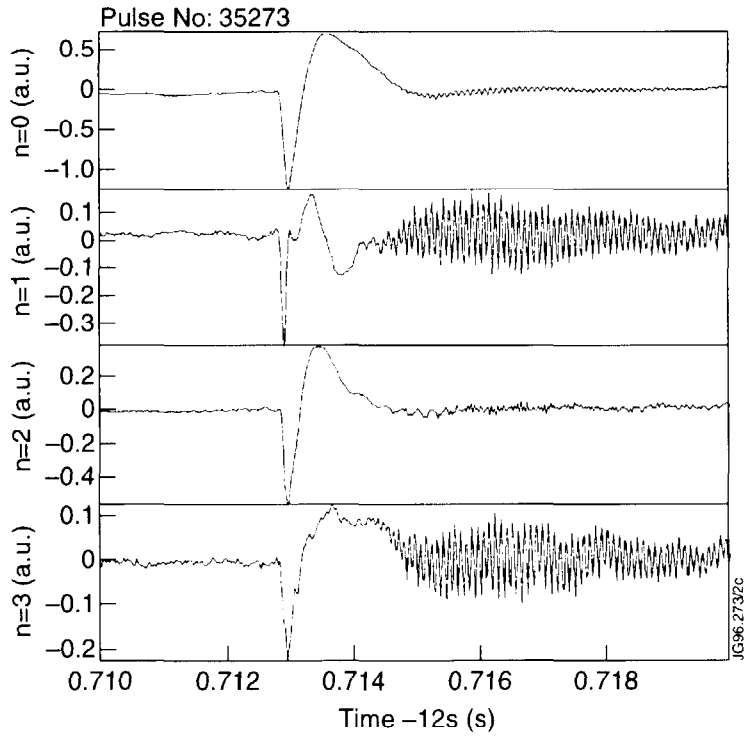

Fig. 2: Amplitudes of dB_θ/dt, with toroidal mode numbers n=0,1,2,3 at a poloidal position of θ~60°.

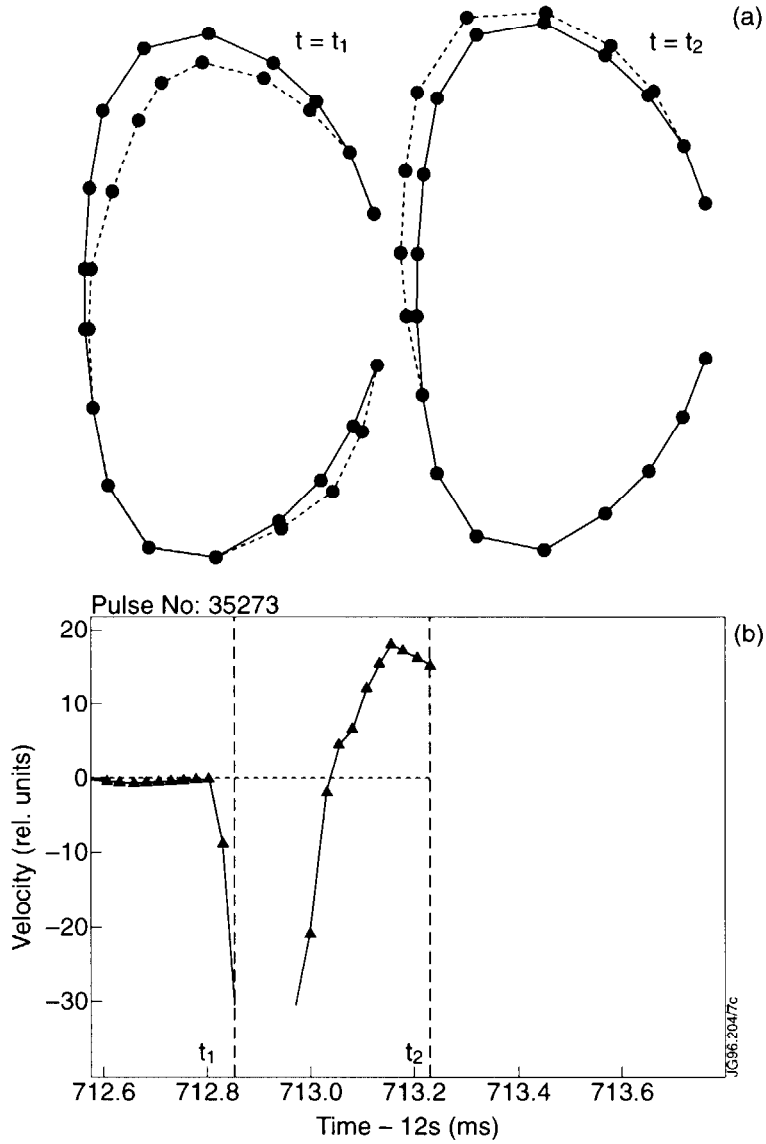

Fig. 3: (a) dB_θ/dt perturbation at two times during an ELM (see (b)). On fast time-scales (<<3ms) this is proportional to the local normal plasma speed.

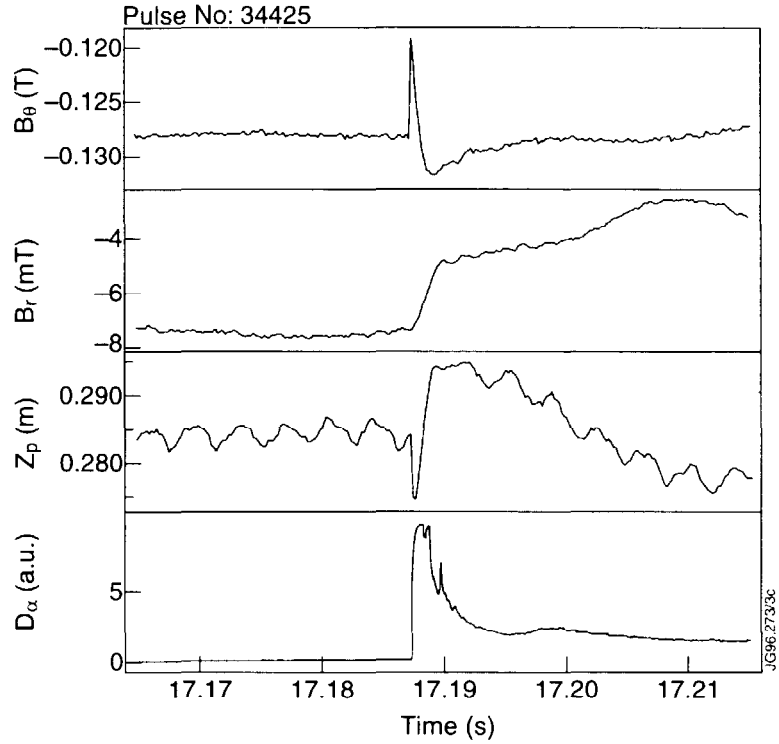

Fig. 4: (a) Poloidal field and (b) radial field at top of vessel, and the plasma current centroid (c), at an ELM.

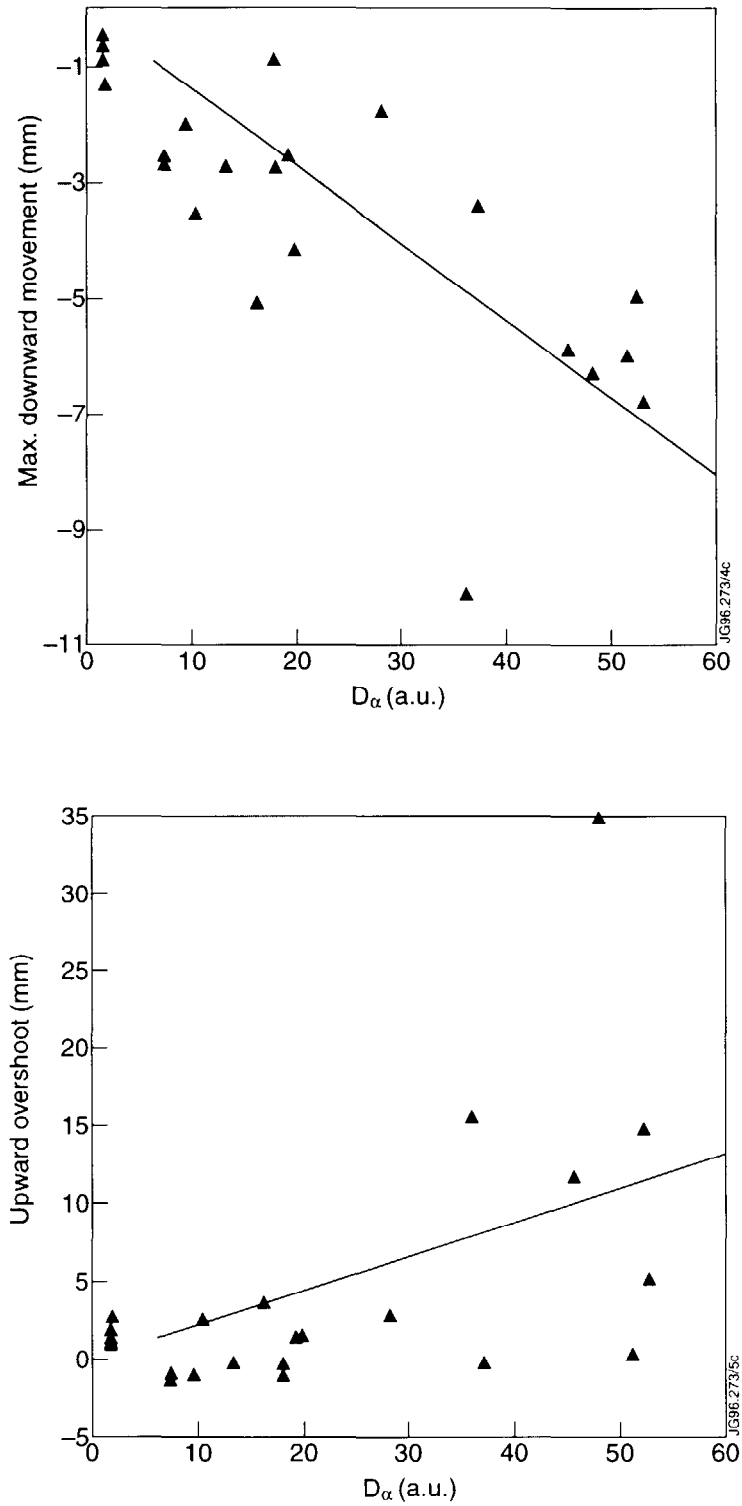

Fig. 5: Plasma displacement estimated from poloidal flux compression. The upward movement is likely to be underestimated by a factor of ~2, due to partial flux penetration.

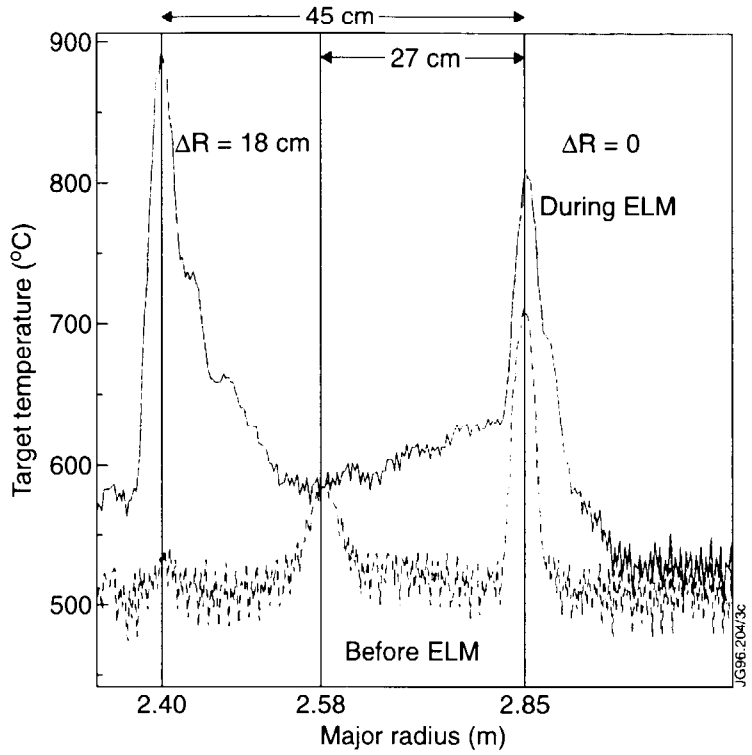

Fig. 6: Infra-red camera view of the divertor target before and during and ELM.

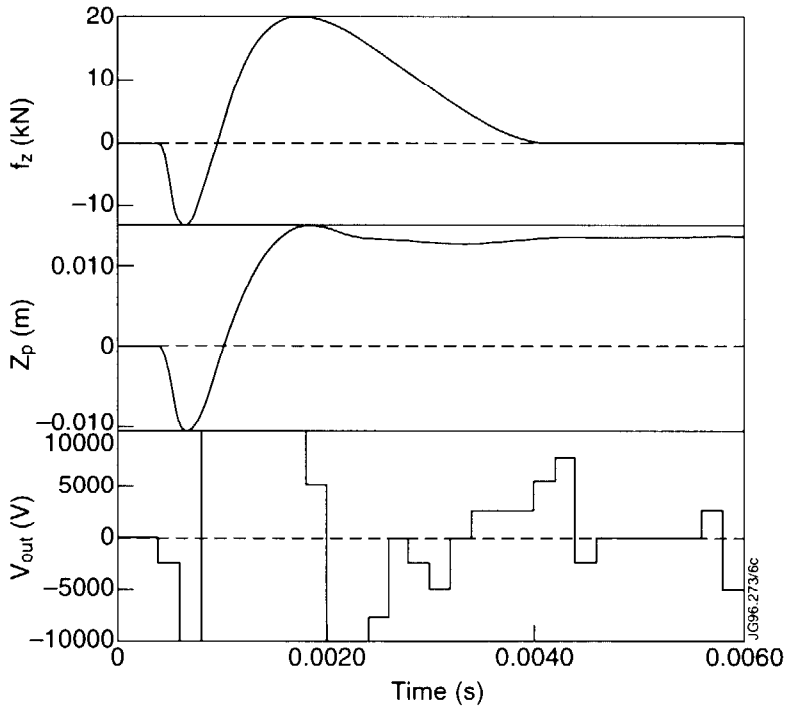

Fig. 7: Force required for typical plasma movement at a giant ELM, for a 3MA plasma with γ=700s^{-1}.

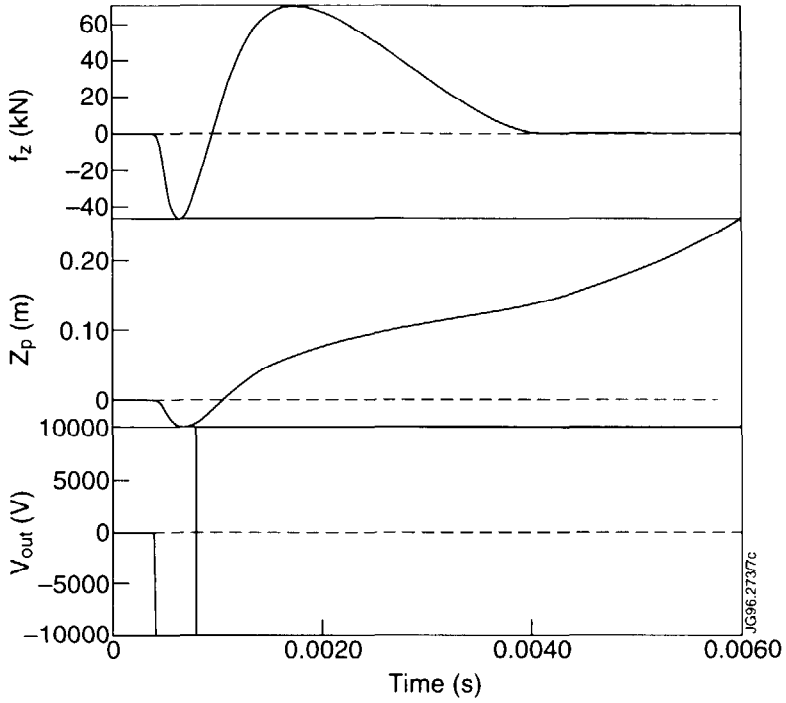

Fig. 8: Vertical instability produced by amplifying the force waveform found in fig. 7 by a factor of ~3.

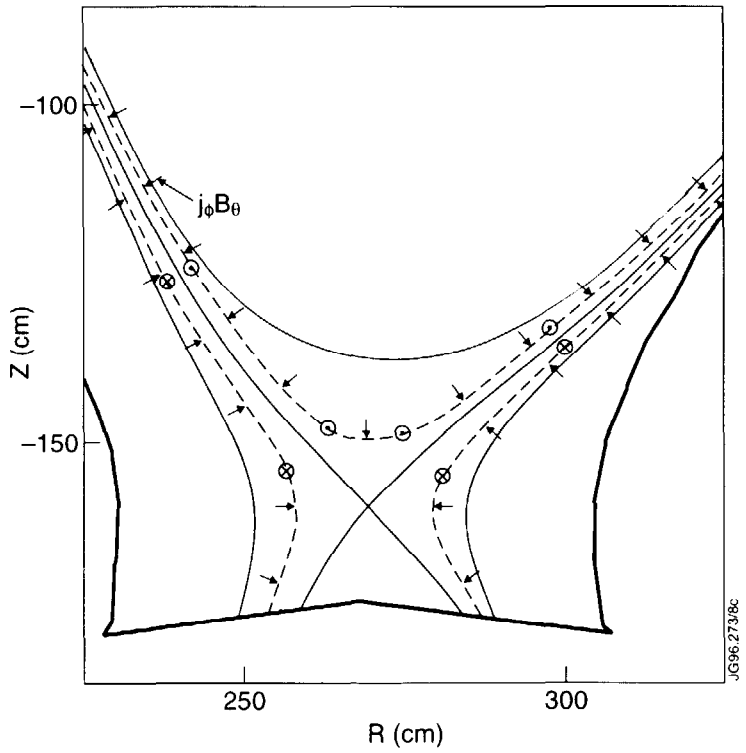

Fig. 9: Forces arising from toroidal current transfer from edge confined plasma to the SOL

Strong Asymmetries in Impurity Distributions of JET Plasmas

B. Alper, A.W. Edwards, R.Giannella, R.D. Gill, C.Ingesson,
M. Romanelli, J.Wesson, K-D.Zastrow

JET Joint Undertaking, Abingdon, Oxon. OX14 3EA, UK.

INTRODUCTION

A general feature observed during hot-ion H-mode discharges in JET has been a pronounced poloidal asymmetry in the soft X-ray (SXR) emission profiles with a distinct excess emission occurring on the outboard, low-field side. A tomographic reconstruction of one such plasma, using data from the new multi-camera SXR diagnostic[1] with 210 lines of sight and six independent views at one toroidal location, is shown in Figure 1. This figure clearly demonstrates this feature with a pronounced peak in the SXR emissivity beyond a major radius (R) of 3.5m. A similar phenomenon has been observed, in a less dramatic form in earlier JET plasmas [2], the effect being attributed to the centrifugal force on heavy (metal) impurities as a result of toroidal plasma rotation [3]. This feature is strongest at high toroidal velocities, which approach or even exceed the impurity ion thermal speed. These conditions occur in the hot-ion H-mode plasmas in which plasma rotation, driven by the neutral beams, reaches frequencies in excess of 18 kHz and where nickel impurities with temperatures in the range 10 - 15 keV are found. Also seen in Figure 1, in addition to this outboard peak, a second narrow peak is seen at, or close to, the magnetic axis. This is attributed to neo-classical diffusion of the metal impurities.

LASER ABLATION OF NICKEL

The peak in SXR emission at large major radii, shown in Figure 1, is attributed to line emission from metal impurities. A more quantitative study of this effect has been possible with controlled injection of nickel by laser blow-off during high performance discharges. In one such case, shot 34476, the nickel injection was performed early in the high performance phase of a hot-ion H-mode discharge. Figure 2 shows time traces of the concentration of nickel, together with its angular frequency and ion temperature from a high resolution X-ray crystal spectrometer.

The rise in nickel concentration is clearly seen at the time of laser ablation and reaches 4 parts in 10^4 . The Ni^{26+} emission used in these measurements is also the dominant source of line emission contributing to the SXR diode data. At the time of peak nickel concentration (12.96s) the nickel temperature is 11 keV corresponding to $v_{thermal} \sim 1.3 \times 10^5$ m/s with an angular

frequency of 110 krad./s corresponding to $v_{rot.} \sim 4x10^5$ m/s (at a radius of 3.6m). Thus the rotational velocity of the nickel is more than a factor of 3 greater than the thermal velocity.

Tomographic reconstruction of the SXR emission during this event has been performed using a pixel technique developed initially by C. Fuchs for JET bolometer data. In Figure 3 the SXR emissivity along a horizontal line through the magnetic axis is shown for several time slices. The background emission at 12.91s has been subtracted. The inward progress of the nickel occurs very rapidly following the ablation over a period of about 10-15ms and then essentially stops. The last time slice, over 400ms later, shows the development of a secondary peak at the plasma axis (probably due to neo-classical diffusion) with a minimum in emission occurring between the two peaks. This two peaked structure also often develops late into a conventional hot-ion H-mode discharge (e.g. Figure 1). In Figure 3 the peak emission is centred on the outboard equator at a major radius of ~3.6m; (the magnetic axis being at ~3.0m). Figures 4 shows a 3-dimensional view of SXR emission corresponding to the '+30ms' trace of Figure 3. Note that no up-down asymmetry is observed, unlike reference [3].

THEORY OF THE ASYMMETRY

The asymmetry in the SXR emission distribution arises because the impurities take up the toroidal rotation of the plasma and the resulting 'centrifugal force' throws the impurity ions outwards. The behaviour is complicated by the electrostatic field which arises to maintain quasi-neutrality in the plasma. Nevertheless, it is possible to set up simple equations to describe the system and in the case of low impurity content, to solve for the poloidal distribution of each impurity species. The feature which makes this problem tractable is that the poloidal distribution of impurities on a flux surface depends only on the equation of pressure balance parallel to the magnetic field in the poloidal plane. The balance of forces, in the simple case of a trace species with charge Z in a hydrogenic plasma, arises from the pressure gradient, centrifugal force and electrostatic field in a magnetic surface (Ψ). This can be represented by

$$T_Z \frac{dn_Z}{dR} = n_Z\left(m_Z\omega^2 R - eZ\frac{d\phi}{dR}\right)$$

where the derivatives are taken at constant Ψ.

Solving the set of equations for a pure deuterium plasma with a small addition of impurity (s) yields the ratio of impurity concentration between the outboard-(o) and inboard-(i) sides

$$\frac{n_s^o}{n_s^i} = \exp\left\{\frac{m_s\omega^2(R_o^2 - R_i^2)}{2T_s}f\right\} \text{ where } f = \left(1 - \frac{T_e}{T_i + T_e}\frac{m_i}{m_z}Z_s\right).$$

At the radius of peak nickel emission for shot 34476, T_e is ~5.5 keV at 12.94s and taking $T_i=T_s$ a value for f ~0.7 is obtained. This yields a value for the ratio of concentrations of 5.5±1:1. A further correction for the presence of other impurities in the plasma (carbon and beryllium) reduces this ratio by around 20%. (See [2] and references therein). Experimentally, from Figure 3 a value of 4±1 : 1 is found, in good agreement with theory.

A numerical simulation of the poloidal distribution of the nickel emission has been carried out for one time slice using these equations. The outboard radial distribution through the magnetic axis was taken from the data at 12.94s. The model results are shown in Figure 5 and compare well to the data of Figure 4.

SUMMARY AND CONCLUSIONS

Strong in-out asymmetries are observed in the soft X-ray emission from JET hot-ion H-mode plasmas, a peak being observed on the outboard side. The key feature of the asymmetry can be explained by the effect of the centrifugal force on metal impurity ions in these rapidly rotating plasmas, where their rotational velocities exceed their thermal velocities by a factor of three. A simple model developed for the poloidal distribution produces quantitative agreement with data from a discharge in which there was laser ablation of nickel into the plasma. The radial distribution of impurity ions with a stationary peak at R~3.6m and the subsequent development of a secondary peak on axis is less well understood.

REFERENCES

[1] Alper B. et al, 21st EPS Conference on Controlled Fusion and Plasma Physics, Montpellier, 1994, Vol.III p1305

[2] Giannella R. et al, 19th EPS Conference on Controlled Fusion and Plasma Physics, Innsbruck, 1992, Vol. I p279

[3] Smeulders P., Nuclear Fusion Vol.26 (1986) 267

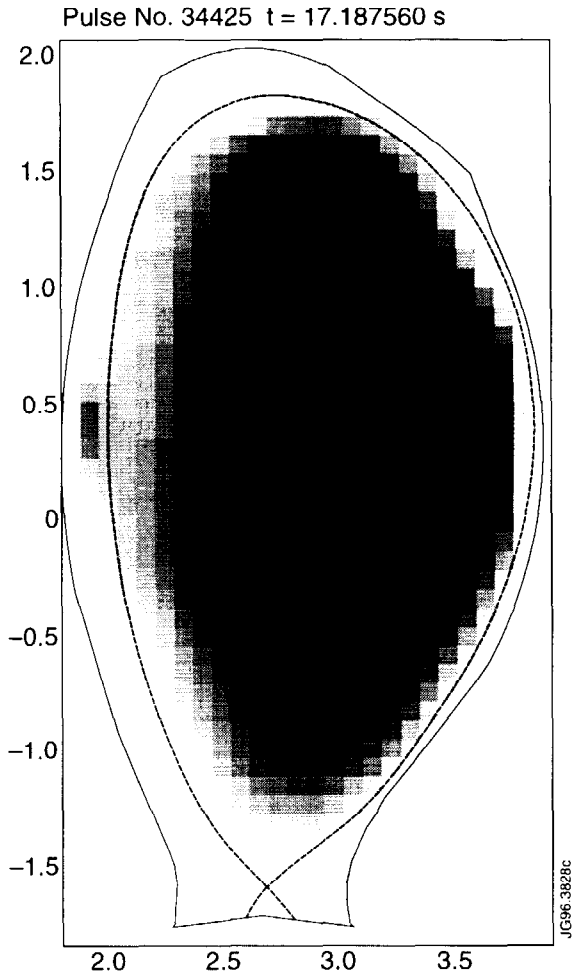

Figure 1. SXR emission during the high performance phase of a hot-ion H-mode discharge 34425

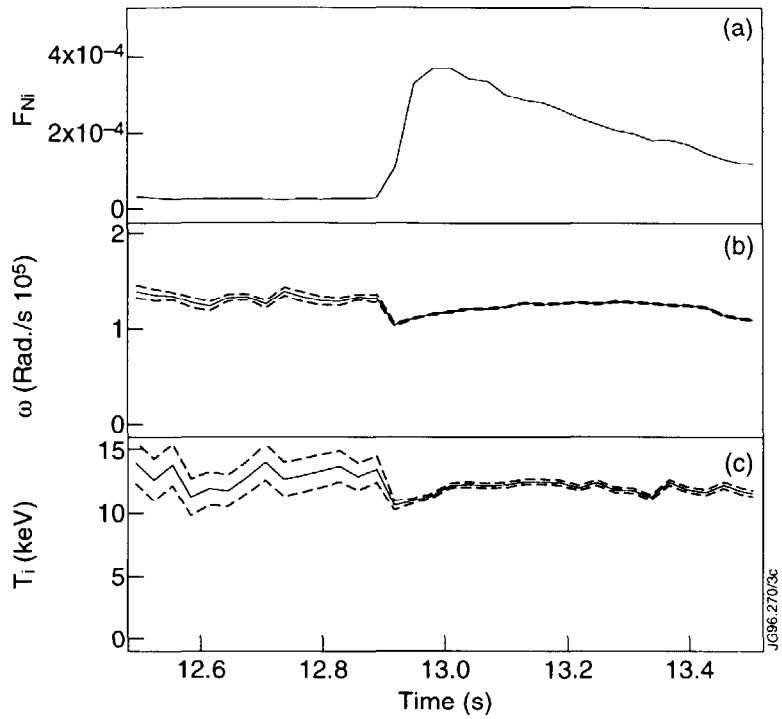

Figure 2. (a) Ni concentration, (b) Ni^{26+} angular frequency and (c) the ion temperature of Ni^{26+} with errors for shot 34476.

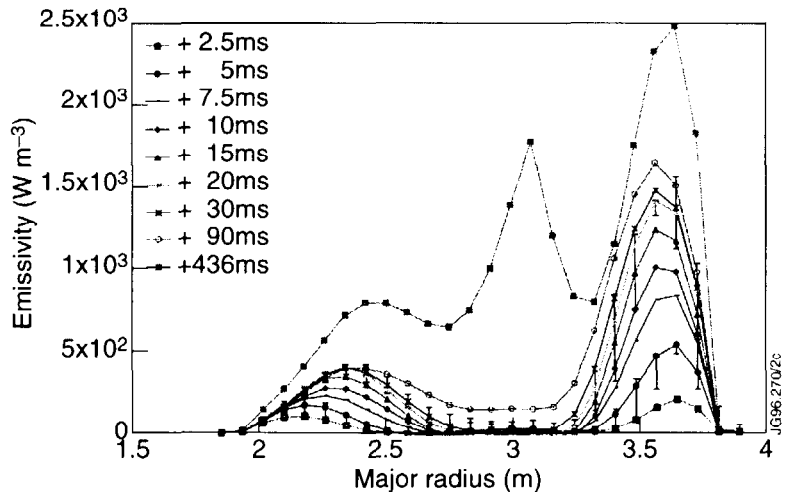

Figure 3 Emissivity projected onto a horizontal line through the magnetic axis after subtraction of the first - pre-ablation time slice for shot 34476.

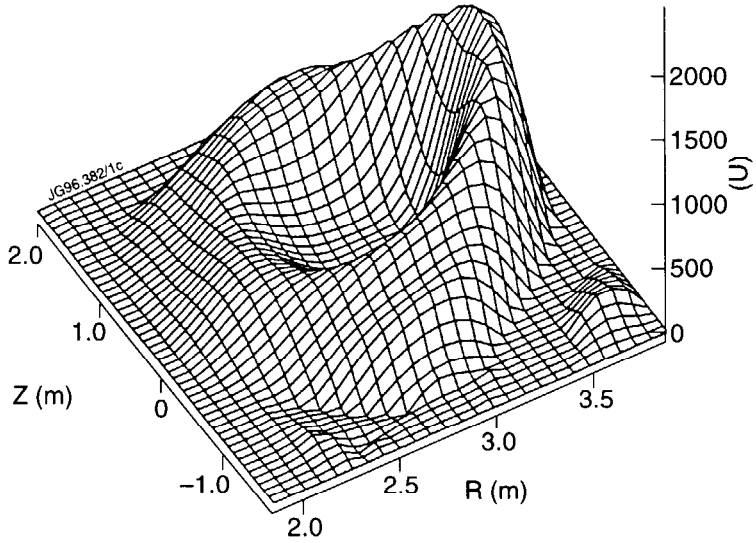

Figure 4 Tomographic reconstruction 30ms after nickel injection with background emission subtracted.

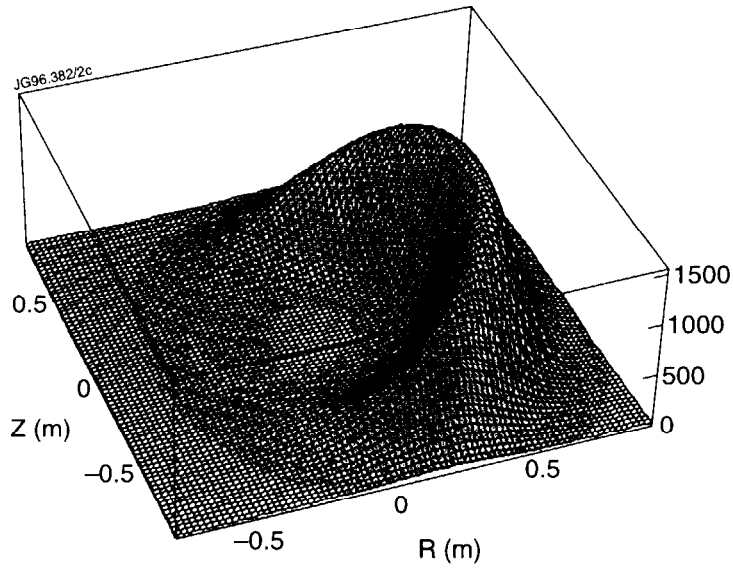

Figure 5 Simulation of the poloidal distribution of the Ni emission for shot 34476. The outer equatorial intensity from Fig. 3 at +30ms was used as input and circular geometry assumed

MHD Related Transport Analysis in JET

B. Balet, G. Huysmans, M.F.F. Nave1, P. Smeulders and J.A. Wesson

JET Joint Undertaking, Abingdon, Oxfordshire, OX14 3EA
[1]Associaçao Euratom/IST, Institute Superior Technico, Lisbon, Portugal.

INTRODUCTION:

The MHD activity observed during the JET hot ion H-modes, has been described in [1]. Three main types of MHD phenomena can be distinguished:

- Core modes such as sawteeth which cause substantial drops in the core temperatures.
- Outer Modes (OM) i.e. MHD oscillations (mainly n = 1, m = 3-5) with frequencies ~ 10kHz observed within the outer 20% of the plasma.
- Giant Edge Localised Modes (ELMs).

A selection of discharges (see Table I) has been analysed with the TRANSP code to clarify the effect of the MHD instabilities on the plasma transport. For that purpose an effective χ_{eff} is defined to quantify plasma losses:

$$\chi_{eff} = q_{loss}/(n_e \nabla T_e + n_i \nabla T_i)$$

χ_{eff} doesn't separate ion and electron loss channels and includes all loss terms (conduction, convection, CX losses etc).

A typical evolution of a hot ion H-mode pulse #34500, is shown in Fig.1. The performance appears to be limited by MHD events. A saturation of the neutron yield (= 0.5 × R_{DD}), $T_e(0)$ and W_{DIA} coincides with the onset of an OM (seen in the magnetic coil signal between 12.63s and 13s). The increase in the D_α emission is correlated in time and shape to the OM. The OM is interupted by a small ELM. The plasma performance recovers until a giant ELM at t = 13.25s, which marks a drop in R_{DD} and W_{DIA}. Finally at t = 13.45s, a sawtooth combined with a giant ELM coincides with the irreversible decline of R_{DD}.

OUTER MODES:

An increase of χ_{eff} near the edge, occurs at the time of the OM (see Fig.1). However, it is not clear how they are related quantitatively. Fig.2 shows the χ_{eff} profiles before (t = 12.55s), during (t = 12.8s) and after the OM (t = 13.2s) for #34500. During the OM, χ_{eff} ($\rho \geq 0.4$)

increases by a factor 2-3. After the OM, χ_{eff} returns to values comparable to the pre-OM values. An interesting point to note is that the increase in χ_{eff} occurs over a large part of the plasma radius, even though the OM is located beyond the q = 3 surface, with displacements of 2-3 cm. However, the onset of the OM is followed by an increase in recycling, an influx of impurities and a cool front which reaches the core in ~ 20 ms (see [1]).

The increase of χ_{eff} over a larger part of the plasma radius reflects the increased loss associated with this cool front.

ELM AND SAWTOOTH:

A typical evolution of $\chi_{eff}(\rho)$ is shown in Fig.3 for #34500. χ_{eff} increases by up to 40% in the outer region at the time of an ELM (13.3s). It doesn't recover its previous value after the ELM and in fact increases further (13.4s), reaching values ~ 70% higher than 0.2 sec earler. At the time of a sawtooth combined with an ELM (13.45s) a large increase of χ_{eff} throughout the plasma radius occurs (by a factor 1.5 for $\rho < 0.8$ to 2.5 near the edge).

BALLOONING AND KINK LIMITS:

The stability plot for external kink and ballooning for #34500 shows that the plasma edge is close to marginal stability for the external kink throughout the discharge (see Fig.4). This is compatible with the observed OM. The edge pressure gradient increases along the n = 1 kink stability boundary up to the ballooning limit which is reached around the time of the maximum in R_{DD}, coincident with an ELM. This suggests that ELMs are related to ballooning modes possibly combined with external kink. The same features are seen in #33648 and #33650, but not in the highest performance pulse #33643 whose edge remains in the stable region.

HIGH FREQUENCY MODES:

A variety of high frequency coherent modes (f > 30 kHz) is observed growing throughout the H-mode phase. Some seem to be associated with a saturation of R_{DD}. Their frequencies are consistant with β-driven Alfvén eigenmodes (BAE with f ~ 60kHz) and toroidal Alfvén eigenmodes (TAE with f ~ 110-120 kHz). (see Fig.5). The χ_{eff} profiles are not affected by these modes; this may indicate that it is mainly the fast ion population which is perturbed by the high frequency modes (causing a different beam deposition profile from the TRANSP calculated one).

NON-RECOVERY:

In some circumstances, the plasma performance doesn't recover after the MHD event. This is the case for #33648 where the temperature profile T_e doesn't increase anymore once the OM has disappeared, contrary to #34500 (see Fig.1) and despite the fact that both pulses show similar amplitudes and frequecies of the OM. The only difference is that, for #34500, the OM appears 0.63 sec after the onset of NBI, whereas it appears 1.25 sec after for #33648. The flattening of the beam deposition profile with time, due to the density build-up, is a feature of all the hot-ion H-modes (see Fig.6), and in shot #33648 prevents the plasma core from reheating after the OM.

TERMINATION:

The final loss of fusion performance is triggered in most cases by an OM and/or an ELM and in the highest performance pulses by a sawtooth and/or a giant ELM (see Fig.1). This is accompanied by a large increase of P_{rad} and D_α, and by a sudden drop in R_{DD}, W_{DIA} and temperature. During this phase, $\chi_{eff}(\rho)$ increases by a factor 2-3, denoting huge thermal losses (see Fig.3). After the terminating event, the plasma doesn't reheat (see $T_e(0)$ in Fig.5) partly due to a decreasing NBI central heating (see Fig.6) and to the fact that fast ions have been expelled out of the core region by the sawtooth.

The highest fusion performance #33643 doesn't show a change in W_{DIA} at the sawtooth as large as the comparable pulse #33650. (see Fig.7). However for #33643, W_{DIA} keeps on falling after the sawtooth, suggesting a lasting change in the transport state of the plasma. This behaviour is discussed in more detail in [2].

DISCUSSION:

The 3 classes of MHD instabilities (OM, ELM and sawtooth) have a clear effect in increasing the plasma energy losses. However this effect may be partly indirect. Sawteeth affect the fast ion distribution (and therefore the NBI heating profile). The OM and ELM, although localised in the outer part of the plasma, are accompanied by changes of the temperature profile over a wider region.

The precise loss mechanism associated with the MHD instabilities is unclear. Different interpretations have been put forward, each of them accounts for part of what is observed:

1) MHD is the direct cause of the degradation in transport.

2) MHD acts as a trigger to another state of the plasma transport, which partly remains once the MHD instabilities have disappeared.

3) MHD instabilities change the recycling conditions, causing a larger influx of neutrals and therefore increasing charge-exchange losses.

The investigation of the extent of these different processes is the aim of future studies.

CONCLUSIONS:

The TRANSP analysis of individual MHD events: Outer Modes, Giant ELM and Sawtooth + ELM, shows the radial extent and the amplitudes of the loss processes, however the precise loss mechanism is not known.

The MHD instabilities have more severe consequences in the later stage of the heating phase because of decreased central heating by NBI, due to the density build-up.

REFERENCES:

[1] F. Nave, et al., 'An overview of MHD activity at the termination of JET hot ion H-modes', to be published in Nuclear Fusion.

[2] J. Wesson and B. Balet, 'Abrupt changes in confinement in the JET tokamak', submitted to Phys. Rev. Letters.

Table I:

Pul no	B (T)	I (MA)	P (MW)	β_N	H_{89P}	$\langle n_e \rangle$ ($\times 10^{19}$ m-3)	q95	κ	δ	W (MJ)	R_{DD} ($\times 10^{16}$ s^{-1})
33643	3.4	3.8	18.8	1.6	2.9	3.9	3.2	1.9	0.31	12.0	8.9
33648	3.4	3.0	16.5	1.6	2.6	3.6	3.9	1.9	0.32	8.9	5.3
33650	3.4	3.5	18.6	1.8	2.7	4.8	3.3	1.9	0.29	11.7	6.5
34500	2.7	3.1	16.0	1.9	2.5	4.0	3.3	1.9	0.32	9.0	4.0

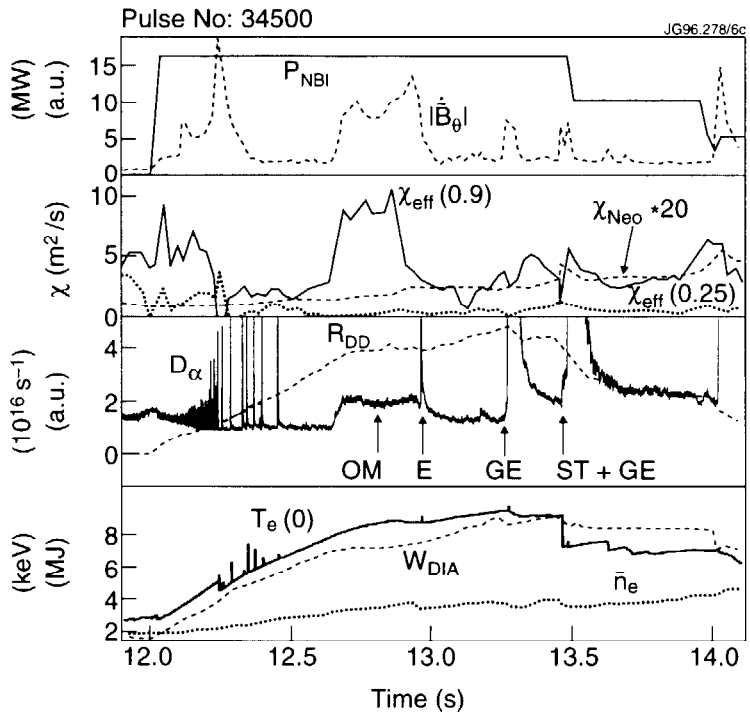

Fig. 1: Time evolution of pulse #34500 showing the NBI power and the magnetic perturbation, χ_{eff} at ρ = 0.25 and ρ = 0.9 together with the ion neo-classical heat conductivity χ_{neo}(20) at the edge as calculated by TRANSP, D_α signal and total DD reaction rate R_{DD}, the central electron temperature $T_e(0)$, the plasma stored energy W_{DIA} and the line averaged electron density $\bar{n}_e$.*

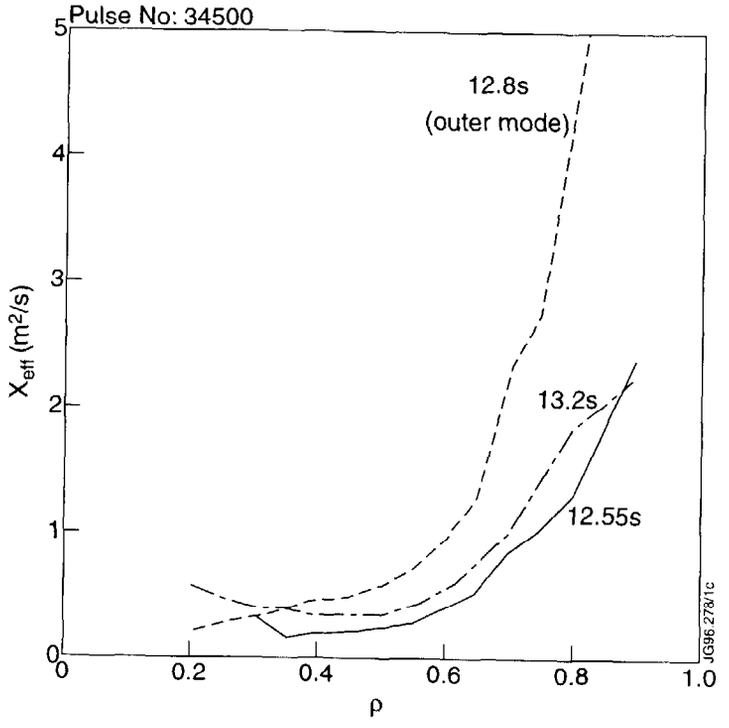

Fig. 2: χ_{eff} profiles before (t = 12.55s), during (t = 12.8s) and after (t = 13.2s) the OM for #34500.

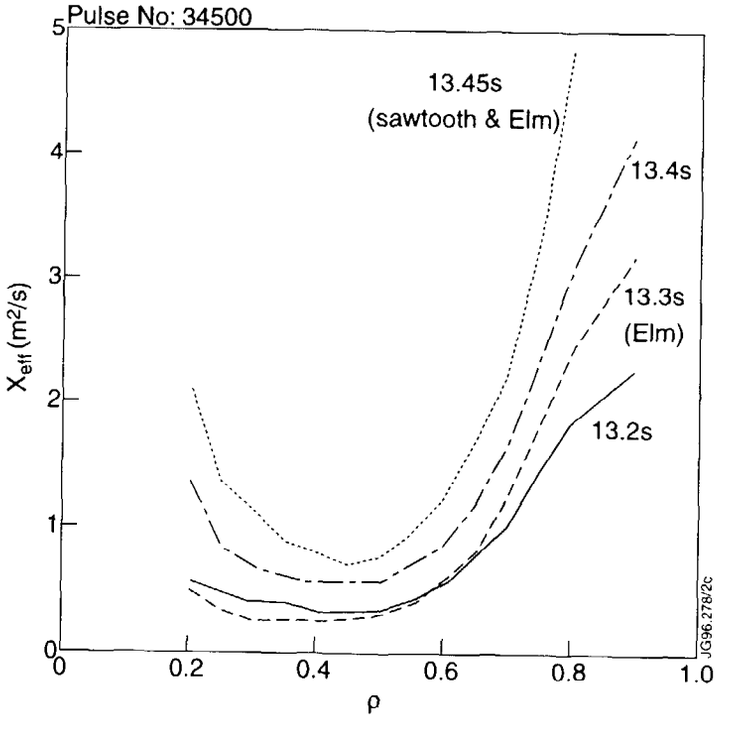

Fig. 3: χ_{eff} profiles for #34500 at different times.

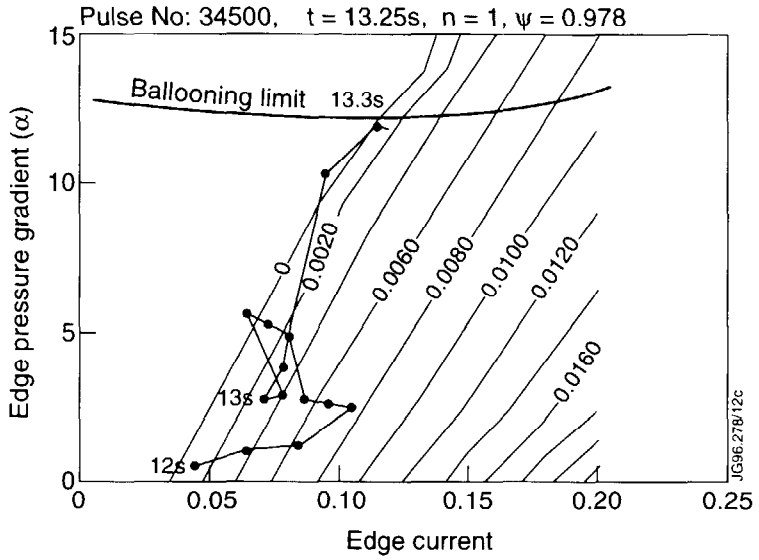

Fig. 4: Stability plot for the n = 1 kink and ballooning for #34500 at $\Psi = 0.978$.

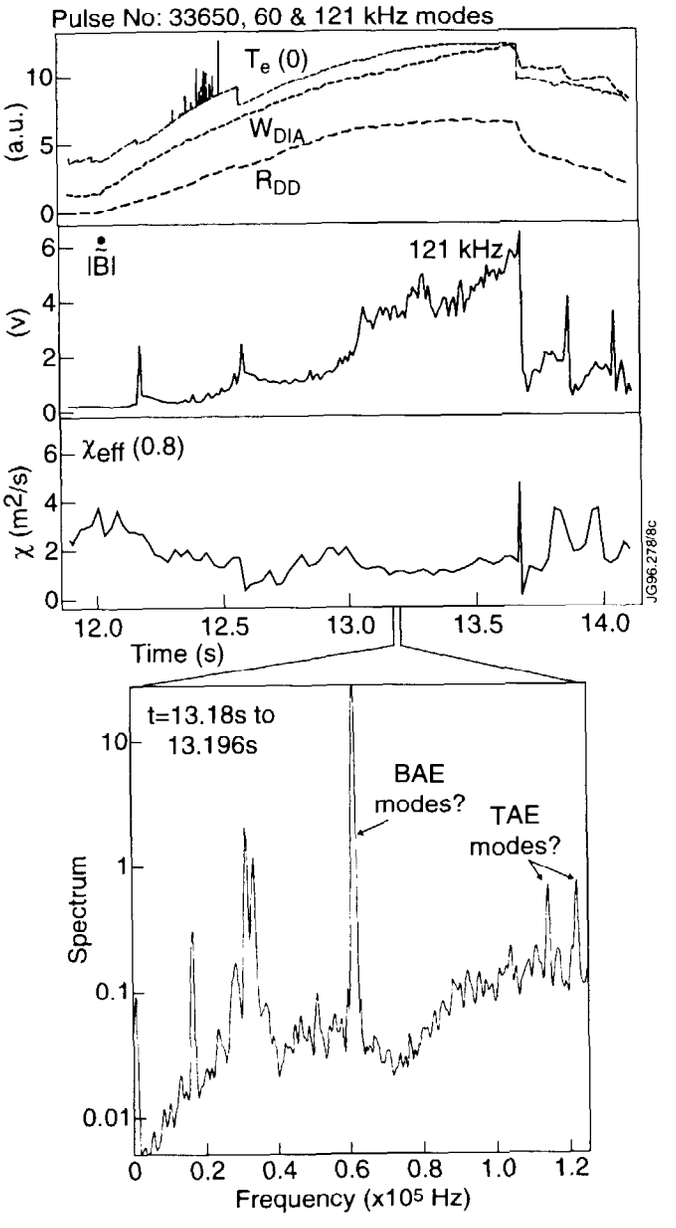

Fig. 5: Time evolution of pulse #33650 showing $T_e(0)$, W_{DIA} and R_{DD}, magnetic signals from comb filters at 121 kHz, χ_{eff} at ρ = 0.8 as calculated by TRANSP and spectrum versus frequency for t = 13.8 to 13.196s.

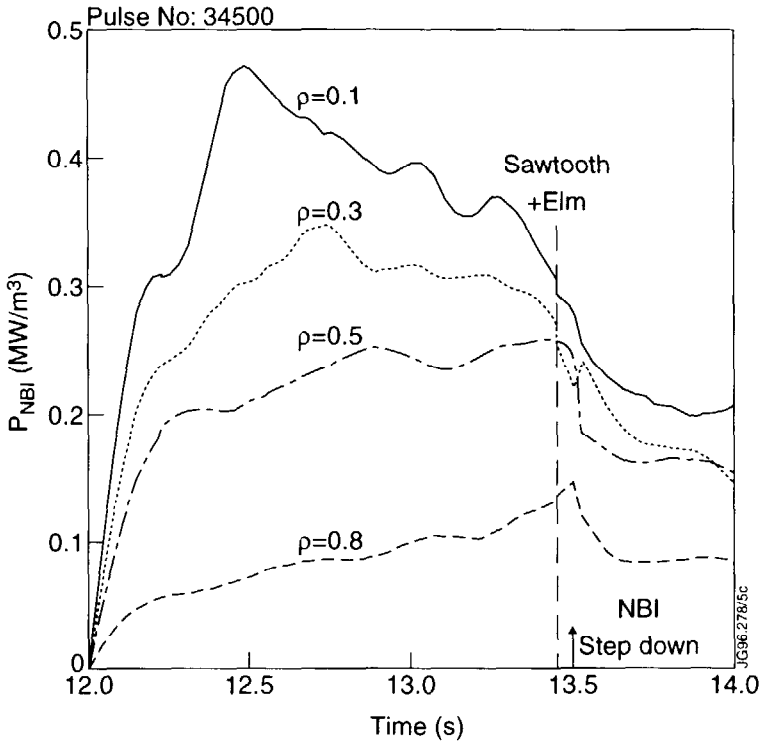

Fig. 6: Time evoultion of the absorbed NBI power density at different positions ρ for #34500.

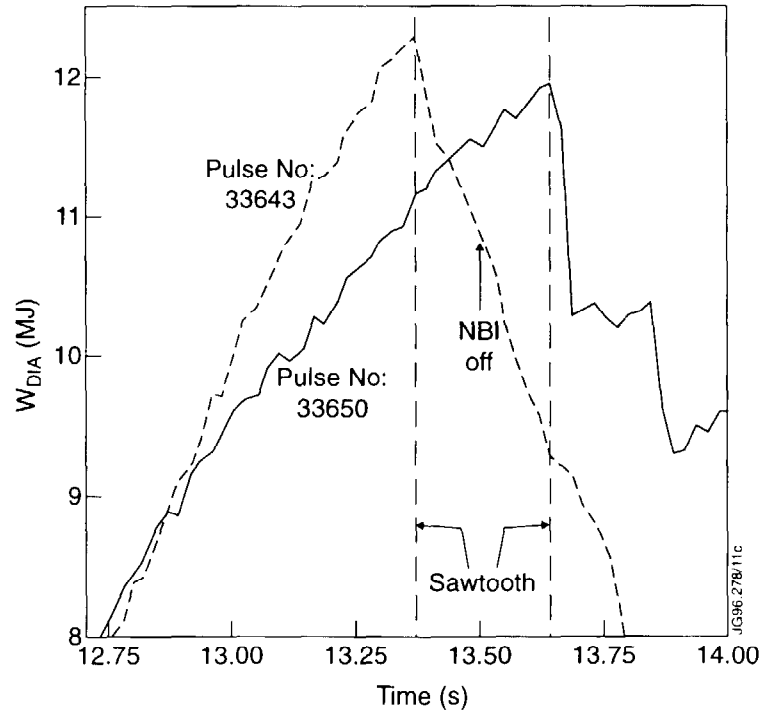

Fig. 7: Time evolution of W_{DIA} for pulses #33650 and #33643.

Linear and Nonlinear Dynamics of Alfvén Eigenmodes in JET Plasmas

D.Borba**, J.Candy, A. Fasoli*, W. Kerner, D.Muir, S.Sharapov

Jet Joint Undertaking, Abingdon, Oxfordshire OX14 3EA, U.K.
*CRPP, Assoc. EURATOM-Confederation Suisse EPFL , 1015 Lausanne, Switzerland
**Associação EURATOM/IST Av Rovisco Pais 1096 LISBOA PORTUGAL

ABSTRACT

The stability of Alfvén eigenmodes in JET is studied using a Hybrid Gyrokinetic MHD model which takes into account finite orbit effects, realistic plasma geometry and Alfvén waves fields including first order ion Larmor radius corrections. This analysis provides stability diagrams for global Alfvén eigenmodes in the presence of fusion products or energetic ions generated by auxiliary heating. The nonlinear evolution and saturation of the modes is studied using an Hamiltionian guiding center description of the particle motion in a perturbed magnetic field with a self consistent update of the amplitude and phase of the wave.

INTRODUCTION

The influence of energetic particles on the stability of Alfvén waves in the Joint European Torus (JET) is analysed using a three-step numerical procedure. First, the equilibria are reconstructed using the codes EFIT and HELENA. Secondly, linear properties of the toroidal Alfvén wave spectrum are determined by the MHD normal-mode code CASTOR (Complex Alfvén Spectrum in TORoidal geometry). The linear stability analysis includes the determination of the principal wave damping mechanisms, i.e. ion and electron Landau damping, radiative damping and collisional electron damping as well as the evaluation of the instability drive including effects due to large, non-standard (i.e potato) orbits characteristic of alpha particles and of radio-frequency-heated (RF) ions in the JET tokamak. Finally, the nonlinear mode evolution, including amplitude saturation and fast-particle redistribution/loss, is computed using the particle code FAC (Fast particle-Alfvén wave interaction Code).

JET discharges with a large fraction of RF and NBI generated ions are studied with distributions based on Fokker-Planck simulations using the codes PION (for RF ions) and PENCIL (for NBI ions). Possible scenarios for TAE excitation by alpha particles, as well as by NBI and/or RF-produced energetic ions, are studied in conditions relevant to JET DT experiments.

MODEL

Using the MHD equilibria reconstructed by EFIT and HELENA, the linear normal-mode analysis is performed by the spectral codes CSCAS and CASTOR. The linear MHD model (CASTOR-CR) includes first order finite ion Larmor radius effects and the perturbed parallel electric field. The CASTOR-CR code solves the linearized MHD equations with the parallel resistivity obtained from kinetic theory:

$$\eta \approx 4\pi i\omega {\rho_s}^2\left(\frac{3}{4}+\frac{T_e}{T_i}(1-i\delta_e)\right).$$

The electron dissipation includes collisional damping δ_e due to a finite longitudinal electric field and collisional curvature damping obtained from a tabulated solution of the bounce-averaged electron kinetic equation. ρ_s is the ion sound Larmor radius, T_i, T_e are the ion and electron temperatures and ω frequency of the perturbation. The contribution of energetic ions is included perturbatively. The CASTOR-K code computes the first order perturbation on the eigenvalue due to the resonant interaction between the wave and the energetic ion population using a gyro-kinetic model. The resonant Landau damping from thermal particles is included in the same fashion.

$$(\omega_r+i\omega_i)^2 K=\delta W_{MHD}+\delta W_{hot}\ ,\ \frac{\gamma}{\omega}=\frac{\omega_i}{\omega_r}=\frac{Im[\delta W_{hot}]}{2\omega_r^2 K}$$

K representes the kinetic energy of the perturbation, δW_{MHD}, represents the MHD part and δW_{hot} represents the contribution from energetic ions to the eigenvalue. CASTOR-K utilises the linear eigenfunction obtained by CASTOR-CR and decomposes the hot particle energy functional into poloidal bounce harmonics and integrates the resonant contribution over the particle phase-space $dP_\phi dEd\mu$ [3],

$$\delta W_{hot}=-\frac{2\pi^2}{\Omega m^2}\sum_\sigma\int dP_\phi dEd\mu\sum_{p=-\infty}^{\infty}\frac{\partial F}{\partial E}\frac{\tau_b\mid Y_p\mid^2\left(\omega-n_0\omega_*\right)}{\omega+n_0\omega_D+(n_0q+p)\omega_b},\ Y_p=\oint\frac{d\tau}{\tau_b}\ L^{(1)}\ e^{ip\omega_b\tau}.$$

$L^{(1)}$ represents the perturbed Lagrangian of the unperturbed particle motion, ω_D, ω_d the precessional drift and bounce particle frequencies. The nonlinear dynamics is studied using the FAC code. The nonlinear interaction of a discrete spectrum of low-β fluid modes with a hot particle source is described by a Hamiltonian guiding center scheme for the particle motion in the presence of a field perturbation with a self consistent differential update of the phase and the amplitude of the wave. The time evolution of the perturbed distribution function δf is described as an initial value problem by a set of markers (quasi-particles).

$$\frac{d}{dt}\delta f_{hot} = -\frac{d}{dt} f_{hot}{}^{0} - \upsilon \delta f_{hot}$$

ANALYSIS OF JET DISCHARGES IN THE PRESENCE OF ALPHA PARTICLES

Due to a combination of the mode structure and the finite orbit effects the most unstable modes in JET in the presence of alpha particles $E = 3.5\ MeV$ are KTAE modes with n=5 to 8. The analysis shows that alpha particles have a strong destabilising effect $\gamma/\omega \approx 2\langle\beta_\alpha\rangle$. But due to the alpha particle pressures possible in JET tritium experiments $\langle\beta_\alpha\rangle \leq 10^{-3}$ and the various damping mechanisms, these modes are expected to be marginally stable as shown in figure 2. The nonlinear simulations show that when the KTAEs are found to be unstable the saturation amplitude scales as $\frac{\delta B}{B} \approx 0.5\left(\frac{\gamma}{\omega}\right)^2$ and therefore the saturation amplitude is small $\frac{\delta B}{B} \approx 10^{-5}$. For these amplitudes no significant anomalous alpha transport is expected. The computations are based on a typical JET high performance discharge with $n_e = 5\times10^{19} m^{-3}$, $B_0 = 3T$, $T_i \approx 10 \rightarrow 20 KeV$ and $T_e = 10 KeV$, using an alpha particle slowing down distribution. In the stability diagram the ratio between the alpha particle velocity and the Alfvén velocity on axis $\frac{V_\alpha}{V_A}$ is scanned by changing the plasma density.

INFLUENCE OF NBI AND RF HEATING

High performance JET discharges are characterized by a large auxiliary heating power in the form of NBI or/and RF. Due to the nature of the orbits of RF generated ions (trapped ions), it is more difficult to excite KTAE modes than TAE modes with RF heating. The interaction between TAE modes and RF is strongest when the RF resonant layer is localised at the low field side of the torus as shown in figure 4.

NBI injected ions have lower energy $E \leq 140 KeV$ than RF produced ions $E \geq 500 KeV$ and are expected to destabilise only high-n (n>10) TAE and KTAEs at high densities. For low-n (n<10) modes the beams should have a stabilising effect. Detailed calculations including the radiative damping of high-n modes, the ion Landau damping at high densities and the destabilising effect of large beam power on high-n TAE and KTAE modes are required in order to determine the stability boundaries.

CONCLUSIONS

The hybrid Gyro-Kinetic-MHD model developed provides detailed description of the interaction of energetic ions with global plasma waves taking into account: realistic geometry, finite particle orbit width including large non-standard orbits, realistic wave fields including

first order ion Larmor radius corrections and linear and nonlinear evolution. Applications of the model to JET high performance discharges show that due to orbits effects RF ions do not have a strong influence on the KTAE modes. On the another hand neutral beam generated ions can destabilzize only high-n (n>10) TAE and KTAE modes at high densities. Alpha particles will have a strong destabilising effect only on low-n KTAE's modes due to finite orbit effects. As a consequence of the small alpha particle pressure and the various sources of damping low-n modes should be marginally stable in the JET tritium experiments.

REFERENCES

[1] H. L. Berk et al, Phys.Plasmas 2 (9), (1995) 3401

[2] A.Fasoli et al, Nuclear Fusion, Vol 35 No 12 (1995) 1485

[3] F. Porcelli et al, Phys. Plasmas 1 (3), March (1994) 470

[4] W. Kerner et al, Plasma Phys. Control Fusion 36 (1994) 991

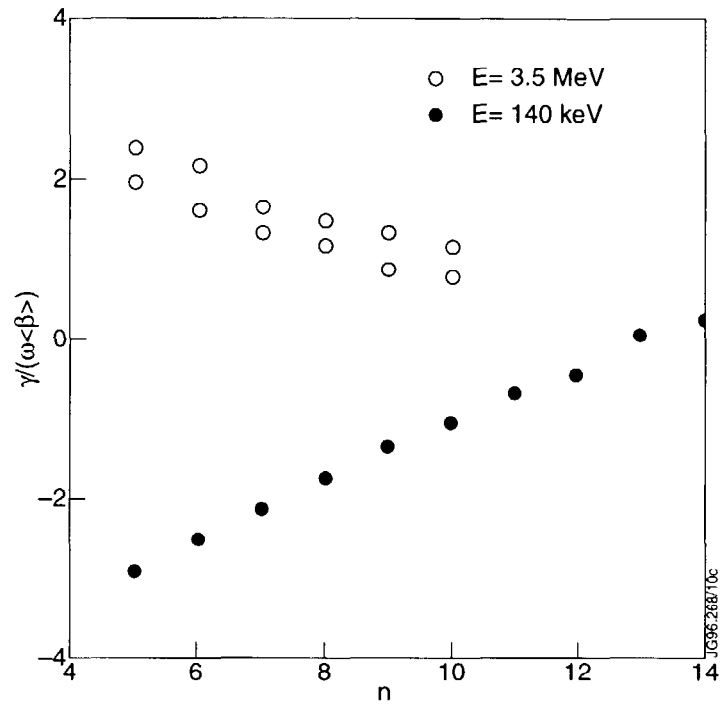

Figure 1 Drive due to a slowing down distribution of alpha particles and NBI generated ions for KTAE modes as a function of the toroidal mode number.

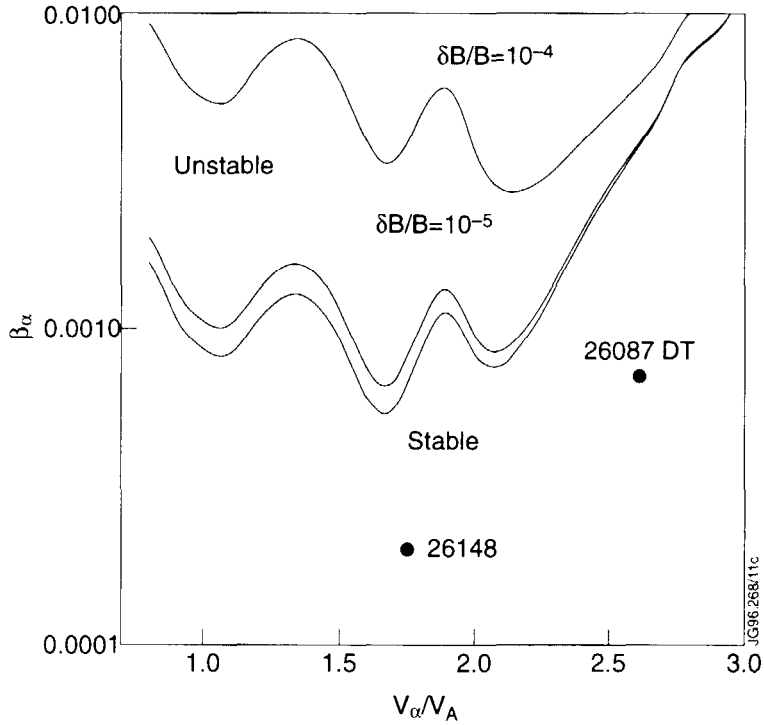

Figure 2 Stability diagram for KTAE modes in JET high performance discharges for 1) the preliminary tritium experiment PTE1 #26148 and 2) a future 50% tritium discharge based on #26087.

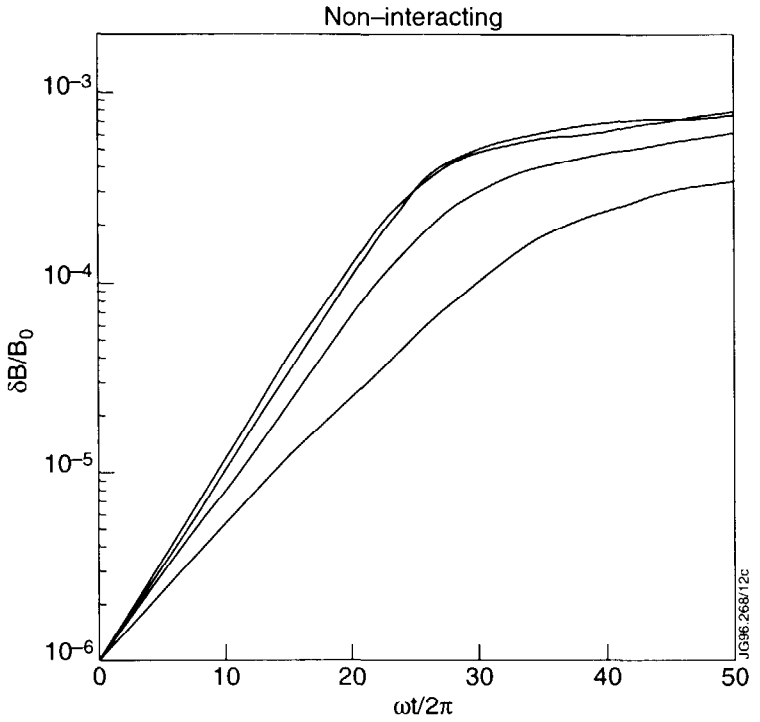

Figure 3 Nonlinear evolution of unstable KTAE modes with n=5 to 8 in the presence of alpha particles. Each toroidal mode is simulated individually .

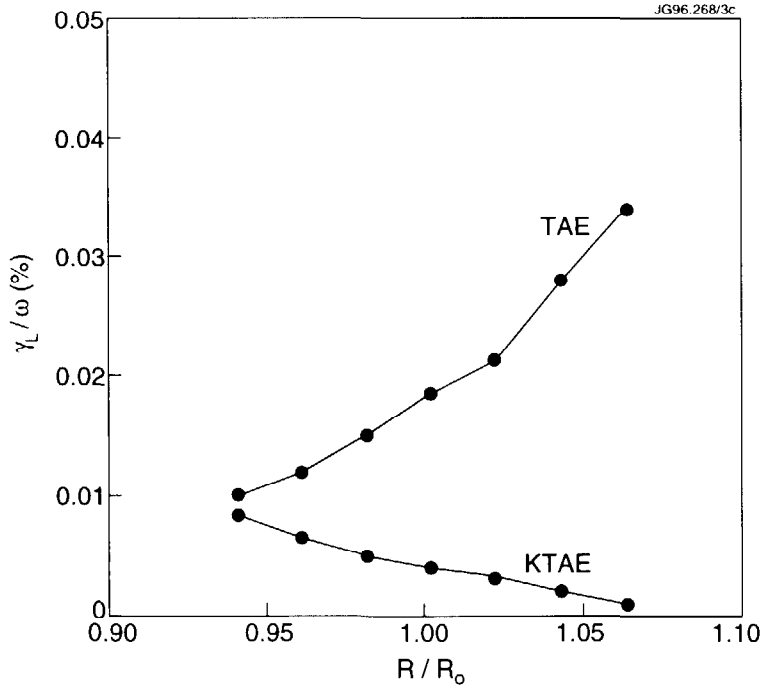

Figure 4 Growth rate of TAE and KTAE modes as a function of the RF resonant layer position in the presence RF generated ions. Optimal excitation is achieved for TAE modes when the resonant layer localized in the low field side of the torus.

A Description of ELM-Free H-modes in Terms of a Neoclassical Edge Barrier and a 'Mixed' Model for Energy and Particle Transport

A. Cherubini, B.Balet, N. Deliyanakis, M. Erba, R.Giannella, N.C. Hawkes, V.V. Parail, L. Porte, A.Rookes, E. Springmann, A. Taroni

JET Joint Undertaking, Abingdon, OX14 3EA, UK

INTRODUCTION:

High performance in JET ELM-free H modes appears to be related to the edge temperature, which can reach several *keV*'s, contributing up to half of the stored energy. A model to compute these edge values must then be given in order to predict plasma confinement. The existence of a neoclassical transport barrier was assumed in *[1]*: transport inside the separatrix is reduced to ion neoclassical values on a width scaling with the ion poloidal Larmor radius $\rho_{\theta i}$. In this work we extend that model to include plateau effects, and most importantly include particle transport, using the JETTO transport. Particle confinement and recycling conditions are shown to be crucial factors for energy confinement and the evolution of the discharge, as observed in experiments.

ENERGY TRANSPORT MODEL IN THE CORE PLASMA:

We use a 'mixed' transport model *[2]*, which combines a gyroBohm ($\chi_{gB} = c_{gB}\sqrt{T_e}\nabla T_e / B_T^2$) and a Bohm-like term ($\chi_B = c_B (\nabla P_e / n_e B_T) q^2 a^2 < \nabla T_e / T_e >_{\rho>0.8}$):

$$\chi_e = \chi_B + \chi_{gB}$$
$$\chi_i = 2\chi_B + \chi_{gB} + \chi_{neo,i}$$

This model can be used to describe both L and H modes, due to the non local dependence of the Bohm-like term on $L_{T_a}^{-1} \equiv < \nabla T_e / T_e >_{\rho>0.8}$, the electron temperature scalelength averaged in the outer 20% of the radius, excluding the transport barrier.

EDGE TRANSPORT BARRIER:

We assume that in H modes, free from ELMs or other MHD activity, all transport coefficients are reduced to ion neoclassical values, on a width $\sim\rho_{\theta i}$ inside the separatrix. In the banana regime, relevant to JET high performance shots, the heat loss from the edge then scales as: $Q_{neo} \sim n_a \chi_{i,neo} T_a / \rho_{\theta i} \sim Z_{eff}\, n_a^2 / I_p$, and particle losses as $\Gamma_{neo} \sim Q_{neo} / T_a$.

An important energy loss term is due to charge exchange with cold neutrals: $P_{CX} \sim \Gamma_0 T_a$, where Γ_0 is the neutral influx from the edge. We write $\Gamma_0 = \Gamma_{neo} + S^+$, with S^+ taking into account any sources in addition to the 100% recycling. When S^+ is small compared to the outgoing flux Γ_{neo}, then $P_{cx} \sim \Gamma_{neo} T_a$ and so total energy losses will retain the neoclassical scaling. Additional energy losses due to radiation P_{RAD} are included in the simulations, but are often negligible.

The scalings change when the edge approaches the plateau regime, when $\nu^* > 0.1$. The energy losses are not independent of T_a anymore: $Q \sim n_a T_a^2$, and a pedestal saturation is expected.

From the given scalings some conclusions can immediately be drawn.

a) The best confinement will require low edge density, and low recycling conditions (wall conditioning).

b) Steady state can be reached only in three ways: stepping down the input power P; increasing n_a up to $\sim\sqrt{P}$; elming or other additional energy losses (e.g. increased radiation).

c) While n_a remains low (i.e. heat loss $Q \sim n_a^2$ small compared to P), a situation of near thermal runaway is created, with $W \sim P - Q$. Typically both W and T_a rise on a timescale faster than n_a, so the plasma hits a local β-limit (e.g. ELM, 'slow roll over', etc.) before reaching steady state. This is typically the case of JET high performance discharges.

In the JETTO code the transport barrier can be simulated in two ways. Either it can be taken into account explicitly, reducing all transport coefficients appropriately on a few mesh points close to the separatrix, or the neoclassical fluxes can be imposed as Neumann boundary conditions, thus solving the transport equations only up to the transport barrier. The two methods have been shown to be equivalent (see later), but the former allows coupling with SOL codes, as EDGE2D *[3]*, and thus further validation against SOL measurements.

Semipredictive simulations, i.e. imposing the density profile from measurements, have been initially used to check some of the dependencies predicted by the model. A series of discharges was performed scanning density and current and optimizing the configuration for edge measurements. All relevant plasma characteristics were successfully reproduced, even for shots with the edge approaching the plateau regime. These simulations support the dependencies of the model on current and collisionality, but given the importance of n_a, modelling of particle transport is required.

FULL ENERGY AND PARTICLE SIMULATIONS OF ELM FREE H MODES:

The NBI particle deposition profile is a very important ingredient in the analysis. This was obtained from the TRANSP Montecarlo package. The source profile of edge cold neutrals is computed by the code FRANTIC, with the total influx given by $\Gamma_0=\Gamma_{neo}+S^+$. When simulating an experimental discharge, S^+ can be imposed to reproduce the total particle content.

We describe the particle flow by using only an 'effective' diffusion term: $D_{eff} = f(\rho)\chi_e\chi_i/(\chi_e+\chi_i)$. The radial function $f(\rho)$ was chosen in one of the shots in order to reproduce the shape of the measured density profiles and the magnitude of Γ_0, and then kept constant in different shots. It turns out that in order to reproduce the experimental density profiles $f(\rho)$ must decrease from $f(0)\sim 1$ to $f(1)\sim 0.1$, though its exact form cannot be precisely determined (linear was used). This result can be interpreted as an indication for the existence of an inward pinch localized in the outer region of the plasma, in agreement with similar results from ohmic mode*[3]*.

All the main experimental measurements of hot-ion H modes have been satisfactorily reproduced, when S^+ is given as above. Typical density and temperatures profiles computed for a very high performance shot are given in *Fig.1,2*, together with experimental ones. Relevant time traces are given in *Fig.3*. The neutral flux Γ_0 grows up to $\sim 2\ 10^{21} s^{-1}$, in good agreement with the SOL modelling and measurements *[4]*.

To study the effect of recycling conditions we have scanned S^+, and run the simulations for a time longer than the experimental MHD-free period (usually <1.2 *s*). *Fig.4* shows the predicted time evolution for the stored energy, fusion reaction rate, and neutral influx: increasing S^+ causes higher n_a and lower T_a, leading to an increase in Γ_{neo} (and so Q_{neo}) even bigger than S^+ itself.

It is clear that low recycling is essential to high performance. Higher neutral influx will induce lower pedestal temperatures and increase transport everywhere, via $L_{T_a}^{-1}$. Natural saturation and even degradation of the high confinement phase is observed (*Fig 4*), because n_a grows in time ~linearly and so energy losses with $\sim t^2$, but the timescale on which saturation appear depends on recycling conditions, and it can be longer than the MHD free period.

The degradation of confinement can also be caused by an impurity influx: the increase in edge Z_{eff} enhances Γ_{neo} , and hence both Q_{neo} and P_{CX} , reducing pedestal and confinement (the increased radiation will also play a role). This effect can be used to simulate experimental confinement degradation ('slow roll over'), assuming a trigger event (MHD) to increase Z_{eff}.[5]

CONCLUSIONS:

The neoclassical transport barrier coupled with the 'mixed' transport model provides a reasonable description of the ELM-free H-mode. The scalings for energy and particle losses have been derived and tested in numerical simulations of experimental discharges.

Simulation of particle flows requires an 'effective' diffusion decreasing towards the edge, a possible indication for the existence of an inward pinch strongly growing in the outer region.

Energy and particle transport in hot ion discharges have been successfully simulated, including the prediction of pedestal values. High confinement is achieved when the energy losses through the barrier are small thus leading to high pedestal values, this in turn reduces the transport coefficients throughout the plasma.

The main energy losses are the predicted neoclassical heat losses and charge exchange with cold neutrals. Low recycling (wall conditioning) and low impurity content prove to be the main factors required to maintain the small energy losses necessary for high confinement.

REFERENCES

[1] M.Erba et al., proc. of 22nd EPS Conf. on Contr. Nucl. Fus. & Pl. Phys., Bournemouth, 1996, pII-213

[2] V.Parail et al., JET-P(95)49, to be published in Pl. Phys. and Contr. Fus.

[3] A.Taroni et al., this conference.

[4] G.K.McCormick et al., 12th PSI Conference, St.Raphael, France, 20-24 May 1996.

[5] H. de Esch et al., this conference.

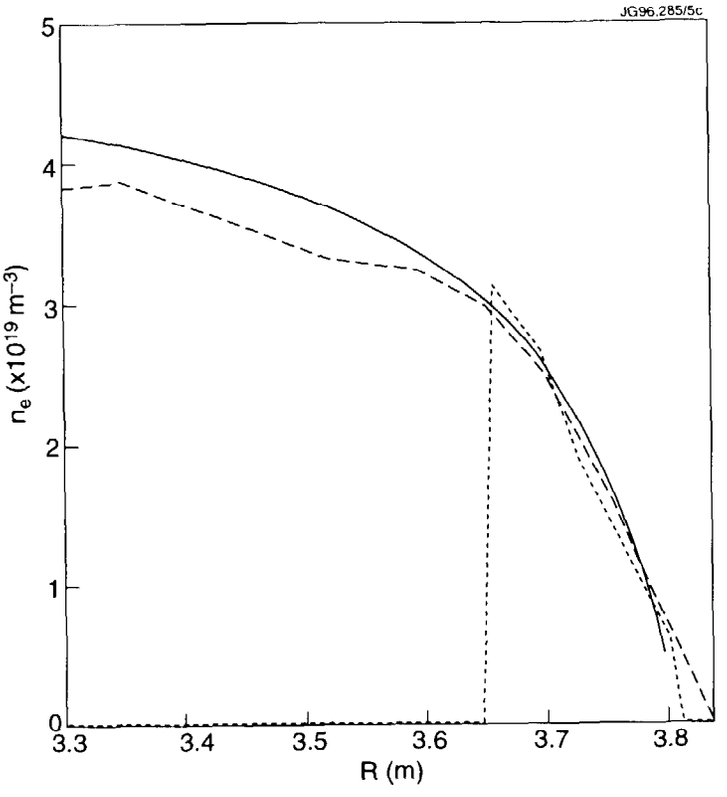

FIG.1 Computed (full line) density profile vs LIDAR(dashed) and reflectometry(dots), shot 33643, at t=53. *Note no discontinuity in gradient at the barrier* (R>3.75~m). *Reflectometry provides reliable information close to the boundary.*

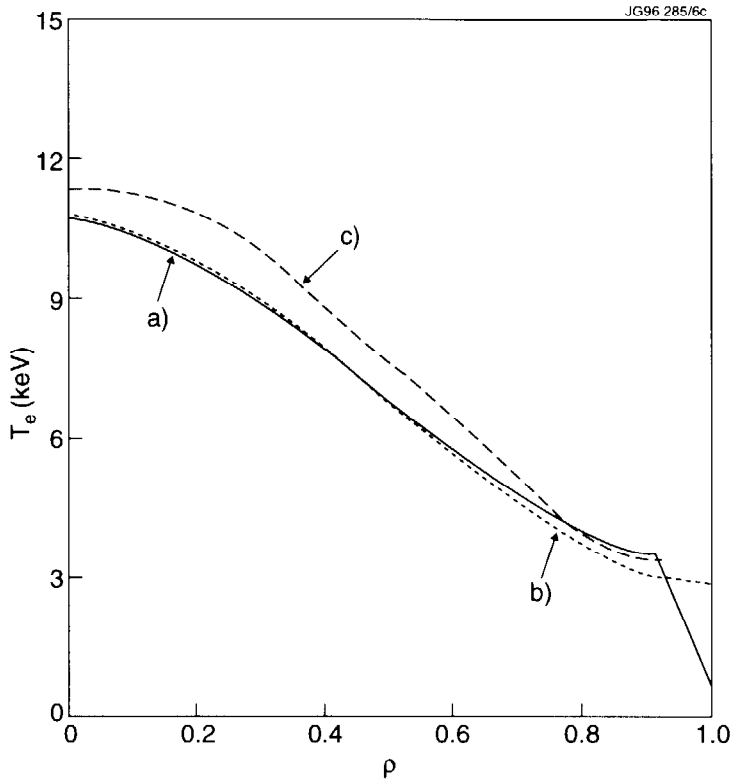

FIG.2 Profile comparison at t=53 *of measured (LIDAR, trace c) and computed* T_e *profiles, shot 33643. Trace a is computed imposing the barrier explicitly: the change in slope is clearly visible. Trace b was computed with the barrier imposed as Neumann boundary condition.*

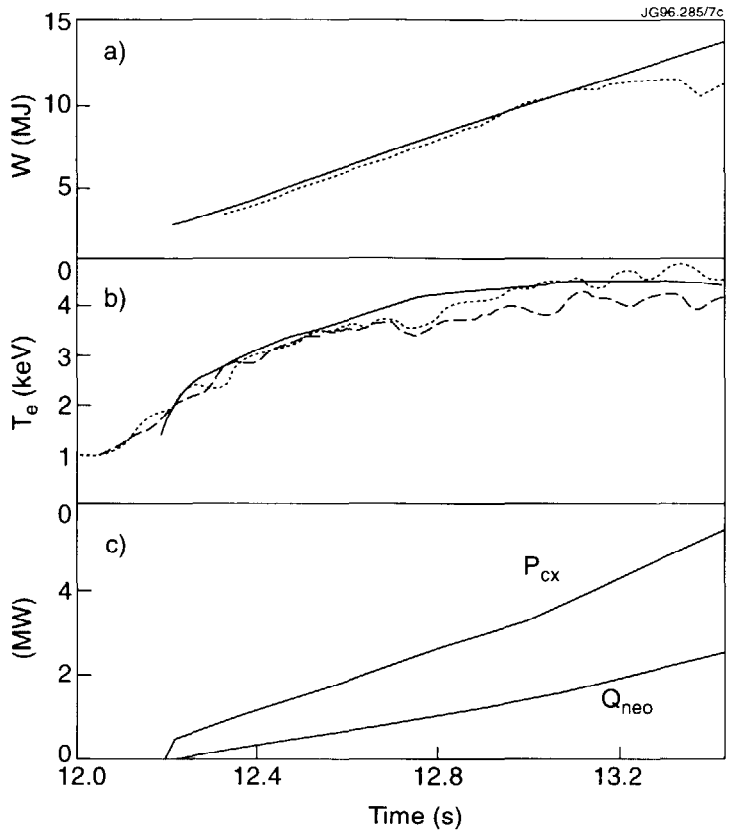

FIG.3 Measured and computed time traces for #33643. Note that experimentally the discharge suffers a 'slow roll over' at t~53.2, *followed by a giant ELM. a) thermal energy (full line is simulated) b)Edge ion temperature. Full line is simulated, the others are from charge. c) Simulated heat losses: full line is total neoclassical losses* Q_{neo}, *dotted line is charge exchange losses to cold neutrals,* P_{CX} . *Note the importance of* P_{CX}, *that nonetheless remains proportional to* Q_{neo}.

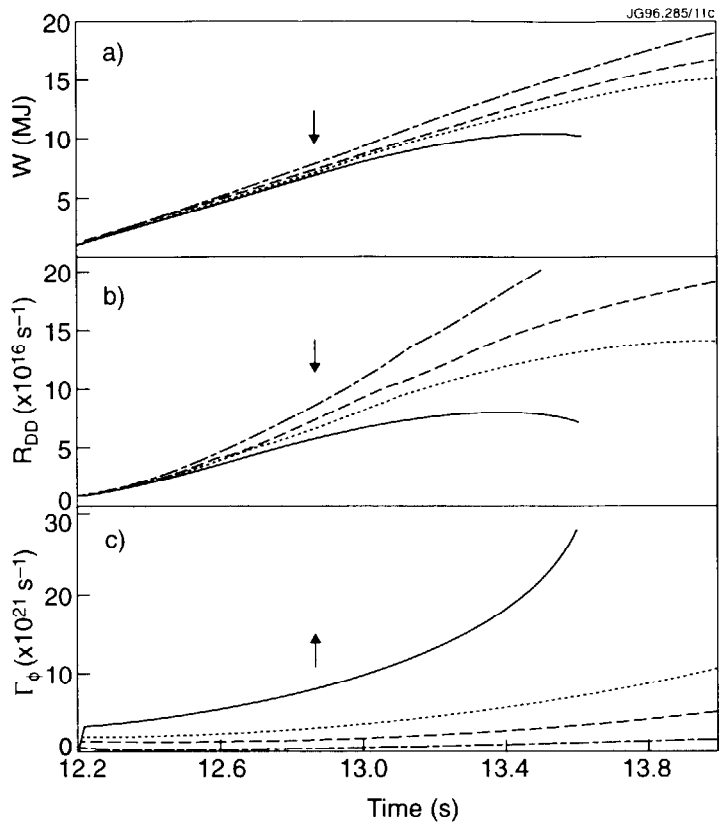

FIG.4 Scan in S^+ =0,0.5,1,2 x10^{21} . *a) energy content b) fusion reaction rate* R_{DD} *c) cold neutral influx from edge* Γ_{0+}. *The arrow indicates increasing* S^+.

Effects of Density and Plasma Configuration on the Divertor Asymmetries

S Clement, A Chankin, S Davies, J Lingertat, R Monk, R Sartori and M Stamp.

JET Joint Undertaking, Abingdon, OXON, OX14 3EA, UK

1. INTRODUCTION.

Asymmetric power deposition with more power going to the outer divertor target is usually observed in single null divertor configurations and is expected from geometrical toroidal effects (higher area of outer magnetic surfaces) and higher anomalous transport towards the outer midplane. The additional effect of drift forces has been discussed in [1]. This paper presents the first results of an analysis of the asymmetries obtained in H-mode regimes. It is found that the magnetic configuration has a strong influence on the imbalance of power and particle fluxes in the divertor. The effects of gas fuelling are also discussed. Two regimes are distinguished: 1)hot ion mode regimes: these have high power (18 MW), central fuelling with the neutral beams (no gas fuelling) and result in a high temperature, poloidally isothermal scrape-off layer (SOL); one expects poloidal drifts to increase the asymmetries; 2) radiative divertor regimes: medium to high power (12MW), edge gas fuelling: these result in a high radiation fraction in the divertor region, and non-isothermal SOL, with possible extra radial drifts[1] which in turn may modify the particle and power exhaust ratios. Langmuir probe data implies high edge ion temperatures in low density hot ion modes. There is empirical evidence from other machines that high edge temperatures are associated with toroidal momentum [2] in the edge plasma. This effect has the correct sign to increase the density at inner divertor.

2. HOT ION MODE: EFFECTS OF THE PLASMA CONFIGURATION.

In general, the power flow towards the outer strike zone should be larger due to geometrical toroidal effects [3] (higher area of the outer magnetic surfaces: calculations yield a 23% higher outer pressure for JET toroidicity), higher $D_{\perp}$ towards outer mid-plane, and the Shafranov shift ([1] and references therein). Furthermore, in the low density/low recycling hot ion mode regime, one expects high and poloidally uniform edge temperatures to cause strong radial electric field and poloidal $E_r \times B$ drifts that should increase the asymmetry.

Higher power to the outer strike zone has been observed in most JET magnetic configurations (see[1] for ohmic and L-mode discharges). This was also evidenced by the fact hat most of the damage occurred on outer divertor tiles.

However, we have found that **high magnetic shear** configurations show a more even power distribution than the low shear equivalent discharges, and the power imbalance can even be reversed in favour of the inner strike zone. High confinement regimes have been found to depend on the magnetic configuration in DIII-D [4] and JET [5].

Fig 1 shows time traces for two discharges with I_p=3.8MA, B_t=3.4T . Discharge #32969 has a shear at q=95% SH_{95} =3.6, discharge 36677 has SH_{95} =5.0, at the time of the peak neutron rate . It can be seen that the inner and outer strike zone peak temperatures are very similar in the higher shear case. The effect of shear (or more generally, of the shape of the plasma) has been studied for two series of discharges of hot ion modes: 1) the 20 best discharges of the campaign in terms of peak neutron production (plasma current 3MA $\leq I_p \leq$ 4MA, toroidal field B_t= 3.4T, input power P_{in}= 18MW NBI, shear values 3.1 $\leq SH_{95} \leq$ 5, no gas fuelling); 2) a series of 12 discharges of a configuration scan (I_p = 2.5MA, B_t = 2.5T, P_{in} = 10MW NBI, shear values 2.8 $\leq SH_{95} \leq$ 4.2, no gas fuelling, no tile temperature data available). All the discharges in the high performance dataset have moderate to high shear. The dataset includes two main types of configurations: the high flux expansion single null (moderate shear) and the double null type of discharge (high triangularity, high shear).

All these discharges have low divertor densities and electron temperatures above 50eV, as measured by Langmuir probes. For the probe measurements the power accountancy is poor, indicating that the ions carry a higher fraction of power to the divertor than electrons. Good global power balance is found with the IR camera measurements. These discharges radiate below 10% of total input power, and show a constant and very weak D_α emission in the divertor during the ELM free period. It is observed that: 1) the ratio of outer to inner peak surface temperatures decreases with magnetic shear during the ELM- free H-modes (fig. 2); 2) the same trend is observed in the D_α ratio (fig3), as one would expect in a high temperature SOL, with no temperature gradients along the field lines; 3) the same effect on the temperature ratio is observed in the low confinement phase that follows the hot ion mode, although the temperature values are more scattered (movement of the strike points due to β changes).

Drifts alone cannot explain the higher power going to the inner strike zones at high shear for poloidally isothermal plasmas. Other possible explanations could be related to: 1) toroidal momentum: its effect is expected to be important at high edge temperatures; however high electron temperatures are measured in all the high performance dataset; unfortunately ion temperature data are not available to show if there is any effect of the plasma configuration. 2) fluctuations, observed to be different in the high and low field side; however, the position of the heat source does not seem to matter too much in isothermal SOLs; 3) thermoelectric currents in the SOL.

It has to be noted that the same trends are obtained by plotting the data against the triangularity of the plasma. The values of the triangularity are calculated with a greater accuracy than those of shear, because it is an edge parameter. However, there is a strong correlation

between shear and triangularity in the dataset used. Finally, no correlation with the plasma current or with q was found.

3. RADIATIVE DIVERTOR REGIMES: EFFECT OF DENSITY (GAS FUELLING).

When gas is injected in the divertor or the SOL, the resulting increase of the edge density will change the pattern of radiation in the divertor region. This is particularly important for radiative divertor regimes. In L-mode confinement regimes [1], the ratio of the power in the outer and inner strike regions ranged from a factor ≈ 1.5 to values ≈ 3. In general, the asymmetries in the electron density, temperature and D_α fluxes appeared to be consistent with radial $E_\theta \times B$ drifts playing an increasingly important role as the density and hence the parallel temperature gradient was increased. However, the effect of increasing the divertor density on the power distribution was obscured by the onset of detachment occurring at the inner strike zone.

Two discharges at high power and far from detachment have been chosen to compare the effects of the density. The configuration is one of moderate shear ($SH_{95}=3.3$), and the power going to the target plates is very similar in the two cases. It can be seen (fig.4) that gas fuelling increases the density by a factor of two and brings the asymmetry factor in the divertor temperatures from 1.1 to 1.6 . The relative change in the radiated power in the divertor $Prad_{outer}/Prad_{inner}$ changes only from a value of 1 at low density to 0.85 at high density. This result is consistent with the development of a poloidal temperature gradient in the SOL as the density increases, giving rise to high radial $E_\theta \times B$ drifts.

4. CONCLUSIONS.

In the majority of the configurations used at JET more power flows to the outer than to the inner strike point, as expected from theoretical predictions; however in hot ion mode regimes (poloidally isothermal SOL) we observe a more even power distribution as the magnetic shear (or the triangularity) is increased. This effect is also observed in the particle flux to the divertor region. These observations are not accounted for by any classical drift. Toroidal momentum could play a role in the development of these asymmetries. However edge ion temperature data are needed to determine its importance.

The effect of gas fuelling on the power ratio is consistent with the development of a poloidal temperature gradient in the SOL as the density increases, giving rise to radial $E_\theta \times B$ drifts. The effect of the magnetic configuration on the power and particle distribution poses a problem for the design of a divertor for ITER. Codes based on edge and divertor parameters may need to have a model of the central plasma coupled to make reliable predictions.

The work of P J Lomas and Task Force H is gratefully acknowledged.

REFERENCES

1. A Chankin et al, Plasma Phys. Control. Fusion 36 (1994) 1853.
2. A Chankin and W Kerner, Nucl. Fusion 36 (1996) 563.
3. P J Harbour, Contrib. Plasma Phys 28 (1996) 417.
4. J Stambaugh and the DIII-D Team, Proc. of the 15th IAEA Conference on Plasma Physics and Controlled Nuclear Fusion (1994) 83.
5. PJ Lomas and the JET Team, as above, p.211.

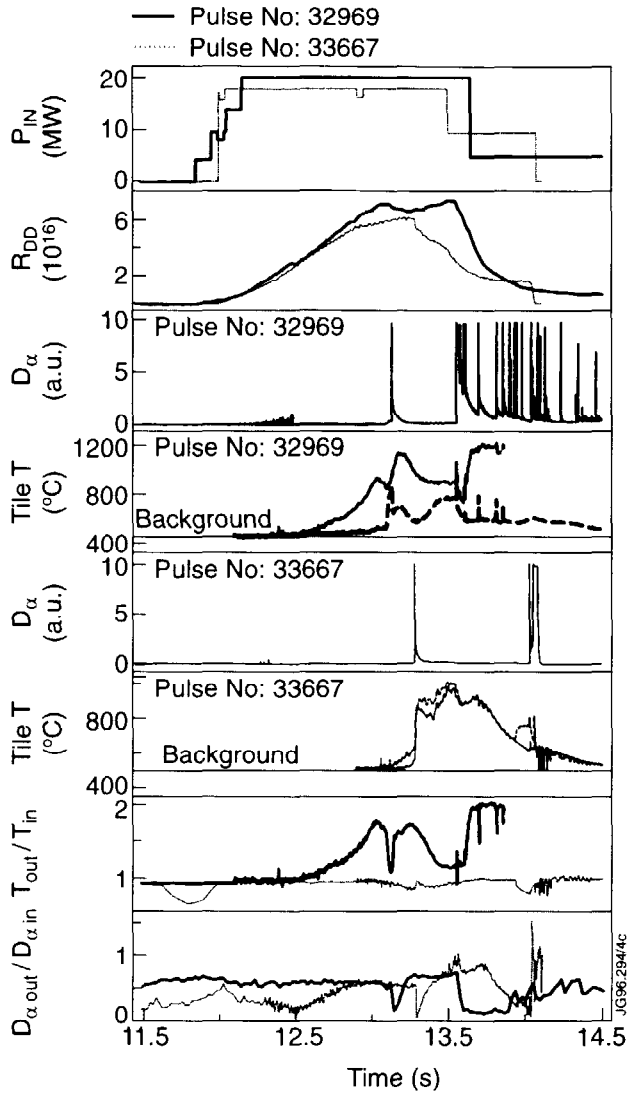

Figure 1 Time traces of the input power, radiated power, power going to the divertor target, central line density and the temperatures of the inner and outer strike zones for shots #35752(no gas fuelling) and #35752 (high gas fuelling).

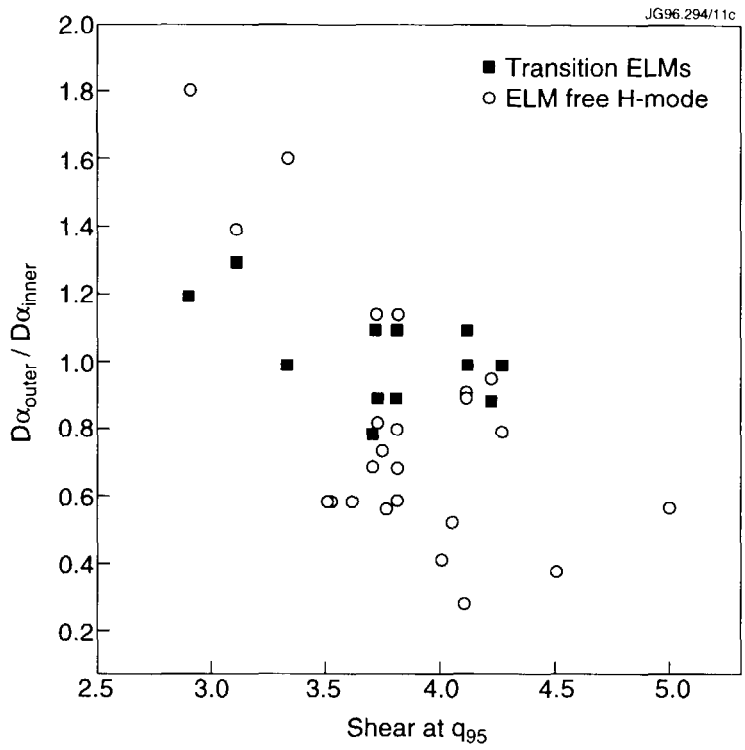

Figure 2 Ratio of the outer to inner strike zone total integrated particle fluxes versus shear at q_{95}.in ELM-free H-modes, and during the transition ELMs.

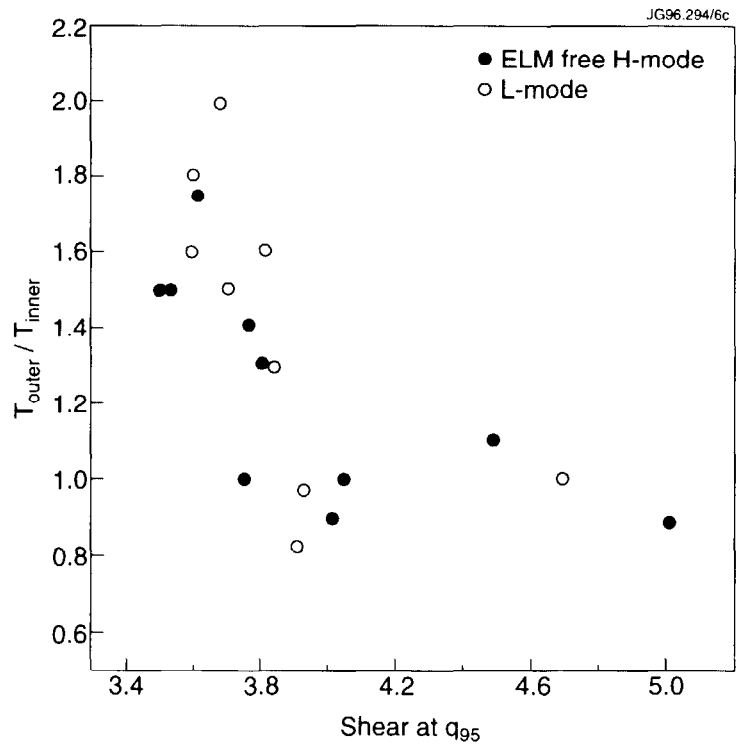

Figure 3 Ratio of the peak values of the outer to inner strike zone tile temperatures versus shear at q_{95} in .H-mode, ELM-free and L-mode.

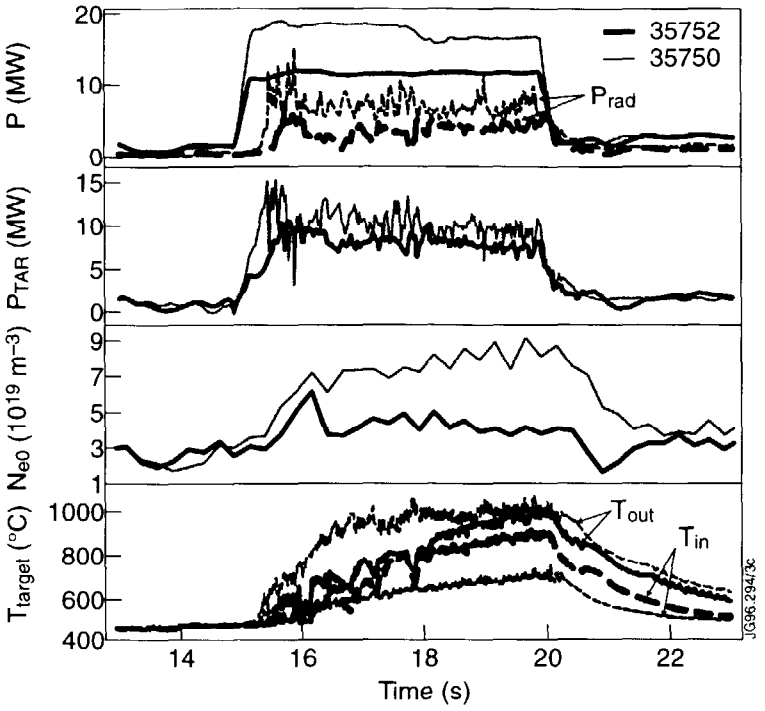

Figure 4 Time traces for shots #32969 and #33667: total input power, neutron reaction rate, D_α peak tile temperatures in the inner and outer divertors, and the ratios of outer to inner values in temperature and D_α integrated photon fluxes.

ICRH in Hot-Ion H-modes in JET

G.A.Cottrell, C.Gormezano, A.Howman, T.Jones, P.J.Lomas, F.Rimini,
R.Sartori, G.Sips, D.F.H.Start

JET Joint Undertaking, Abingdon, Oxfordshire, OX14 3EA, U.K.

In JET the NBI-produced ELM-free hot-ion H-mode plasma has generated the highest DD fusion reaction rate (R_{DD}) and therefore represents one of the leading modes for high fusion performance in the next DT phase of operations. The work presented here examines the role of adding ICRH to hot-ion H-mode plasmas.

RF IN HOT-ION H-MODES

The plasma has triangularity $\delta \cong 0.25$, expanded flux surfaces in the divertor and low recycling - conditions not optimised for ICRH coupling. Two discharges in Fig.1 had central ion temperatures $T_{i0} > 20$ keV and were pre-heated by similar LHCD powers to drive off-axis current, maintaining $q(0) > 1$, and suppress sawteeth prior to the main heating phase [1]. Pulse No. 34454 had both ICRF (6MW) and NBI (17MW) heating. ICRH was in the H-minority regime with near-axial resonance. The NBI-only reference (Pulse No. 34443), was heated with 16 MW. The discharges terminate by an ELM and sawtooth collapse. ICRH enhances R_{DD} as well as total plasma energy content - the latter is due to the increased heating power, an increased thermal confinement time, and the energy content of the ICRH fast ions. The fast ion content has been subtracted from the measured energy to estimate the thermal energy. The thermal confinement time was normalised to the ITERH93-P scaling law to derive the H-factor: $H = \tau_E/\tau_{93}$ where:

$$\tau_{93}\,(\mathrm{sec}) = 0.035\,(I_p/\mathrm{MA})^{1.08}\,(n/10^{19}\mathrm{m}^{-3})^{0.17}\,(B_T/\mathrm{T})^{0.32}\,(Q_L/\mathrm{MW})^{-0.67}(R/\mathrm{m})^{1.79}\varepsilon^{-0.11}\kappa^{0.66}M^{0.4}\,, \quad (1)$$

and Q_L is the heat flux across the boundary. Fig. 2 shows the thermal H-factor is up to 30% larger during the combined heating case. The TRANSP code was used to analyse the improvement in global confinement. At t = 16.7s and in the interval ($0.3 < r/a < 0.7$), there are similar values of electron thermal diffusivity; $\chi_e \sim (0.5 \pm 0.25)$ m^2 s^{-1} for both pulses, values typical of those in JET hot-ion H-modes. Thus the enhancement in the global confinement found when ICRH was added cannot be explained by a change in χ_e. However the ICRF heating profile is more peaked than that of the NBI. About 85% of the total ICRH power is found within r/a = 0.4 whereas only 45% of the total NBI power is found in that region. We

expect the more centrally condensed ICRH power deposition to increase the H-factor by only ~10% compared with the 30% measured increase. A model [2] which agrees with the experimental results is based on a neo-classical boundary condition at the separatrix, representing an edge transport barrier and is derived assuming the energy loss is related to direct losses of trapped ions. Q_L (= kn_a^2) is independent of the edge plasma temperature and is constant for constant edge density and,

$$dW/dt = P - Q_L \qquad (2)$$

For constant n_a, and input power P, $W = W_O + (P-Q_L)t$, where W_O is the energy content at the time of barrier formation. Thus both W and τ_E [= W/(P-dW/dt)], increase linearly with time: $\tau_E = \tau_O + (P/Q_L - 1)t$ where $\tau_O = W_O/Q_L$. Since Q_L is constant, we see from Eq.(1) that τ_{93} is only weakly dependent on time through the density evolution and predict that H should increase approximately in proportion with time. Moreover dH/dt depends on applied power,

$$dH/dt = (1/t93)\ (P/QL - 1). \qquad (3)$$

In Pulse No. 34454, we estimate Q_L ~ 10MW and calculate the fractional increase in dH/dt produced by ICRF finding the H-factor should increase ~1.4 times more rapidly than in Pulse No. 34443, in agreement with the observed ratio of ~1.3 of the slopes in Fig.2.

To exploit the potential benefit of this configuration, further optimisation is required. If we rate the performance of 3MA hot-ion H-modes in terms of R_{DD}, pulse No. 34454 ranks highly at 70% of the best performing 3MA discharge. This latter pulse was with NBI only and achieved its performance because the ELM-free period persisted for over twice as long. With lower recycling and improved stability [3], NBI can produce higher performance than in Pulse No. 34443. Adding ICRF/LHCD can certainly improve performance of the best NBI plasmas further, provided the ELM-free period is maintained, by optimising shear at the edge which normally decreases at low internal inductance.

HIGH ELECTRON TEMPERATURES

A record central electron temperature of T_{e0}= 15keV has been produced by RF + NBI heating in a hot ion H-mode (Fig.3). The H-mode was produced by 9MW of NBI which was progressively stepped down whilst the RF power was ramped up to 4MW. As a result, both the stored energy and the density reach stationary values during the H-phase. T_{e0} reached 15keV when $n_{e0} = 4 \times 10^{19} m^{-3}$ and T_{i0} = 12keV. H = 2.5 - 3 depending on whether the fast ion energy content is included. T_{e0} is plotted in Fig. 4 for hot ion and RF H-modes in 3MA triangular configurations and for RF-H-modes in 2.5MA discharges that simulate the JET "gas box" divertor configuration. For the hot ion cases, the data lie in the same region as those from pellet

enhanced performance H-modes (PEP + H) and hot electron modes obtained in the 1991/92 experimental campaign. Fig. 4 also shows, for comparison, the scaling of T_{i0} with P_{NBI}/n_{e0}. Similar values of T_{e0} and T_{i0} are obtained for the same values of P/n_{e0} implying similar core values of χ_e and χ_i. In 3MA, RF-only H-modes, T_{e0} increases linearly up to $P_{RF}/n_{e0} = 3 \times 10^{-19}$ m^3 MW. Above this, T_{e0} increases less rapidly possibly either due to fast ion orbit broadening of the electron heating profile or an adverse scaling of χ_e with temperature. A non-linear behaviour is evident in the 2.5MA "gas box" divertor data in which T_{e0} saturates at 9keV. TRANSP radial profiles of χ_e for the RF H-mode Pulse No. 34046 and the hot ion H-mode, Pulse No. 34242, at the time of maximum T_{e0} shows that, for the hot ion H-mode, χ_e is about half that in the RF H-mode. In the 2.5MA "gas box" divertor plasma with the highest P/n_{e0}, χ_e (r/a = 0.3) ~ $3m^2/s$ or about twice as large as that for the RF H-mode. For the hot ion H-mode χ_i ~1.5 χ_e. As T_e (and β_e) increase, the fraction of power absorbed by the electrons - by electron Landau damping + TTMP - also increases. This concentrates the power deposition in the core, ameliorating the orbit-broadening of the MeV fast ion heating profile. β_{e0} is a factor of two greater in the hot ion H-mode compared with the RF-only H-mode case. In Pulse No. 34242 the direct electron damping is 15% of the input power compared with 6% in Pulse No. 34046. A variation amongst the 3MA discharges was Pulse No. 35297 in which 5MW of ICRH with resonance ~ 0.3m on the high field side produced T_{e0} = 10keV at $n_{e0} = 2.7 \times 10^{19} m^{-3}$. This T_{e0} is higher than those obtained for the same P/n_{e0} with axial resonance in the 3MA RF-only H-modes (Fig. 4). TRANSP shows a core χ_e value similar to that for the hot ion H-mode and about half that for the RF-only H-mode.

SUMMARY AND CONCLUSIONS

The injection of fast waves into 3MA hot ion H-modes has increased the normalised thermal energy content by up to 30% compared with that achieved by beam heating alone. TRANSP analysis has established that there is no change in the thermal diffusivity. The enhancement is too large to be produced by the centrally localised nature of the ICRH alone, but is consistent with an interpretation in terms of an edge confinement barrier which maintains an energy loss independent of the plasma energy content. With this model, the H-factor increases with time at a rate which increases with the input power.

Central electron temperatures of ~ 15keV have been obtained in both RF-only and hot ion H-modes, close to the anticipated electron temperature in ITER at ignition, namely T_{e0} = 19keV. The temperature gradient and the electron toroidal beta are similar to the expected values in ITER, but the density in JET is three times lower. These data indicate that ICRH is an effective heating method - especially when its basic advantages - central heating independent of density and no fuelling at the edge - are fully exploited.

REFERENCES

[1] Ekedahl, A., et al. this conference

[2] Bak, P. et al, JET report JET-P(95)09, submitted to Nuclear Fusion.

[3] The JET Team, Plasma Physics and Controlled Fusion, 37 (1995) p. A359 - A370

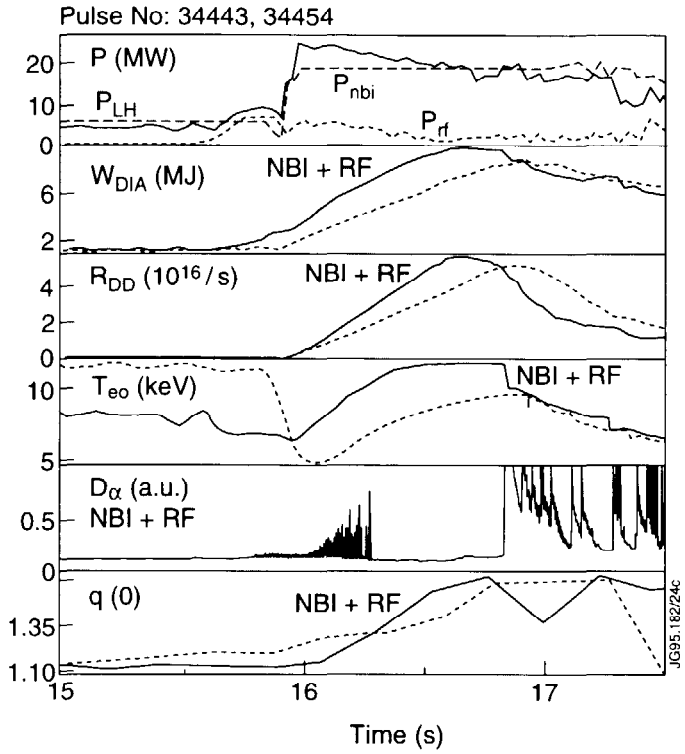

Fig.1. Parameters for two similar NBI hot ion H-mode plasmas (I_p = 3MA, B_T = 3.1T, q_{95} = 3.9) with (solid lines) and without ICRH (dashed lines)

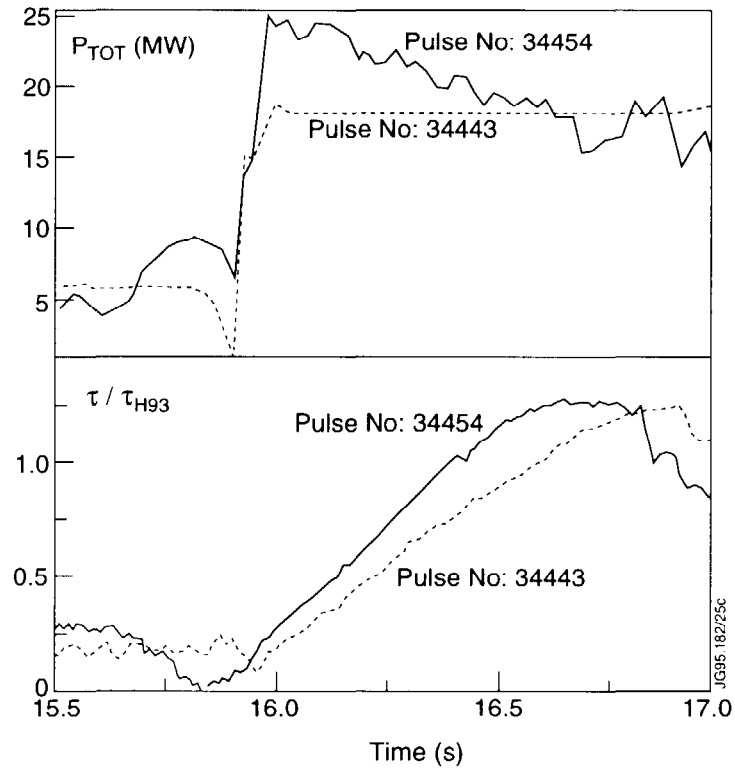

Fig.2. Upper: total power and lower: variation of normalised thermal H-factor for NBI and NBI+ICRH pulses hot ion H-mode plasmas of Fig.1.

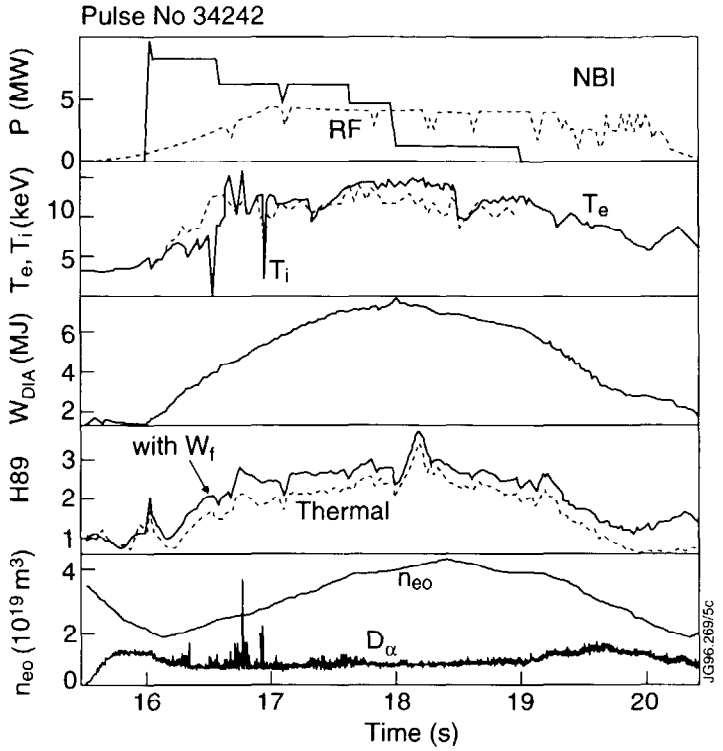

Fig.3. Variation of plasma parameters for a high central electron temperature discharge

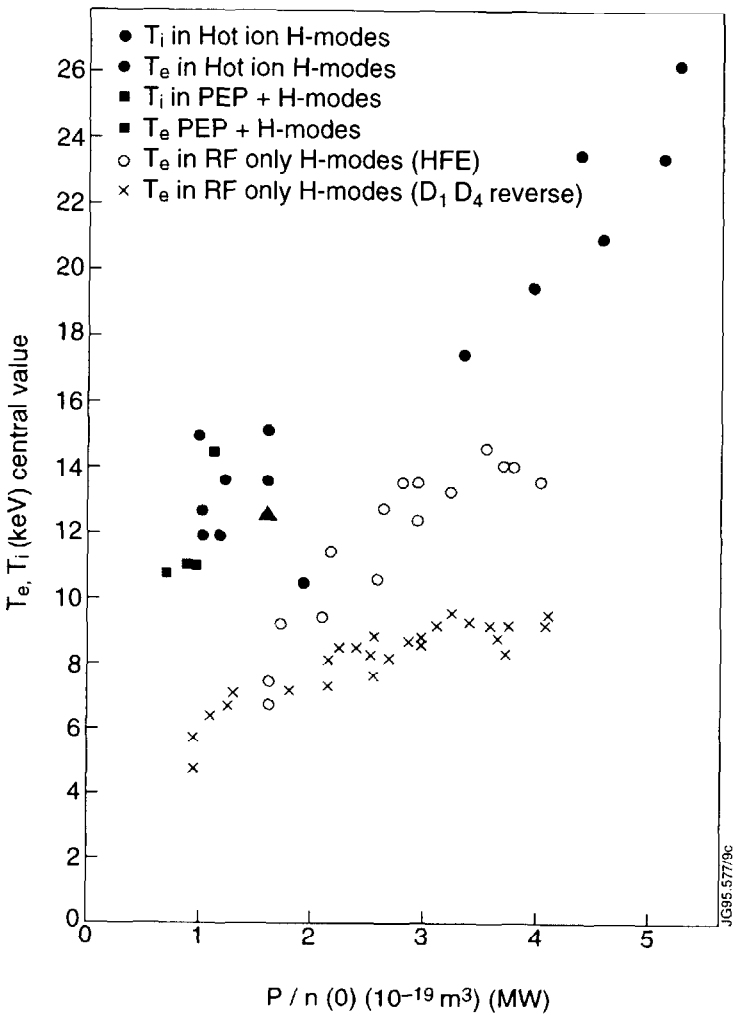

Fig.4. Central ion and electron temperatures versus applied power per particle: P/n.

Identification of the Physical Mechanism of Low-M, N=1 Mhd Mode Control in JET

M. De Benedetti[1], S. Ali Arshad, D. J. Campbell, G. D'Antona[2], A. M. Edwards[3], G. Fishpool, R. J. La Haye[4], E. Lazzaro[2], A. Santagiustina, F. Sartori, P. Savrukhin[5]

JET Joint Undertaking, Abingdon, Oxon, OX14 3EA, UK.
[1]Imperial College, London, SW7 2BZ, UK;
[2]Istituto di Fisica del Plasma, Euratom-ENEA-CNR, 20123, Milan, Italy;
[3]Culham Laboratory, UKAEA Technology, Abingdon, OX14 3DB, UK;
[4]General Atomic, San Diego, California, USA;
[5]Russian Research Centre 'Kurchatov Institute', 123182, Russia.

INTRODUCTION

Experiments have been performed in the JET pumped divertor to study the stability of plasmas in the presence of rotating applied fields and to investigate the possibility of stabilising disruptions by magnetic feedback control of the n=1 precursor mode.

EXPERIMENTAL ARRANGEMENT

The disruption feedback stabilisation system (DFSS) is based on a set of 4 saddle coils mounted inside the JET vacuum vessel, each consisting of 3 turns and covering approximately 90° toroidally and 60° poloidally (Fig. 1). Toroidally opposite pairs of saddle coils are coupled in an n=1 arrangement and each pair of coils is driven by an amplifier capable of operating in the range 0-1kHz at currents of up to 3kA, and in the range 1-10kHz at currents of up to 1/f kA/kHz. Low-m, n=1 rotating precursor modes are detected by a set of four pick-up coils, and a counteracting magnetic field is generated by the four saddle coils driven by the amplifiers with an appropriate amplitude and phase. A sophisticated digital controller, based on a set of six C40 processors, has been developed to integrate measurements from the magnetic pick-up coils and from Rogowski coils monitoring currents in the saddle coils. This controller, cycling at up to 200kHz, corrects the magnetic pick-up signals for known sources of error, such as the plasma response and vacuum vessel eddy currents, and calculates the amplitude and phase of the required currents in each pair of saddle coils.

THEORETICAL BASIS

The theoretical framework on which the experiment is based is a modified version of Rutherford's theory for the growth of a magnetic island. The island time evolution is given by

the well known equation: $\dot{w} = \eta\Delta'/\mu_0$ .For the control to be effective we require that $k \geq r_s\Delta'/2m$, where k is the ratio of the island magnetic field and that produced by the feedback system at the resonant surface (gain of the loop)[1].

EXPERIMENTAL DETAILS

A typical diverted equilibrium in JET has minor radius a=1.05m, vertical displacement Z_0=0.3m, elongation k=1.6, radius of the q=2 resonant surface r_s=0.75. A numerical code has been used to calculate the vacuum magnetic field components produced by JET saddle coils when the shape and position of the resonant surface is changed. m=2 magnetic fields on the resonant surface in the range $0.8 \div 2\times10^{-4}$ T are expected. Many different poloidal components are generated. Note that for rotating fields, the interaction with the wall reduces the field amplitude by about 40% and changes their phases with respect to the DC field.

In addition, the presence of a plasma column changes the detected magnetic field at the wall. This so-called 'plasma response' (Fig. 2) is a strong function of the equilibrium parameters of the plasma. However, it is found that the response in JET is independent of the driving frequency of the external fields while it is linearly proportional to the amplitude of the saddle coil current. Observations are consistent with a simple theory based on the assumption that each surface reflects the magnetic field component with which it is resonant.

PRODUCTION OF ROTATING TEARING MODES

Rotating tearing modes can be induced in the plasma by applying a rotating magnetic field. Such modes are locked to the external field frequency and reach an amplitude which is at least 3 times larger than naturally growing tearing modes before locking to the wall[4]. The threshold of mode generation is a function of the driving frequency and has a minimum around the natural frequency of the mode in the plasma, as expected on the basis of Hender-Fitzpatrick theory[2].

FEEDBACK CONTROL OF TEARING MODES

Initial experiments on the feedback stabilisation of naturally growing tearing modes were performed during the MkI divertor campaign. The applied current during these experiments was, however, severely limited, to approximately 30% of the design value, to avoid the possibility of electromagnetic resonances causing damage to the saddle coils. This limitation will be substantially eased in the future due to strengthening of the saddle coils and to improvements in the saddle coil protection system.

The feedback control loop was initially closed in vacuum to investigate the intrinsic stability of the system. and oscillations (even at low loop gains) were seen at around 13kHz.

This instability, which is due to the poor feedthrough compensation for high frequencies, can be prevented by filtering of the signals and by careful feedthrough compensation.

The loop was subsequently closed in the presence of naturally growing tearing modes which preceded density limit disruptions (Fig. 3). The controller generated fields with the correct phase and amplitude, indicating that the controller logic operated correctly and that the various corrections had been implemented properly. However, the magnetic islands usually grew too fast and locked before the precursor could be stabilised - it is not expected that the feedback control system will be powerful enough to suppress modes once they have grown to a sufficient amplitude for locking to the vessel wall (several Gauss in JET). A first estimation of the instability parameter Δ' and of the loop gain $2mk/r_s$ (Fig. 4) confirms that in the pulses studied an increased current capability, together with early detection of the growing islands, would be required to permit suppression of the precursor mode. Besides, with the present limitations in the system design, the modes were not controlled in speed and thus locking could not be prevented.

MODELLING OF FEEDBACK STABILISATION EXPERIMENTS

A numerical model[3] of the feedback control system, including a realistic model of the evolution of the internal mhd mode in the presence of externally applied fields, has been developed and detailed simulations of the control system have been performed. They reproduce with good accuracy the real behaviour of the system and can give useful information about the efficiency of the control. For example, In shot 35221 the natural growth rate of a magnetic island changed abruptly when the feedback was switched on. Comparison of real signals with simulated ones suggests that, being the mode close to saturation, the feedback gain was actually big enough to completely stabilise the island .

CONCLUSIONS

Initial experiments with the disruption feedback stabilisation system in JET have allowed many aspects of the physics of magnetic island evolution in the presence of externally applied fields to be investigated. In addition, the operation of the control loop has been explored and phenomena such as the vacuum feedthrough and plasma response have been quantified. Analysis of these first experiments indicates that the control loop functioned correctly, but that limitations in the power capability of the system, related to the mechanical stresses in the saddle coils, prevented the system from stabilising disruption precursor modes. Simulations of the operation of the control loop using a numerical model have yielded insight into the physics of the control problem and should allow an understanding to be developed of the role of various processes in determining the behaviour of magnetic islands during feedback stabilisation experiments.

On the basis of the operating experience, the control system has been substantially upgraded in advance of the forthcoming experimental campaign. An improved protection system has now been installed which should permit the system to reach its full current capability of 3kA. In addition, improvements in the trigger logic of the controller should allow modes with an amplitude of only 20μT at the vessel wall to be detected, a substantial improvement over the present detection threshold of 50μT. As a final significant improvement, the upgraded controller will be able to control not only the mode amplitude but also its rotation frequency, and this will provide an important additional feature to increase the likelihood of achieving mode stabilisation. Overall, the disruption feedback stabilisation system should prove a powerful tool, not only in addressing the question of disruption control, but also in studying the physics of tearing mode evolution in tokamak plasmas.

REFERENCES

1. Lazzaro E., Nave M.F., Phys. Fluids, 31 (1988) 1623.
2. Fitzpatrick R., Nuclear Fusion, 33 (1993) 1049.
3. Savrukhin P. et al., Numerical simulations of feedback control of coupled tearing modes at JET, Jet internal report JET-R(95)06.
4. Savrukhin P.et al., Effect of the error fields on plasma stability in JET and ITER, this conference.

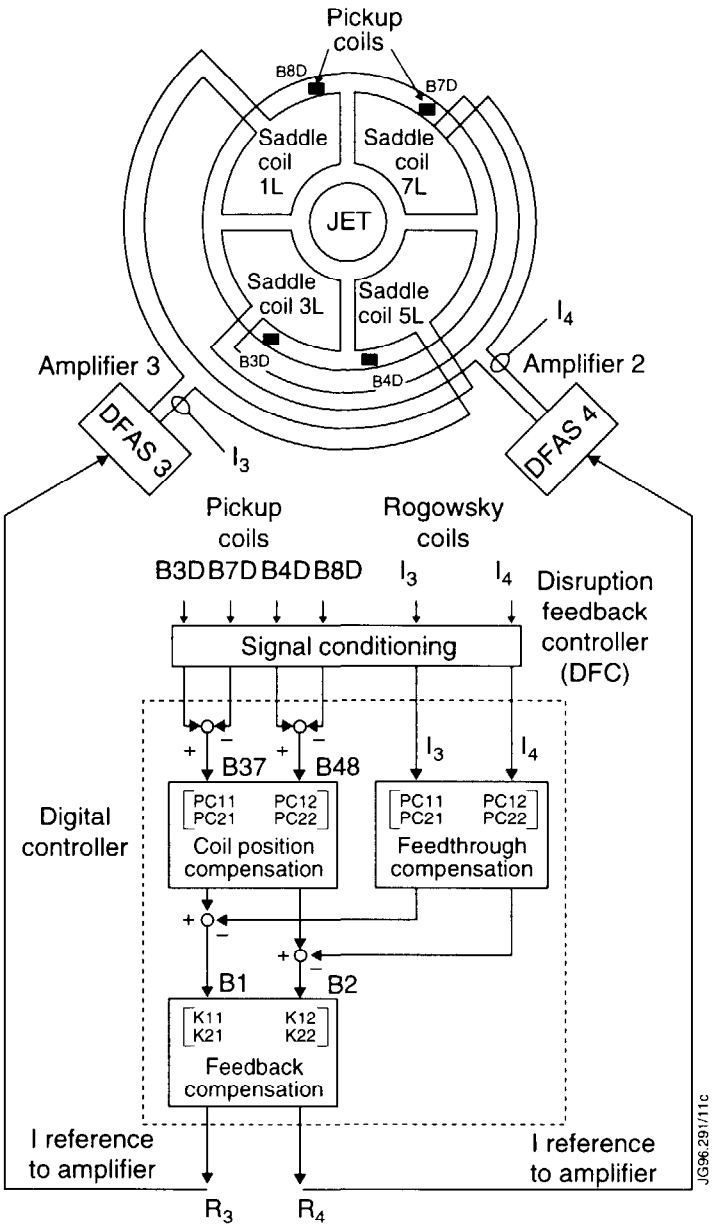

1. Scheme of the control system. Input signals from four pick-up coils and two Rogowsky coils are processed by a digital controller which drives two fast high-power amplifiers, each connected to a pair of saddle coils placed in the bottom of the vessel. The digital controller subtracts the feedthrough compensation from the detected signals and generates two reference signals proportional to the island magnetic field.

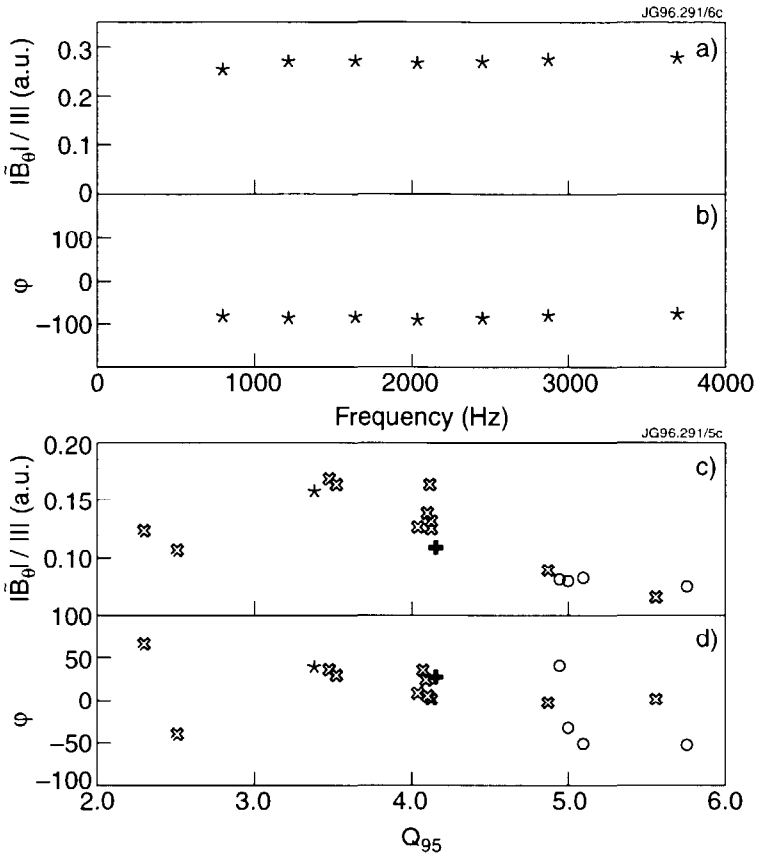

2. Measurements of the fast plasma response defined by the ratio of the reflected field measured at the outer limiter surface and the saddle coil current. a,b) Plot against the driving frequency: the response is independent on the frequency within the accuracy of the measurements. c,d) Phase and amplitude are plotted against the edge safety factor q(a). Points are scattered because the response is strongly dependent on the detailed equilibrium properties of the plasma.

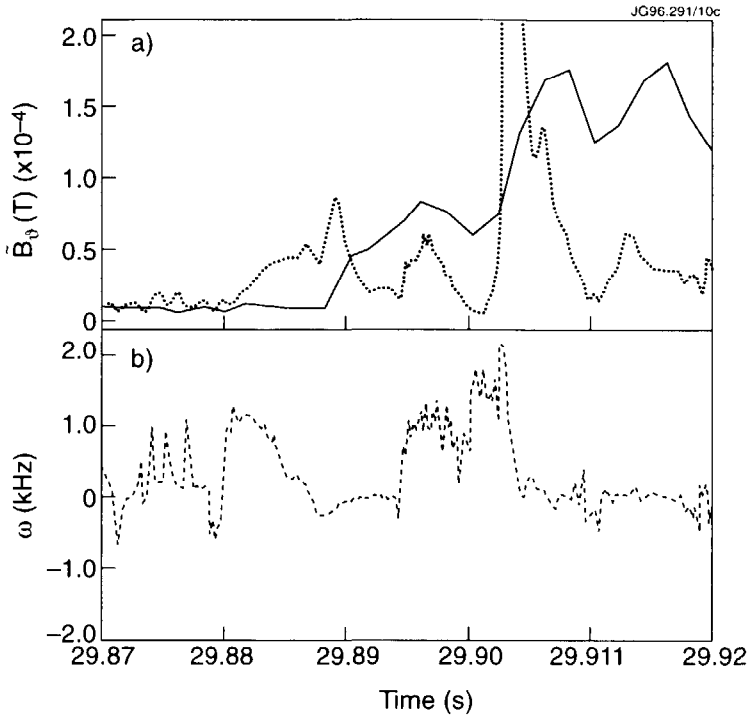

3. Feedback control in the presence of a magnetic island. a) $|\tilde{B}_\vartheta|$ at the wall (dotted), applied feedback field (solid). b) Estimated mode frequency ω. An island is present when ω is in the range 500-1500 Hz. The loop is closed at 29.89. The island grows too fast for the control loop.

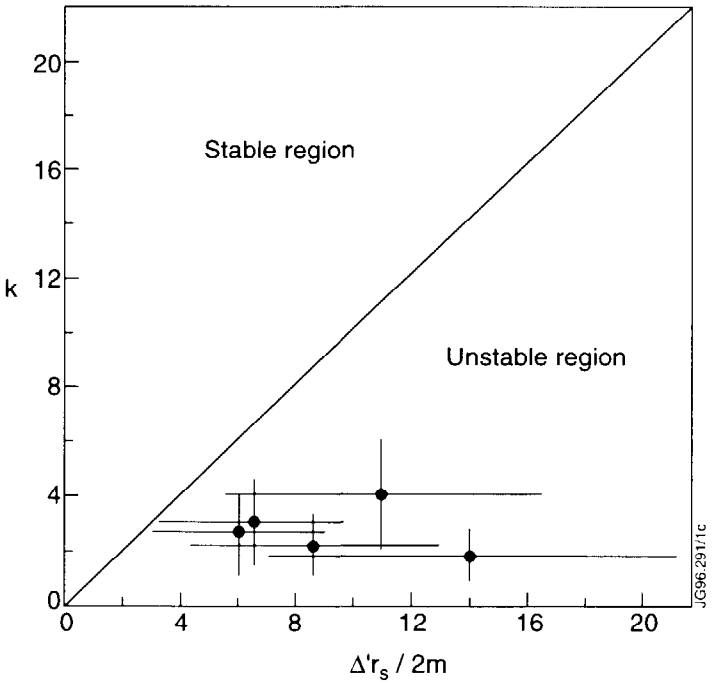

4. Stability parameters Δ′ plotted vs. $2mk/r_s$ for a series of discharges in which intrinsic modes were observed. Large error bars are due to large uncertainties in the measurements of the resistivity and of the growth rates of the modes. There is no clear evidence of disruption stabilisation.

Simulations of JET Hot-ion H-modes with a Predictive Code

H.P.L. de Esch, A. Cherubini, J.G. Cordey, M. Erba, T .T.C. Jones,
V.V. Parail, D. Stork and A. Taroni.

JET Joint Undertaking, Abingdon, Oxon, OX14 3EA, UK.

1. INTRODUCTION

The $1^1/_2$-D predictive code PRETOR [1] has been modified to include, among other things, neutral beams [2]. PRETOR has been used to simulate the JET hot-ion H-mode. This mode is obtained by injecting high power neutral beams into a low density plasma. This results in a hot plasma ($T_i \approx 20$ keV, $T_e \approx 10$ keV) which exhibits almost linearly rising stored energy, plasma density and neutron yield, until a termination event limits the performance [3].

Simulations of hot-ion H-modes considering different levels of recycling, various beam energies and deuterium and tritium beams will be described in this paper. A limiting pressure gradient (based on ballooning modes) and a limiting edge current density (based on external kink modes) have been considered in the modelling and are discussed. The simulations point the way to possible improvements in performance.

2. DESCRIPTION OF THE PRETOR MODELLING

Recent additions to PRETOR include a mixed Bohm - gyro Bohm transport model for the bulk transport and a one poloidal Larmor radius wide neoclassical H-mode transport barrier at the plasma edge [4,5]. The following leading terms in the edge can be identified:

H-mode barrier width: $$\rho_\theta = 0.457 \frac{\sqrt{A T_i}}{B_{pol}} \quad \text{(cm, keV, T)} \tag{1}$$

Heat and particle diffusivity: $\chi_i = \chi_e = D \sim \dfrac{n_i (Z_{eff} - 0.7)}{\sqrt{T_i B_{pol}^2}}$ (m^2/s, 10^{19} m^{-3}, keV, T) (2)

Heat flux $$q_{heat} \sim \frac{n_i^2 (Z_{eff} - 0.7)}{\sqrt{A}\, B_{pol}} \quad \text{does not depend on temperature} \tag{3}$$

Due to (3) the stored energy of a hot-ion H-mode can grow almost linearly in time until heat losses proportional to n^2 and Z_{eff} become comparable to the input power.

3. SIMULATION OF THE HOT-ION H-MODES

JET's neutron yield record shot 33643 (3.75MA/3.4T) has been modelled, keeping the volume average density evolution ($<n_e>(t)$) equal to the experiment: $d<n_e>/dt = 1.29\ \phi_{nbi}$. Time traces for $<n_e>$, Z_{eff}, total stored energy W_{tot} and D-D reaction rate R_{DD} are given in figure 1. Experimentally, the termination occurred at 13.38 seconds. This was simulated by increasing Z_{eff} at 13.38 seconds in line with the experimental Z_{eff} derived from charge exchange spectroscopy. An increase in Z_{eff} is modelled by puffing "carbon gas" into the edge of the discharge, so the *edge* Z_{eff} is even higher than the average Z_{eff} in figure 1, leading to a big increase in the heat loss (3) and irreversible termination of high performance.

There are also successful simulations of a hot-ion H-mode at 1.7MA / 1.5T (34488) and shots where the beam power decreased stepwise after $^1/_2$ or 1 second.

4. INFLUENCE OF THE RECYCLING

Plasma edge recycling of neutrals is quantified in this paper as the excess density rise over beam particle fuelling. It affects the performance because additional cold input gas must be heated. It also leads to higher density, increasing the particle/heat fluxes leaving the plasma (3) and reducing beam penetration. Improvements in performance are expected if excess edge fuelling can be reduced. Figure 2 shows two simulations of a plasma with the same equilibrium, power input and target density as 33643. One corresponds to the measured excess fuelling of 0.29, the other assumes no excess fuelling (every particle leaving the plasma is returned). No termination is assumed. It can be seen that stored energy and neutron yield reach much higher values for the low recycling case.

5. TARGET DENSITY PROFILE PEAKING

Two simulations were done using different values for the density in the plasma centre n_e (0), but with identical volume average densities $<n_e>$ at the start of the H-mode at 12.15 seconds, to test the effects of target density profile peaking. Centrally deposited beam particles diffuse towards the edge where the H-mode barrier prevents most particles from leaving the plasma. The two simulations (figure 3), showing cases with a very peaked and flat density profile appear to reach the same density profile in less than a second: *core particle transport wins over beam fuelling*. Indeed, experiments with peaked target density profiles have never yielded significant benefits over modestly peaked target density profiles.

6. PARAMETERISATION OF HOT ION H-MODE TERMINATION

Ballooning modes [6] and the external kink [7] impose a limit on the pedestal energy W_{ped} that can be sustained by the H-mode barrier. For the ballooning limit we have:

$$\frac{\nabla p}{\nabla p_{\max}} \sim \frac{W_{ped}/\rho_\theta}{B_{pol}^2} \sim \frac{W_{ped}}{B_{pol}\sqrt{AT_i}} \Rightarrow W_{ped} < Const\, B_{pol}\sqrt{AT_i} \tag{4}$$

All quantities in (4) refer to the edge. The giant ELM terminating some hot ion H-modes is thought to be a ballooning limit [3,6]. The "outer mode", which occurs in other hot ion H-modes is thought to be related to the external kink [3]. For this mode, the fraction of edge current related to total current is the critical parameter. If the edge current arises solely from the bootstrap current one has, using a simple expression for the bootstrap current [8] and the H-mode barrier width given by (1):

$$\frac{I_{boot}^{edge}}{I_{tot}} \sim \frac{\rho_\theta j_{boot}^{edge}}{B_{pol}} \sim \frac{\rho_\theta (T_e + T_i) q \nabla n_e / B}{B_{pol}} \sim \frac{W_{ped}}{B_{pol}^2} \Rightarrow W_{ped} < Const\, B_{pol} \tag{5}$$

The maximum pedestal energy achievable appears to be a function of the plasma current. The pedestal energy could conceivably be increased by driving an edge current in the opposite direction, e.g by *current rampdown.*

Simulations based on the present 33643 equilibrium; NBI power and target density are shown in figure 4, giving the D-D Reaction rate for various values of $d\langle n_e\rangle/dt$ and termination assumptions. The terminations pose a significant limitation to performance.

With lower recycling, modest improvements in performance are possible. Larger improvements can only be obtained if the ballooning limit can be increased (e.g. by using a more favourable magnetic configuration) ***and*** by using current rampdowns to delay the external kink.

7. DEPENDANCE ON BEAM INJECTION ENERGY

The mix of 13MW of 80 kV and 8 MW of 140 kV beams installed at JET is not suited for experiments on varying the beam energy in a hot ion H-mode, whilst keeping the total power constant. With PRETOR, however, we simulated 15 MW 80 kV NBI and 15MW 120 kV NBI cases (fig. 5). The high-energy beam case has a lower particle influx and reaches significantly higher stored energy and neutron yield than the low-energy beam case. Termination was by the "external kink" in the 120 kV beam case and by "ballooning" in the 80 kV beam case.

8. TRITIUM BEAMS

The present JET Experimental Programme includes a phase of DT plasma operation (Deuterium Tritium Experiment 1 - DTE1) to begin at the end of 1996. The tritium will mainly be supplied with the high energy neutral beams at JET (E≈140-160 keV). The use of tritium beams has several effects on the hot ion H-mode:

- More power. Available beampower will rise from 21 MW to 24-26 MW.
- Lower beam fuelling per MW injected power. This also means that the tritium concentration in the plasma is expected to remain low (≈30%).
- More plasma ion heating from the tritium beams.
- Power from α-particle heating provides plasma heating without associated density rise.
- An isotope effect arises from the H-mode barrier width (1).

All these effects increase the fusion performance and stored energy. Figure 6 shows simulations with tritium beams in a 33643-like plasma. In all cases the same ballooning and kink termination limits were kept as for 33643. No current ramps are applied. Stored energy, D-T neutron yield ($P_{fus}=2.82\cdot10^{-12}\ R_{DT}$) and tritium concentration are shown for:

- 25 MW NBI, consisting of 12 MW 160 kV T-beams and 13 MW 80 kV D-beams.
- 19 MW NBI consisting of 10.5 MW 150 kV T-beams and 8.5 MW 80 kV D-beams.
- 19 MW NBI consisting of 7.5 MW 140 kV D-beams and 11.5 MW 80 kV D-beams.

From fig. 6, performance can be expected to be higher with the tritium beams, even without invoking improvements to recycling and MHD stability.

9. CONCLUSIONS

PRETOR has proven to be suitable for simulating a variety of JET hot ion H-mode discharges and the following experimental observations were successfully simulated:

- Low recycling is beneficial for high performance.
- A peaked target density profile will flatten quickly in the hot ion H-mode.
- The increase in edge Z_{eff} observed in most terminations causes it to be irreversible.

The following predictions have been made:

- Low recycling improves the ballooning stability at the edge.
- Current ramp-down can be used to improve the kink stability.
- Increasing the beam energy leads to higher performance.
- Tritium beams increase the plasma stored energy due to a variety of reasons (sect. 8).

REFERENCES

[1] D Boucher and P-H Rebut, Proc. IAEA Techn. Comm. meeting on Adv. in Simulation and Modelling of Thermonuclear Plasmas, Montreal, Canada, 1992. IAEA Vienna (1993) 142.

[2] H P L de Esch et al, Fusion Engineering and Design 26(1995)589 or JET-P(93)103

[3] T T C Jones and the JET team, Plasma Phys. Control. Fusion 37(1995)A359

[4] V Parail et al, JET-P(95)49, to be published in Plasma Phys. and Control. Fusion.

[5] A Cherubini et al, This conference.

[6] T C Hender et al., Proc. 22nd Eur. Conf. on Contr. Fusion and Pl. Phys. (1995) 19C prt I p. 29

[7] G T A. Huysmans et al., 22nd Eur. Conf. on Contr. Fusion and Pl. Phys. (1995) 19C prt I p. 201

[8] J Wesson, Tokamaks (page 95). Oxford, Clarendon Press, 1987

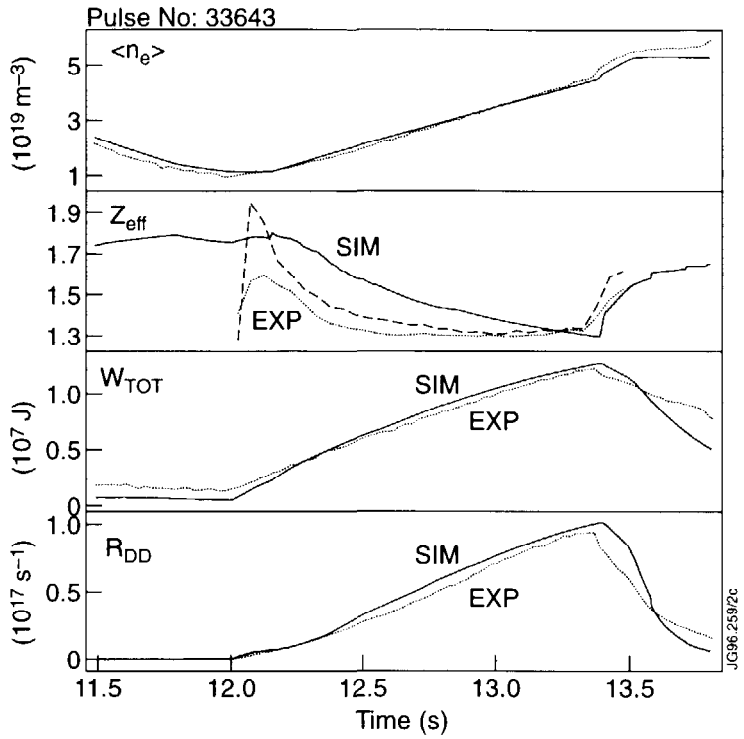

Fig. 1: Volume averaged density, Z_{eff}, Stored energy and D-D reaction rate for shot 33643. Simulation vs. Measurement

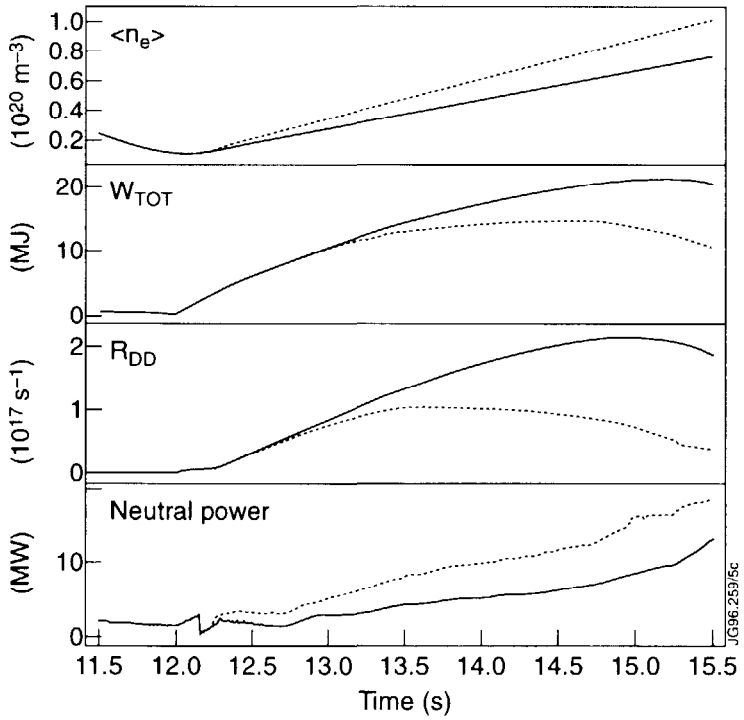

Fig. 2: Simulated density, Stored energy, D-D reaction rate and Power to heat neutrals: Solid lines: $d<n_e>/dt = \phi_{beam}$ dashed lines: $d<n_e>/dt = 1.29\ \phi_{beam}$

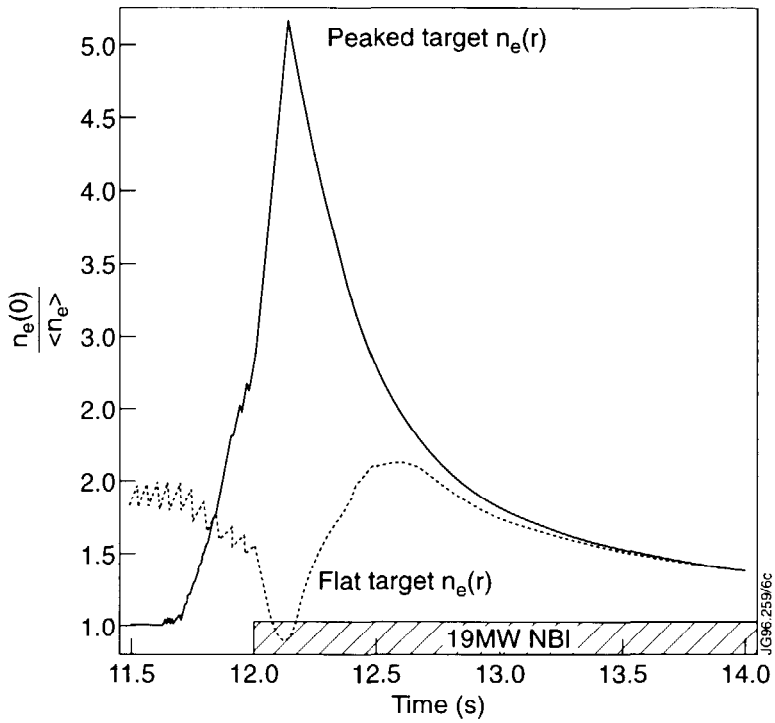

Fig. 3: Density profile peakedness ($n_e(0)/<n_e>$) evolution for two simulations: Solid line: Extremely peaked target density profile at the start of the H-mode. dashed line: Flat target density profile at the start of the H-mode.

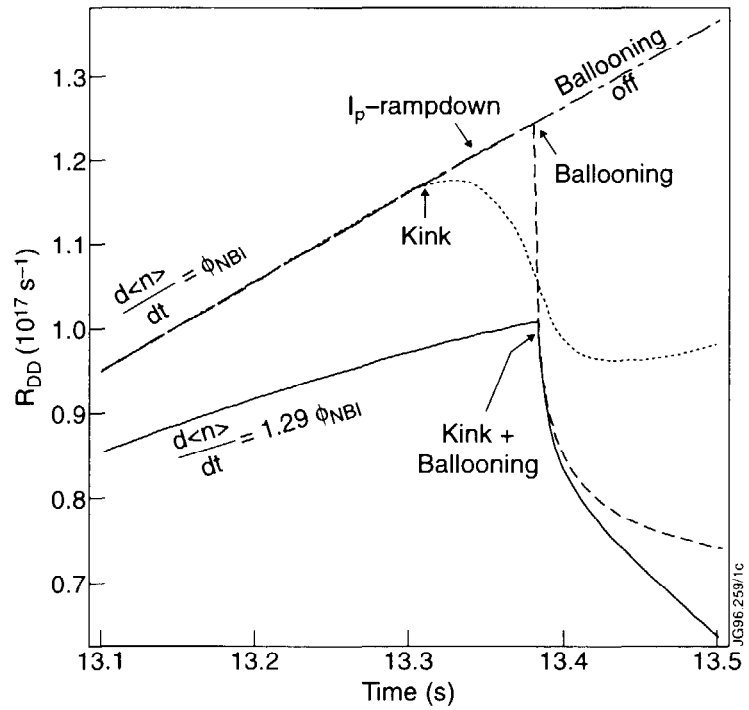

Fig. 4: Simulated D-D Reaction rates: Solid line: Benchmark for kink and ballooning. dotted and dashed lines: dotted: Kink and ballooning enabled. dashed: Current ramp to forestall kink dot-dash: Ballooning switched off

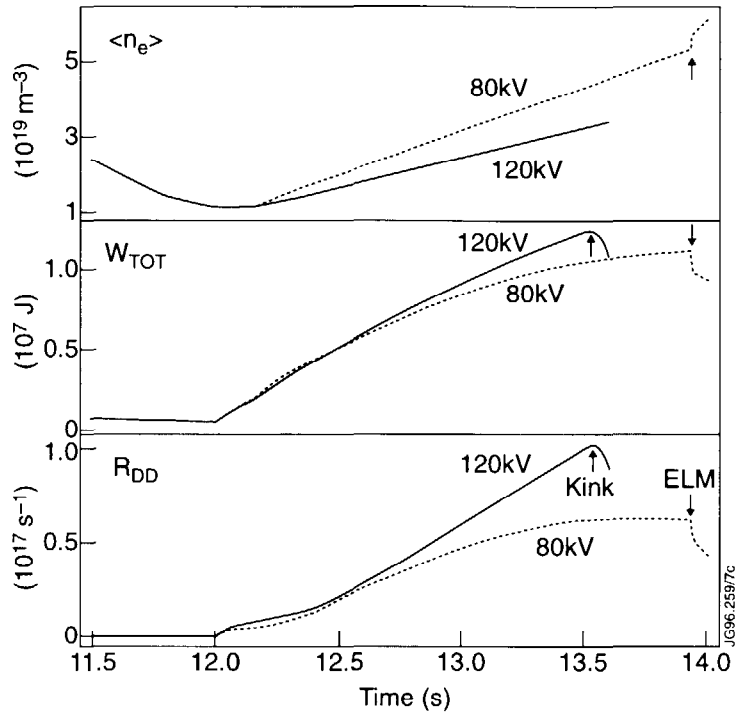

Fig. 5: Density, Stored energy and D-D Reaction rate for two 15 MW hot-ion H-mode simulations. Solid line: 120 keV Beams (kink termination) Dashed: 80 keV Beams (ballooning termination)

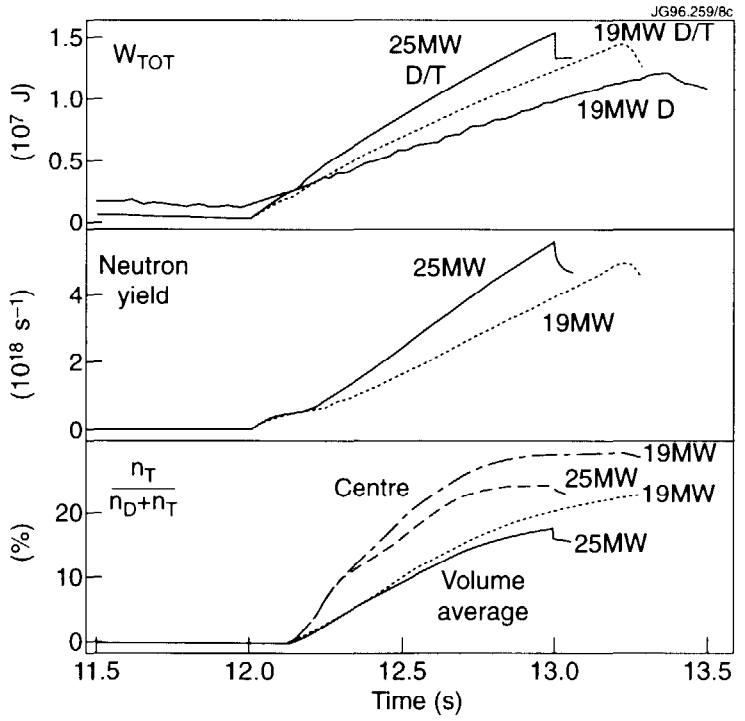

Fig. 6: Stored energy, D-T Neutron yield and tritium concentration for 25 MW D/T beams (solid lines) and 19 MW D/T beams. The experimentally measured stored energy using 19 MW deuterium beams is also indicated.

Profile Control in JET with Off-Axis Lower Hybrid Current Drive

A. Ekedahl1, Y. Baranov, J. Dobbing, B. Fischer, C. Gormezano, M. Lennholm,
V. Pericoli-Ridolfini2, F. Rimini, J. Romero, P. Schild, F. Söldner.

JET Joint Undertaking, Abingdon, Oxfordshire, OX14 3EA, UK.
[1] Electromagn. Field Theory, Chalmers Univ. of Technology, S-412 96 Göteborg, Sweden.
[2] ENEA, Centro Ricerche Energia Frascati, Via E. Fermi 27, 00044 Frascati (Roma), Italy.

1. INTRODUCTION

The full Lower Hybrid Current Drive (LHCD) system in JET was brought into operation in the 1994/95 experimental campaign. The maximum LH power coupled to divertor plasmas reached 7.3MW, using 8.2MW generated power. In profile control experiments 13s long LH pulses were applied, delivering a maximum energy of 68MJ to the plasma. Full current drive and sawtooth suppression have been obtained up to 3MA and analysis suggests that overdriving of the current is taking place in low density discharges with high LH power. For I_p>2MA the fast electron profile and LH driven current profile, as deduced from Fast Electron Bremsstrahlung (FEB) measurements, are peaked at approximately mid radius, as is suitable for current profile control. High power LHCD before the Neutral Beam heating phase has been used to study the effect of profile control on Hot-Ion H-modes.

2. CURRENT DRIVE EFFICIENCY

Full current drive with LHCD alone has been achieved in X-point configuration in the range I_p=0.7-3.0MA and $\bar{n}_e$ =0.7-2.0×$10^{19}$$m^{-3}$. Fig. 1a shows the theoretical current drive efficiency, calculated for the experimental conditions by a ray-tracing + Fokker-Planck code (LHCD code), against volume averaged electron temperature $\langle T_e \rangle$. No DC electric field effect was taken into account in these calculations. Fig. 1b shows the experimental current drive efficiency for discharges where full replacement of the plasma current was obtained, i.e. with zero resistive surface loop voltage. The variation in Z_{eff} was small and has not been taken into account in the graphs. For line averaged density $\bar{n}_e$ >1.1×$10^{19}$$m^{-3}$ the experimental and theoretical efficiency are in agreement. The efficiency reaches η_{CD}=0.25-0.30×$10^{20}$$m^{-2}$A/W, a value which is in accordance with the requirements for advanced tokamak scenarios in ITER. The calculated efficiency (Fig. 1a) saturates above $\langle T_e \rangle \approx$1.5keV and for $\bar{n}_e$ <1.1×$10^{19}$$m^{-3}$ the efficiency drops slightly. An explanation for this behaviour is a shift of the absorption towards lower energy electrons, i.e. $n_{\parallel}$ upshifts, once a saturated plateau in the electron distribution function has been formed. The experimental efficiency (Fig. 1b) deduced from measurements of the surface loop

voltage decreases with temperature for $\langle T_e \rangle > 1.5$keV and $\bar{n}_e < 1.1 \times 10^{19} m^{-3}$. In addition, the hard X-ray emission from the fast electrons appears lower than expected, especially at high LH power ($P_{LH} > 5$MW). A plausible explanation for the observed result is the local overdriving of the current in discharges with excessive LH power. A negative DC electric field, which counteracts the LH wave field, is then induced in the plasma region at approximately mid radius where the LH power is deposited.

The radial profile of the parallel electric field has been calculated, applying the technique by Forest et al. [1]. The method utilises the radial current profile, $j(\rho)$, determined by magnetic measurements, including Faraday rotation, and EFIT equilibrium reconstruction. The parallel electric field profile can be obtained by evaluating the time derivative of the poloidal flux. Fig. 2a shows the loop voltage profile for a 2MA discharge with $\bar{n}_e = 0.7 \times 10^{19} m^{-3}$ and $P_{LH} = 5.5$MW. A reversed loop voltage is obtained in the region $0.1 < \psi < 1.0$ and in the region outside $\psi = 0.5$ the loop voltage is ~ -0.15V, which suggests that the current is being overdriven. There is a discrepancy between the evaluated loop voltage at $\psi = 1.0$, which is almost -0.2V, and the measured surface loop voltage, which remains close to zero. A possible reason is that the measured surface loop voltage is not representative of the value at the plasma surface itself, but at a point further outside the plasma.

The loop voltage profile shown in Fig. 2a was used as input for a simulation of the discharge with the ray-tracing + 2D Fokker-Planck code. The hot conductivity term reached a maximum of $1.6 \times \sigma_{Spitzer}$ at $\psi = 0.6$ and the resulting current was 2.3MA. For comparison, when $V_{loop} = 0$ was used in the calculation the driven current amounted to >5MA, see Fig. 2b. The output of the code was then used to calculate the expected FEB emission and to compare it with the measured emission. A reasonable agreement between experimental and calculated line averaged brightness was obtained when the current profile corresponding to 2.3MA and $V_{loop} < 0$ was used. This analysis suggests that the current is being overdriven, but an accurate calculation is difficult in these conditions and there are still discrepancies between measured and calculated current drive efficiency in some discharges.

3. PROFILE CONTROL EXPERIMENTS

Full suppression of sawteeth has been achieved with LHCD up to 3MA in conditions close to full current drive (Fig. 3). At low density, a peaked electron temperature profile and high central electron temperature (T_{e0} above 8keV) have been obtained. This high temperature phase is characterised by very low MHD activity.

LHCD has been used to modify the current profile before the formation of Hot-Ion H-modes in order to raise q_0 above unity and to suppress sawteeth during the high power NBI or NBI+ICRH phase. In a first campaign the ELM-free period was reduced when preceding LH profile control was used, probably due to the decrease in edge shear and triangularity associated

with the broadening of the current profile. In a second campaign the plasma configuration was modified to keep a higher edge shear, with the result that the length of the ELM-free period was similar both with an without LH profile control. Fig. 4 shows the result of the second experiment. The sawteeth were suppressed during the NBI phase and in some cases there was a softening of the MHD activity, which prevented the decrease of the neutron yield. The ELM which terminated the high performance phase was delayed.

4. SUMMARY

Full current drive with LHCD alone has been obtained up to 3MA, resulting in current drive efficiency η_{CD}=0.25-0.30×$10^{20}$$m^{-2}$A/W. Analysis suggests that overdriving of the current is taking place in low density discharges ($\bar{n}_e$ <1.1×$10^{19}$$m^{-3}$) with high LH power ($P_{LH}$>5MW), but there are still discrepancies between experimental and calculated current drive efficiency in some discharges.

Sawtooth suppression and strong peaking of the electron temperature profile have been obtained up to 3MA in low density discharges. Promising results have been achieved with LH profile control before Hot-Ion H-modes and forthcoming LHCD experiments will aim at improving MHD stability and confinement of Hot-Ion H-modes and at studying shear optimised scenarios.

ACKNOWLEDGEMENT

The authors thank Drs C. Petty and W. Zwingmann for help in the analysis of the loop voltage profiles.

REFERENCE

[1] C.B. Forest et al., Phys. Rev. Lett. **73** (1994) 18.

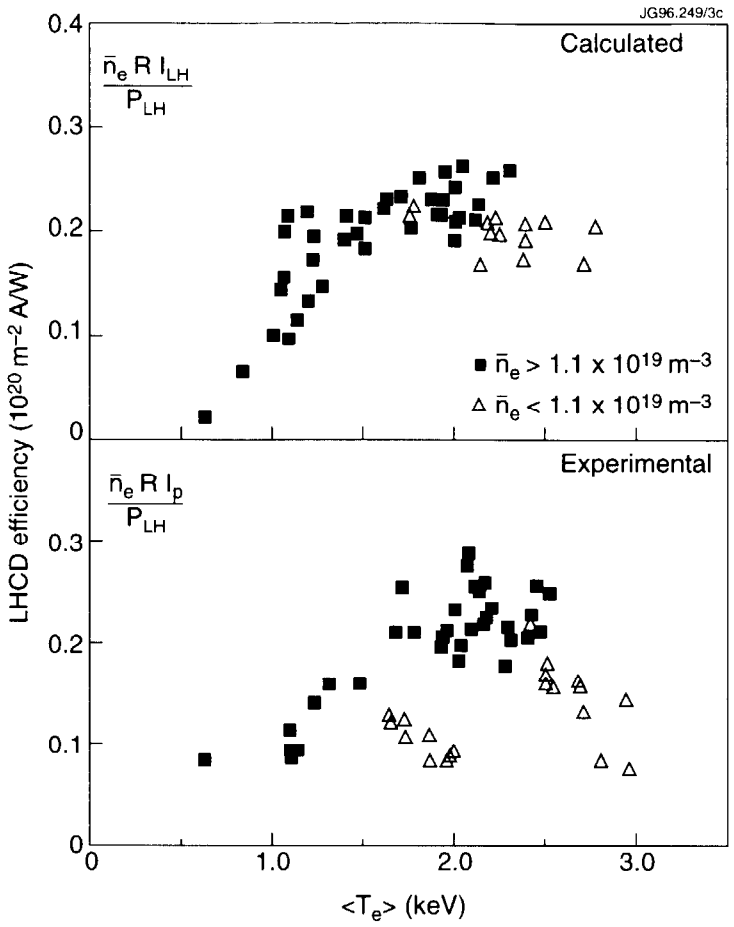

Fig. 1. a) Theoretical η_{CD} without DC electric field effect, calculated by the LHCD code. b) Experimental η_{CD} for full current drive shots.

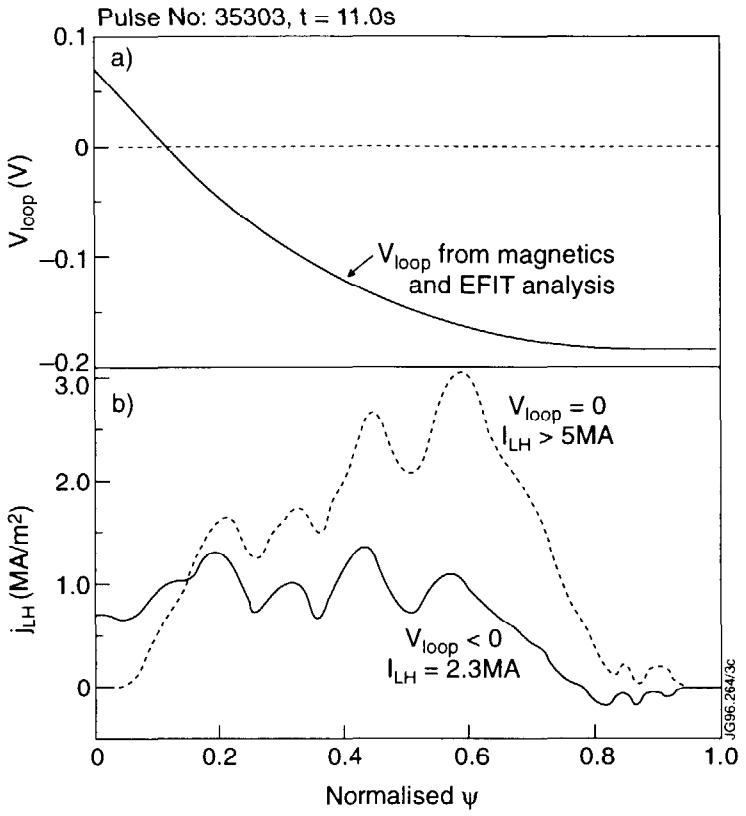

Fig. 2. a) Loop voltage profile from j(ρ)-analysis. b) Calculated LH current profiles for $V_{loop}<0$ (from j(ρ)-analysis) and $V_{loop}=0$.

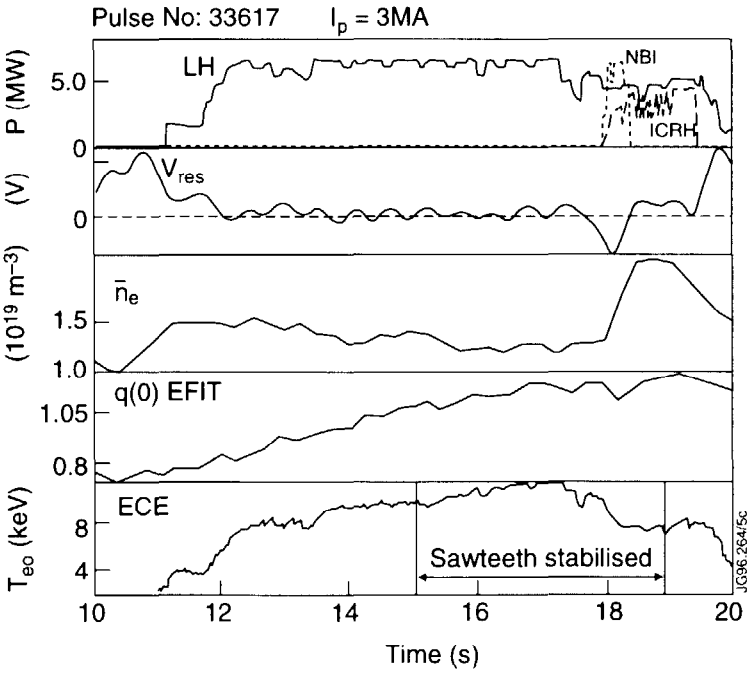

Fig. 3. Sawtooth stabilisation with LH profile control in a 3MA discharge. Full current drive is also obtained.

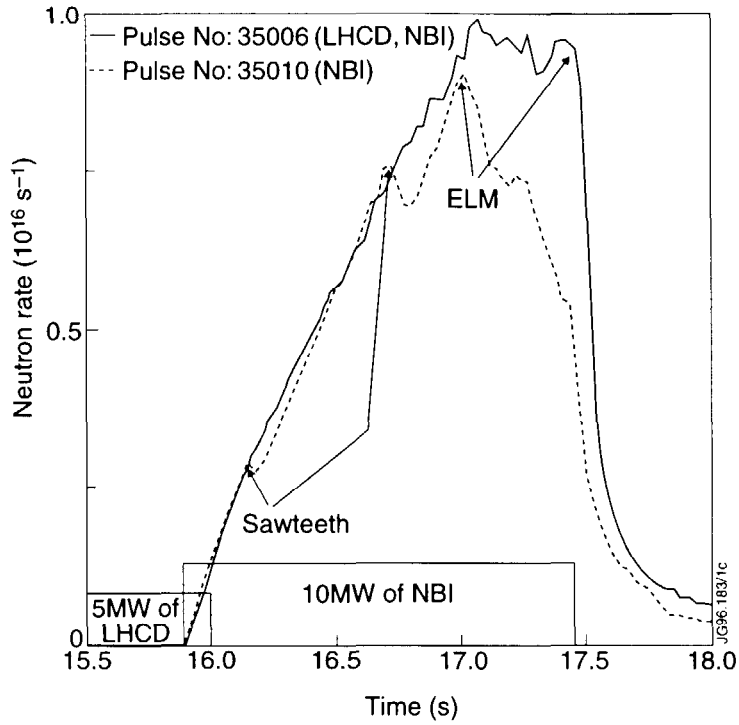

Fig. 4. Time evolution of the neutron rate in Hot-Ion H-modes with and without preceding LH profile control.

Properties of Giant Elms

R.D. Gill, B. Alper, S. Ali-Arshad, A. Cheetham, N. Deliyanakis, A.W. Edwards, G.M. Fishpool, I. Garcia-Cortez, L.C. Ingesson, J. Lingertat, L. Mayaux, O. Menicot, R. Monk, L. Porte, F. Rochard, M. Romanelli, A. Rookes

JET Joint Undertaking, Abingdon, Oxon., UK

Elms are a persistent feature of tokamak configurations which include an X-point. Their phenomenological properties have been recently reviewed[1])but although their effects on tokamak plasma confinement and on the termination of high performance discharges are well known, many details of their structure and causes remain obscure. Several different sorts of elms have been classified, but this paper will confine itself to consideration of giant or type 1 elms. These elms cause the largest disturbance to the plasma and therefore give the best prospect of experimentally determining the detailed changes which occur as the elm progresses. A very detailed examination of the structure and time development of the elms has been made possible because of the development of the CATS data acquisition system[2]) which allows the simultaneous measurement at high time resolution (4μs) and synchronisation of the data from a number of diagnostics including ECE, reflectometry, soft X-rays, D_α, Langmuir probes, infrared camera and the magnetics including the diamagnetic loop. The high time resolution is essential for these investigations as the giant elm has a very fast onset with the fast diagnostics all responding within a few μs. Much of the very detailed information has come from the multicamera soft X-ray system[3]) which has 6 compact cameras (fig. 1) viewing the plasma from different directions in the same poloidal plane and a further vertical camera displaced toroidally by $3\pi/4$. Each camera consists of a pair of 35 element silicon diodes with each element 4 x 1mm. The detectors have been calibrated with an X-ray tube and view the plasma through common pinholes. Except for the vertical camera, alternate detector elements only are used. The lines of sight of the detector were determined using a HeNe laser to survey their positions.

The giant elms considered occur during neutral beam heated divertor discharges with P_{NI} = 17MW, B_ϕ = 3.1T, I = 3MA, elongation of 1.8, T_e = 11keV, and $n_e = 10^{19}m^{-3}$. The elm is frequently associated with the termination of the period of good confinement in JET[4]) and has strong global effects on the plasma. In particular, it reduces the total plasma energy as measured by the diamagnetic loop by up to 7% (~ 0.6MJ) and this is reflected in a reduction of the electron temperature across the whole plasma profile. During the rapid part of the elm (fig. 2) the ECE measurement of T_e typically shows a pronounced very fast (40μs) spike many times the thermal value, with the largest enhancement at the plasma edge, followed by a dip to below

the thermal level for a longer time. It is believed that the spike is due to the formation of a non-thermal electron distribution function following the partial mixing of hot and cold electrons. This modifies the emission and absorption of the cyclotron radiation[5]). The rapid onset of the spike is too fast for it to be caused by the formation of a group of non-thermal electrons with energy very much greater than T_e. The dip is probably due to the production at the edge of a high density region following the large particle influx which is inferred from the H_α measurements.

There do not seem to be precursors to the elms, although there is considerable activity seen by the mhd coils, particularly bursts of activity at 25-30 kHz probably with n = 3. Some of the giant elms occur during these bursts, but others do not, showing that they do not play an essential role in their initiation. This activity is not observed on the ECE or soft X-rays. The magnetics also show that the movement of the plasma caused by the elm is no more than 1-2 cms at the separatrix. The reflectometer observes a coherent mode at 25kHz at the plasma edge, possibly outside the separatrix. The mode stops at the elm and then becomes broad-banded activity. The plasma edge density is seen to increase. Data[6]) from Langmuir probes and an IR camera which views the divertor region shows strong movement of the divertor strike points with their separation increasing from ~ 30 to 45 cm during the elm, and this is confirmed by the X-ray measurements.

The most detailed information on the rapid development of the elm comes from the soft X-ray data. The view into the divertor from the vertical camera shows the main features (fig. 3) as (i) very rapid onset of emission (20μsec), (ii) very localized emission from four channels, (iii) time structure of ~ 30μsec within the total elm envelope of 250μsec. Two of the channels (15 and 18) may be identified with the divertor strike zones. This is confirmed by correlation of the position and time behaviour of the emission with the data from other cameras also with a divertor view. X-ray emission from the divertor implies the presence of energetic electrons (> 500 eV) in this region. Calculations suggest that the observed intensity is consistent with the observed loss of plasma energy if the measured emission is caused by bremsstrahlung radiation of the former plasma electrons with the C divertor tiles. The toroidal camera shows that this emission is not toroidally symmetric, and the first burst of emission is sometimes at one poloidal position and sometimes the other. However the first burst of emission is coincident with the ECE and the H_α spikes.

The other X-ray spikes are somewhat more problematical. Enhanced emission is seen from several regions near the plasma edge but within the separatrix. These regions seem to coincide with the parts of the machine structure which are closest to the separatrix leading to the idea that enhanced impurity influx from these regions may take place during the elm. The structure of these regions of emission has been examined with a pixel tomography method originally developed by Fuchs[7]) which clearly shows (fig. 4) the different regions of enhanced emission. The tomography was carried out on data from which the background intensities

before the elm had been subtracted so that the figure shows only the changes which take place during the elm. The very rapid increase in X-ray emission in the divertor is a very prominent feature.

In conclusion our results show that giant elms are very rapid events with a complex structure which are neither confined to the plasma edge nor localised in the divertor region. They do not have a unique precursor mode. A possible explanation for the observations is that currents in the divertor region lead to a movement and modification of the magnetic structure at the X-point. There is a clear need to develop a theoretical model of the elms which is able to explain these detailed observations.

REFERENCES

1. H. Zohm, Plasma Phys. Control Fusion, 38, (1996) 105.
2. A.W. Edwards et al., APS Topical Conference on High Temperature Plasma Diagnostics. Rochester. 1994.
3. B. Alper et al., EPS Conference on Controlled Fusion and Plasma Physics, Montpellier, (1994) 1304.
4. M.F.F. Nave et al., Submitted to Nuclear Fusion.
5. J. Hastie, private communication.
6. H. Lingertat et al, Conference on Plasma Surface Interactions, St Raphael, 1996.
7. C.F. Fuchs et al., EPS Conference on Controlled Fusion and Plasma Physics, Montpellier, (1994) 1308.

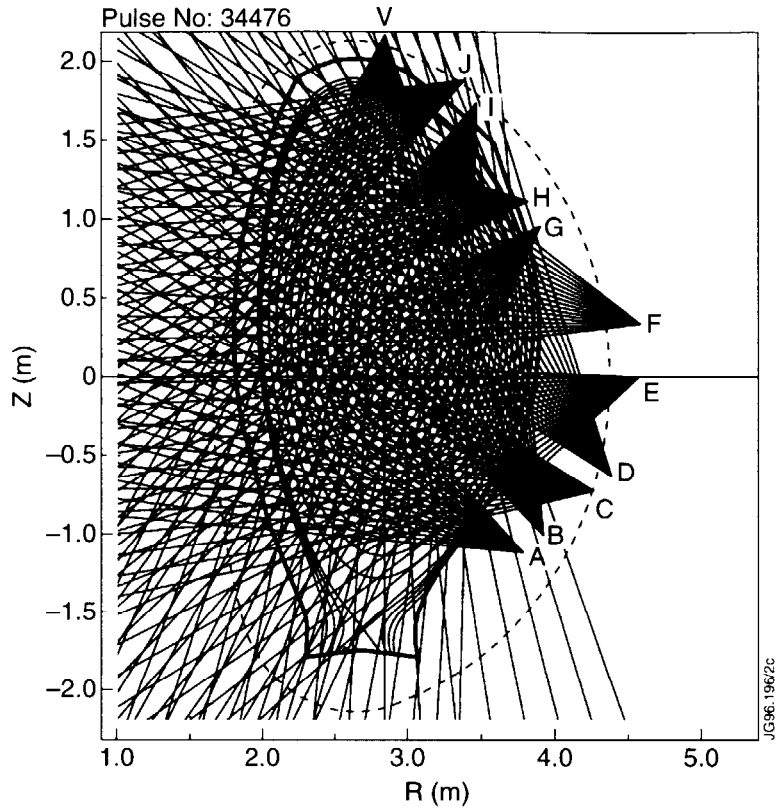

Fig. 1 The lines of sight of the individual detectors of the soft X-ray cameras are shown in relation to the JET divertor configuration.

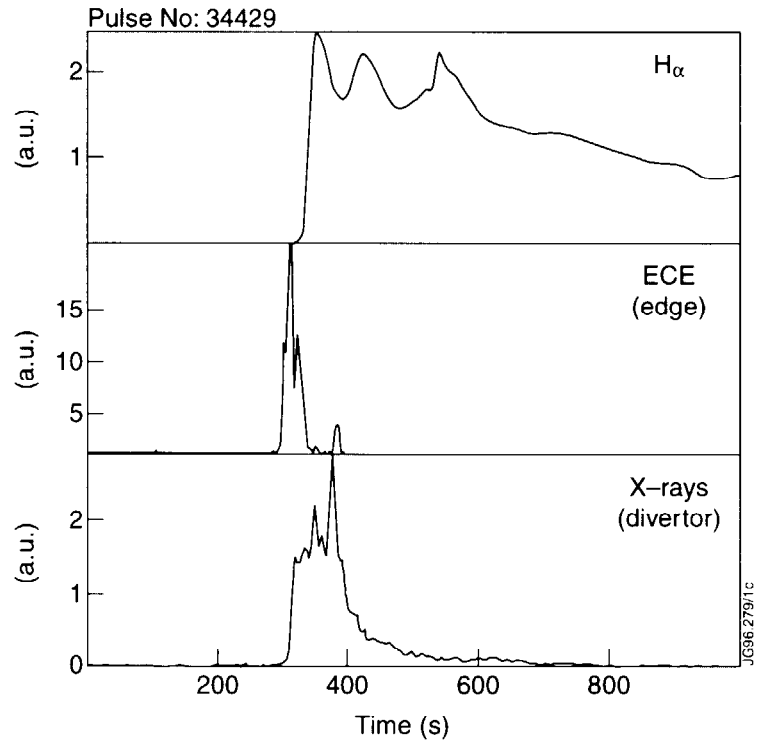

Fig. 2. The fast time development of a giant elm as seen on the ECE, a soft X-ray channel viewing the divertor and the H_α radiation.

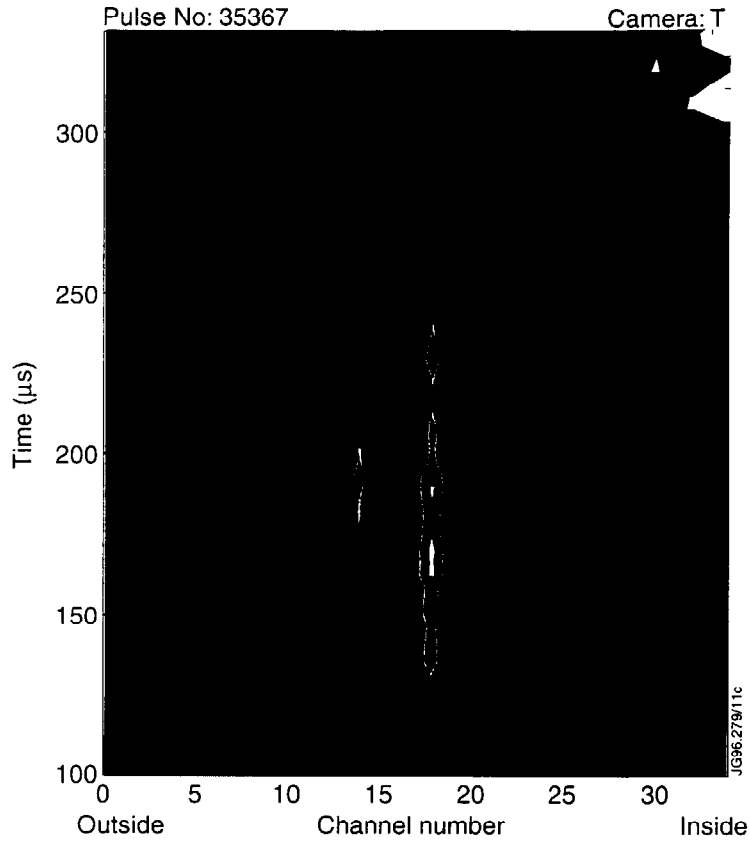

Fig. 3 Contour plot of soft X-ray data from the vertical camera during an elm. The background signal just before the elm has been subtracted from each channel. Complex time and spatial structure can be seen (left).

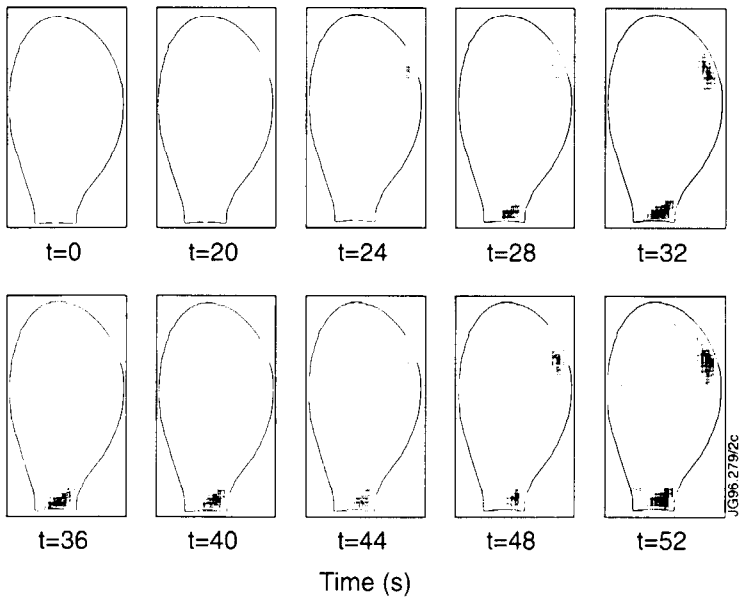

Fig. 4. Tomographic reconstruction showing the initial stages of the elms development. Again the background has been subtracted form all channels and the changes during the elm have been reconstructed (below).

Analysis of VUV Ne radiation in the JET divertor during Ne injections

R. Guirlet*, R. Giannella, L. Horton, K. Lawson†, A. Maas, C. Maggi, M. O'Mullane†

JET Joint Undertaking, Abingdon, Oxfordshire, OX14 3EA, UK

*Permanent address: DRFC/SPPF, Association EURATOM-CEA sur la Fusion, CE CADARACHE,

St-Paul-lez-Durance, France

†UKAEA Government Division, Fusion, Culham, Abingdon OX14 3DB, UK

ABSTRACT

To enhance the radiated power fraction at the edge of a tokamak plasma without degrading the confinement parameters of the bulk, impurity seeding is a classical method. Although neon is one of the most often used impurities, its ability to radiate at the edge without contaminating the plasma itself is still under discussion. This paper presents a detailed estimate of the neon radiated power in the JET Mark I divertor together with an aspect of the Ne behaviour as a function of the Ne density in the bulk using the data provided by a VUV spectrometer viewing the divertor region.

The main diagnostic for this study is an absolutely calibrated double VUV spectrometer (SPRED) directed to the inner part of the divertor horizontal target (fig.1). It is equipped with 2 gratings (450 g/mm and 2105 g/mm) giving a wavelength range of 150Å $\leq \lambda \leq$ 1450Å. The time resolution is 11 ms - 50 ms per spectrum. To extract the various line intensities of D, He, C and Ne, a multigaussian fitting code is used in order to deal with the severe blending of most of the Ne lines. The Ne II resonance line (461Å) intensity is not estimated because of the blending with a C III line in a particularly complex part of the spectrum. The main Ne IX and Ne X lines lie outside the wavelength range of the detector but they radiate in the bulk rather than in the divertor. For each of the other ionisation stages the most important lines are measured. To cross-check the results a bolometer line of sight (BLOS) viewing approximately the same region of the inner target plate is used. The divertor contribution is estimated by subtracting the signal measured by a line of sight viewing only the bulk.

ESTIMATE OF THE POWER RADIATED IN THE DIVERTOR:

To estimate the power radiated in the inner strike point region, a low-Ne content, L-mode discharge ($<n_e>=4.4\times10^{19}m^3$, fig.2) with a small Ne puff is chosen. The X point position is swept. The estimate is made from the D I, He II, CII to IV and Ne III to VIII line intensities.

One of the largest uncertainty comes from C IV because the resonance line (1549Å 2p-2s) lies outside the wavelength range of the spectrometer. The ratio of 2 other C IV lines (312Å 3p-2s and 384Å 3d-2p) is used to determine (with ADAS [1]) a value of T_e and subsequently the resonance line intensity. As far as Ne is concerned the largest error is due to the lack of information about the Ne VII triplet configuration. However the maximum contribution of the triplet resonance line to the radiated power is estimated by ADAS to be 16% of the singlet resonance line. It is observed that the Ne III to V line intensities are strongly modulated by the sweeping, indicating a peaked distribution along the target direction, whereas the Ne VI and VIII intensities are not or weakly modulated (the Ne VII line used in fig.2d is thought to be blended, thus giving an overestimate of its intensity and a fake correlation with the sweeping). This is thought to be due to the location of the higher ionisation stages farther from the divertor target or even above the X point. The radiated power is more or less evenly distributed between the lower (III to V) and the higher (VI to VIII) ionisation stages of Ne. This is in agreement with the bolometer measurements showing that half of the additional radiated power is radiated above the X point. The electron temperatures measured from the line ratios available give Te(C III) =6±4eV, Te(C IV) = 9±4eV, Te(Ne V) = 11±4eV, Te(Ne VI) = 12±6eV. The similarity of the latter two is surprising since only Ne V is modulated by the sweeping. It might be due to the weak sensitivity to T_e of the Ne VI line ratio we use here ($I(2s2p^2\ ^2S\text{-gs})/I(2s2p^2\ ^2P\text{-gs})$). The total radiated flux (fig.2c) estimated from the SPRED measurements, and in particular the extra flux after the Ne puff, due almost entirely to Ne (75%) and deuterium (25%), are in good agreement with the power flux measured by the BLOS. In all the pulses analysed here, the ratio of the BLOS signal to the radiated power in the X point region (calculated by an Abel inversion of the bolometer array signals) is constant as a function of time, due to the fact that the emission comes mainly from the region seen by the BLOS. The agreement between the SPRED and the BLOS being good, this ratio can be used to convert the flux measured by the SPRED to a radiated power, keeping in mind that the obtained value is likely to be an underestimate of the power radiated in the divertor. The same estimate was made for an ELMy H-mode discharge at lower density ($\langle n_e \rangle = 3\times10^{19}$ m^{-3}), with P(NBI) = 15MW (fig.3). This time the Ne injection (7.8×10^{20} atoms) is aimed at maximising the radiation. It results in a saturation of a number of spectral lines on the double SPRED. These line intensities were estimated using line ratios during the non-saturated phases of the signals, giving a factor 2 on the global uncertainty of the power radiated by neon. Only the C III and Ne VII contributions could not be measured because of the saturation of all the corresponding lines. In this case it is clear that however large the error is, the strongest radiator among the neon ions is Ne IV which radiates about 70% of the total neon radiated power, indicating an ionisation equilibrium very different from the L-mode case. Another evidence is the Ne VI modulation as a function of the sweeping, indicating that the Ne VI radiates closer to the target than in the preceding case. Since C III, as in the previous case, is the strongest radiating carbon ion, these results are in qualitative agreement

with the bolometer array measurements showing that the radiation balance is slightly in favour of the X-point radiation (60% of the total radiated power). More experiments are needed to compare these results to the analysis of the bolometer measurements described in [2]. Because of the CIII saturation, it is not possible to say which species, either C or Ne, is the strongest radiator, but from a comparison with the BLOS it can be said that the deuterium radiates about 20% of the total 3.5MW.

EFFECT OF A FORCED D_2 FLOW ON THE NEON RADIATION:

The first pulse shown in the preceding part is one of a series of L-mode, moderate density ($<n_e>$ = 3-4.4 $\times 10^{19}$ m^{-3}), moderate NBI power (3.5MW), X point-swept, divertor D_2-fuelled (2.3-5.5$\times 10^{21}$ atoms/s) discharges. The aim of this series was to study the effect of a forced D_2 flow on the impurity radiation. Ne is puffed as a tracer rather than as a radiator. Both the neon and the deuterium could be injected either from the top of the machine or directly into the divertor, and all combinations were performed. For a given electron density, no effect of the D_2 or Ne injection location was observed regarding the maximum radiation, either on the neon radiation or on the other species (C, O), confirming the results found in [3]. The only difference is the radiation due to the deuterium: it is stronger when the D_2 is injected in the divertor because of the higher deuterium flow necessary to maintain the bulk density.

EFFECT OF INCREASING THE NEON DENSITY IN L-MODE:

A recurrent question about impurity seeding experiments is whether or not it is possible to enhance the edge radiation without contaminating the core. From the series described in the last paragraph, two pairs of shots have been chosen to study the effect of increasing the amount of injected Ne in the plasma at two different densities (fig.4a, $<n_{Ne}>$=0.66$\times 10^{17} m^{-3}$ (solid line), 1.5$\times 10^{17} m^{-3}$ (dashed line); fig.4b, 1.9$\times 10^{17} m^{-3}$ (solid line), 3.3$\times 10^{17} m^{-3}$ (dashed line)). The gain in radiated power when increasing the amount of Ne is considered. However, since the Ne density is different for every shot, we normalise this gain to the Ne density increase in the bulk (estimated from the Z_{eff} measurement):

$$g = \frac{P_{rad2} / P_{rad1}}{n_{Ne2} / n_{Ne1}}$$

g = gain in radiated power / increase in Ne density					
$<n_e>$	Ne III	Ne IV	Ne V	Ne VI	Ne VIII
3×10^{19} m^{-3}	1.6	1.6	1.4	saturated	1.3
4.4×10^{19} m^{-3}	0.8				

At moderate density and for the lower ionisation stages (Ne III to V) the gain in radiated power is significantly higher than the increase of injected neon (see table). For the higher ionisation stages, the gain in radiated power is less favourable, but at least 30% higher than the Ne density increase in the bulk. The difference in the lower and higher ionisation stages indicates a modification of the ionisation equilibrium, even with this small amount of Ne. The decay times of the Ne signals (4.9s for Ne III-V, 4.4s for Ne VI-VIII) significantly decrease when doubling the amount of injected Ne. At higher density, the gain is lower than the increase in the amount of Ne. All the ionisation stages behave in the same way as far as the gain in radiated power is concerned. This is thought to be due to the smaller amount of Ne injected. The decay times (3s for Ne III to V, 3.4s for Ne VI to VIII) do not depend on the amount of injected Ne.

CONCLUSION:

The SPRED has proven to be a useful tool for precise estimates of the radiated flux and even, with few assumptions, the radiated power in the divertor. However, more work is needed to ascertain the C IV resonance line intensity due to its strong dependence upon T_e. The measured Ne VII contribution to the radiation seems fairly small (less than 10% in the L-mode case). Hence if the neon atomic data are revised with more sophisticated calculations, we suggest to put the emphasis on Ne IV which is the strongest radiator of the Ne ions in the pulses presented here. The Ne ionisation equilibrium appears very different in L- and H-mode discharges, more favourable to the edge radiation in H-mode, mainly due to the strong Ne IV radiation. Another Ne-seeding experiment this year will allow us to precise the first results presented here, in particular the relative importance of the various impurities in the radiated power fraction.

In L-mode, for small Ne puffs (compared to the Ne injections aimed at maximising the radiation), the higher density pulses presented here show that the Ne bulk density increases faster than the power radiated at the edge when increasing the amount of injected Ne. At lower density (corresponding here to larger Ne puffs), there is a change in the ionisation equilibrium, suggesting that the T_e and n_e profiles are modified significantly in the divertor region. This is thought to be due to the larger amount of neon in the discharge rather than to an effect of the density.

Simulations with an impurity transport code such as DIVIMP[4] are necessary to confirm the assertions made in this paper, in particular in providing a consistent overview of the T_e, n_e profiles and of the Ne ionisation equilibrium.

REFERENCES

[1] H.P. Summers, ADAS, JET-IR(94) 06 (1994)

[2] H.J. Jäckel et al., 37th APS Conference on Plasma Physics, Louisville, USA (1995)

[3] P.J. Harbour et al., 22d EPS Conference on Controlled Fusion, Bournemouth, UK (1995)

[4] P.C. Stangeby and J.D. Elder, J. Nucl. Mater. 196-198 (1992) 258.

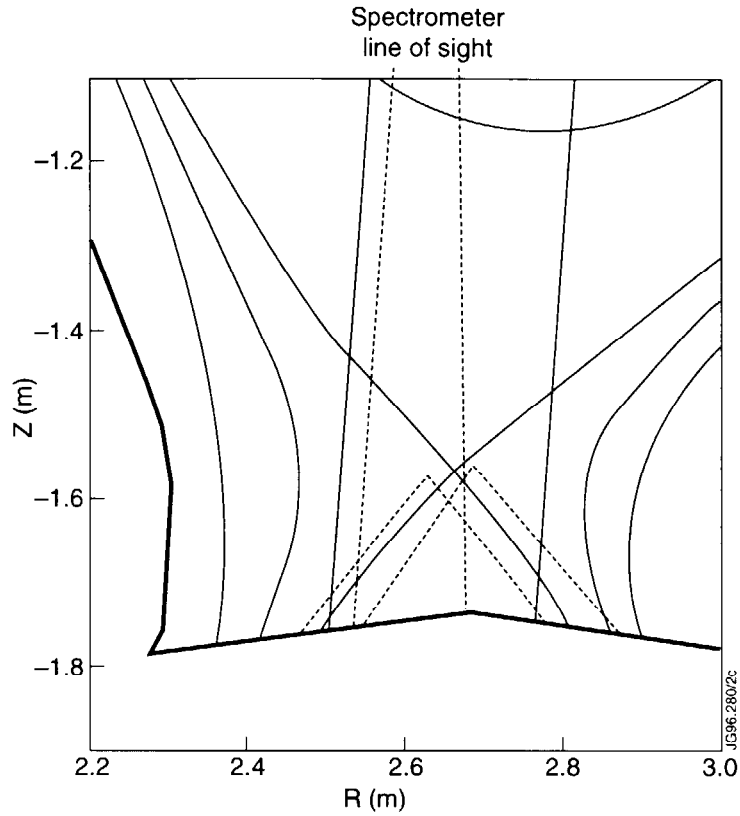

Fig.1: SPRED line of sight and BLOS in the divertor region. The extreme X point positions are indicated for #35042.

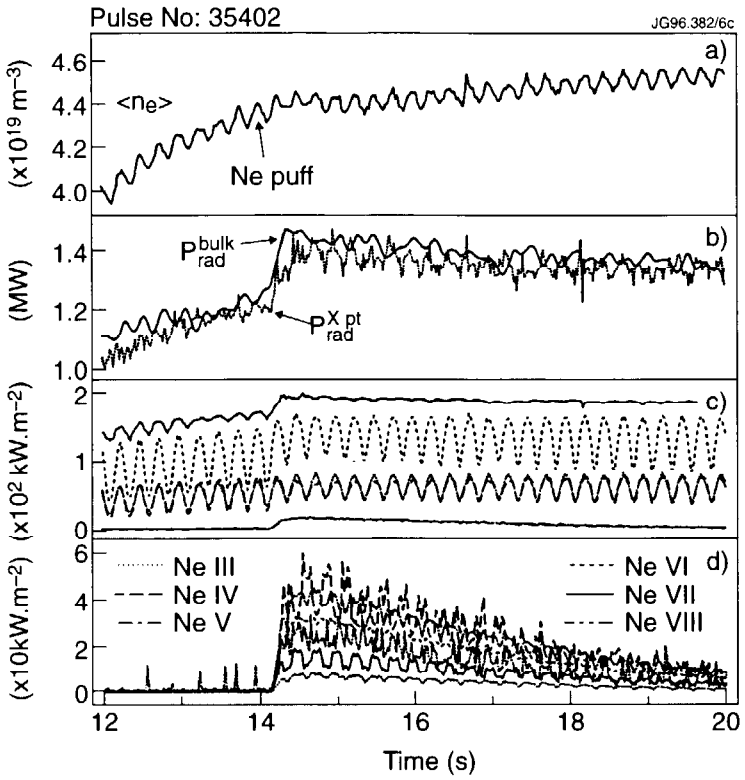

Fig.2: #35402: a) volume average density; b) radiated power measured by the bolometer array; c) radiated flux measured by the BLOS (solid) and the SPRED (dashed: total, dotted: D, broad-dashed: C, dashed-dotted: Ne); d) Flux radiated by Ne as measured by the SPRED.

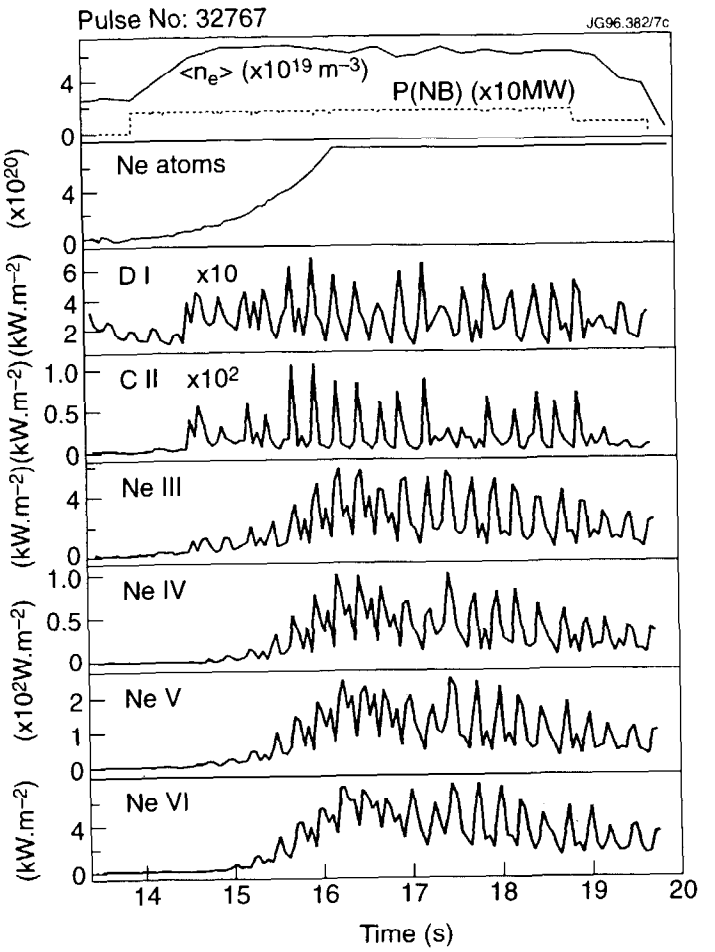

Fig.3: #32767: volume average density, neutral beam injection power, Ne atoms injected into the vessel and radiated flux measured by the SPRED.

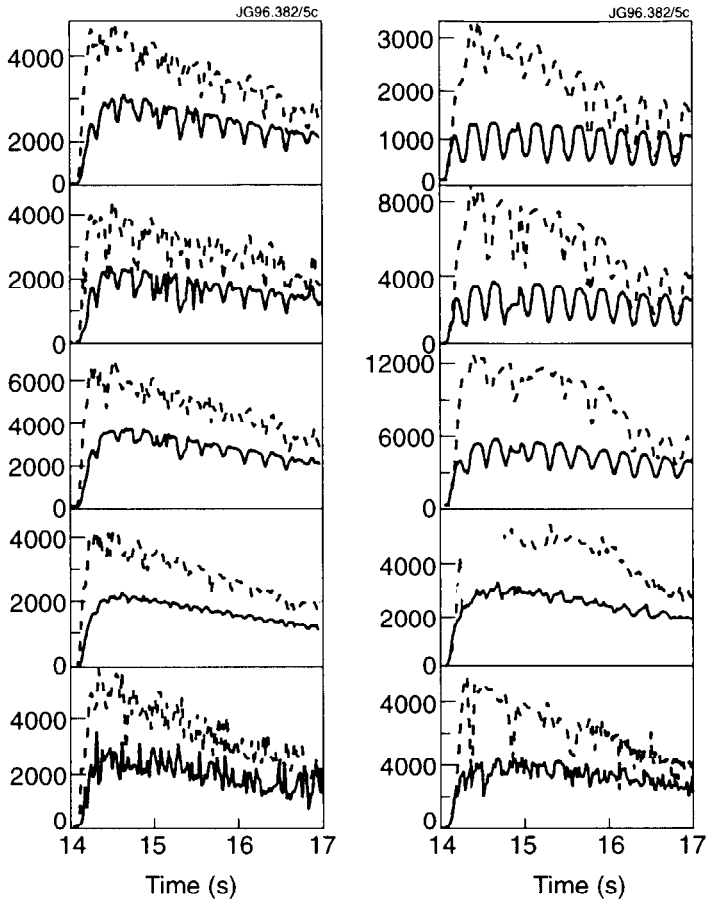

Fig.4: Neon radiated flux at $<n_e>=4.4\times10^{19}m^{-3}$ (left) and $3\times10^{19}m^{-3}$ (right). From top to bottom: Ne III, IV, V, VI and VIII.

Monitoring of Detachment and the Edge using XUV Impurity Spectra from the Mark I Divertor Phase of JET

M G O'Mullane[1], I H Coffey[2], R Giannella

JET Joint Undertaking, Abingdon, Oxon., OX14 3EA, UK
[1]University College Cork, Ireland,
[2]The Queen's University of Belfast, Northern Ireland

INTRODUCTION

The XUV spectrum of CV and CVI from the edge plasma in JET is rich in diagnostic potential. Impurities in the spectral range 20-40Å are monitored with an XUV grazing incidence spectrometer. It is possible to move the spectrometer so that it can view the inner wall at any angle. The spectra analysed here were taken with the spectrometer angled at it lowest position (see insert in Figure 3). Here the spectrometer views the SOL during the ramp-up phase of the discharge, typically for the first 5 seconds. When the X-point is formed the confined plasma is seen. During radiative divertor experiments the view is just above the radiating zone. If the plasma is going to detach from the strike plates it is reflected in the spectra, which can serve as an early indicator of detachment.

SOL PARAMETERS IN RAMP-UP PHASE

In the ramp-up phase of the plasma the spectrometer views the SOL exclusively. An unusual Lyman series and CV G-ratio (intercombination / resonance line ratio) are seen in *all* discharges (Figure 1). A 'distortion' in the Lyman series appears with the Lyman γ line prominent. There is also an inversion in the He-like system G ratio. In Figure 1 the top trace shows the pre-divertor JET limiter configuration spectra (# 13571). For the JET Mark I divertor configuration the middle trace shows a typical edge spectrum in the ramp-up phase (# 32595) and the lower trace shows a radial view through the main plasma (# 30763) in the X-point phase. The difference between the pre-divertor and Mark I divertor spectra is that no n>6 C VI Lyman series lines are now observed. These lines have been attributed to charge exchange with excited deuterium produced when there is contact between the limiter and the plasma [1]. Hence the neutral deuterium is formed by Frank-Condon dissociation at ~3eV

The emission seen by the spectrometer is a slice through a 3-D volume whose parameters vary in space and time (the fall-off lengths are ~cm). The model reduces the geometry to 0-D to

elucidate the important atomic processes. The extreme values of the CV G-ratio can only be explained by emission from a strongly recombining plasma. A transient, recombining, model of the emission is used. Outfluxing C^{6+}, C^{5+} and C^{4+}, from the confined plasma, enters the SOL where ionisation equilibrium does not apply. The outfluxing carbon recombines with a competition between charge exchange and radiative recombination. The residence time of carbon in SOL is set by parallel transport, where $\tau = 2L_c/c_s$ (L_c = connection length, c_s = sound speed). The outfluxing mix is adjusted to match the Ly α /CV resonance line ratio, which is a measure of the ionisation balance. The system is allowed to evolve with the integration time set to 50ms to match the spectrometer's time resolution.

The emissivities of the driving processes (excitation, recombination and charge exchange) were calculated in a collisional-radiative code which forms part of ADAS [2] at JET. All possible transitions and excitation routes for $n \leq 5$ for CVI and $n \leq 4$ for CV were included. The atomic data is mostly taken from ADAS. The charge exchange cross sections are from [3,4]. These were extended by hand to lower energies. It must be noted that there is a severe lack of cross section data at such low thermal energies.

The residence time is estimated at ~4ms. It can be modified by effects such as thermal force in the SOL, but the calculated ratios are relatively insensitive to this parameter. The prominence of the Lyman γ line is conclusive evidence of charge exchange contributions. Figure 2 shows a comparison between calculated line ratios and observations. The model requires a n_{D0}/n_e ratio of ~0.05, equivalent to a neutral density of $\sim 5 \times 10^{16} m^{-3}$. Neutral density fractions of 10^{-3} and above are necessary to explain the CV G ratio. Radiative and dielectronic recombination alone are not enough to account for the observations. The SOL temperature is estimated to fall in the range 50–90eV, which is consistent with all the calculated ratios.

DETACHMENT SIGNATURE

The line-of-sight of the spectrometer passes just above the divertor radiation zone. The emission line ratio of the CV resonance line to the CVI Lyman α line is an early indicator of detachment (Figure 3). As the plasma approaches detachment this ratio rises. The CV G-ratio remains relatively constant as the plasma detaches. When the plasma is fully detached the region of cold plasma becomes localised at the X-point.

During the radiative divertor phase no CVI charge exchange lines are seen, indicating that the emission is from within the confined plasma. Hence a diffusive-ionisation balance equilibrium model can be used (the neutral fraction is much lower in the confined plasma than in the SOL). The observed carbon G-ratio is ~0.7 compared with the equilibrium value of 0.45. The calculated G-

ratio (figure 4) shows that in radiative divertor plasmas the plasma surrounding the X-point radiating zone is cooling as a result of the condensation in the divertor. The local temperature outside the X-point radiating zone, but from the confined plasma, cools to ~80–90eV from the 'normal' temperature of 300eV. G- ratio measurements further from the X-point show higher temperatures. This temperature gradient along the outer flux surfaces may be destabilising, possibly leading to radiative collapse of the plasma.

When a radiative divertor plasma detaches, the CV resonance to Lyman α line ratio begins a steady increase approximately 3.5s beforehand. Radiative divertor discharges which do not attain detachment do not exhibit this behaviour. Figure 4 shows this ratio calculated as a function of confinement time. The steady, monotonic, change in the line ratio as the plasma moves towards detachment is a measure of an increasing diffusion (because $\tau_p \propto a^2/D_\perp$) in the near-edge plasma. The poorer edge confinement may be caused by a degradation of the confinement mode.

CONCLUSION

It has been shown that the CV and CVI spectra can be used as diagnostics of the outer plasma region. In the SOL charge exchange with neutral deuterium is significant and amounts to ~0.05% of n_e. The temperature of the SOL is ~50-90eV. There is a lack of charge exchange cross section data at the low energies needed for this analysis. The near-edge XUV spectra provide a reproducible detachment signature. The condensation at the X-point sets up a temperature gradient along the flux surface. The ionisation balance is also affected. Enhanced diffusion or poorer edge confinement is evident well before the plasma fully detaches.

REFERENCES

[1] M Mattioli et al., Phys. Rev. A, 40, p3886 (1989)

[2] H P Summers, Atomic Data and Analysis Structure (ADAS), JET IR(94)06

[3] N Shikamura et al., Phys. Rev. A, 45, p7876 (1992)

[4] M Kimura and C D Lin, Phys. Rev. A, 32, p1357 (1985)

ACKNOWLEDGEMENT

This work was partially funded by the UK Department of Trade and Industry and EURATOM.

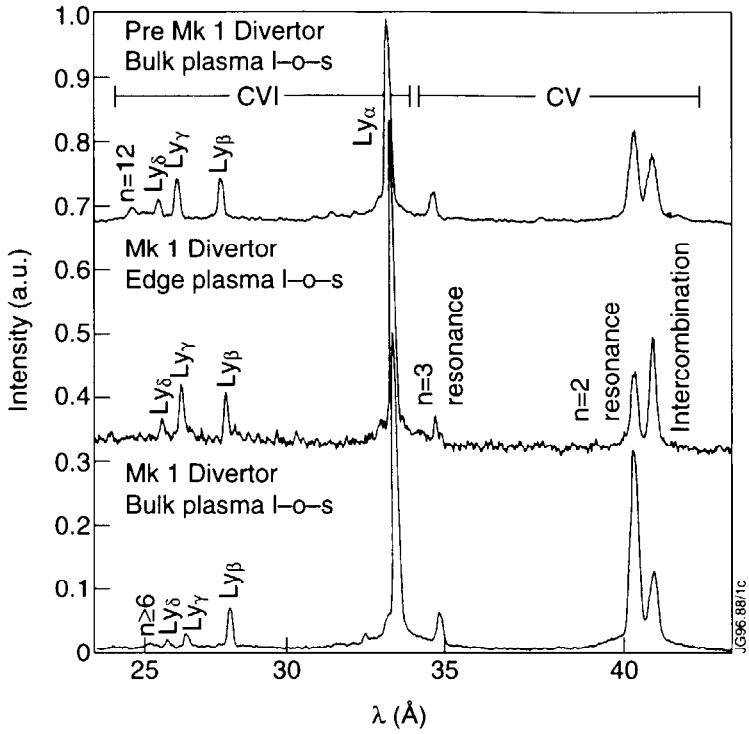

Figure 1 Comparison of observed C V and C VI spectra from the main and edge plasmas from different JET operational periods.

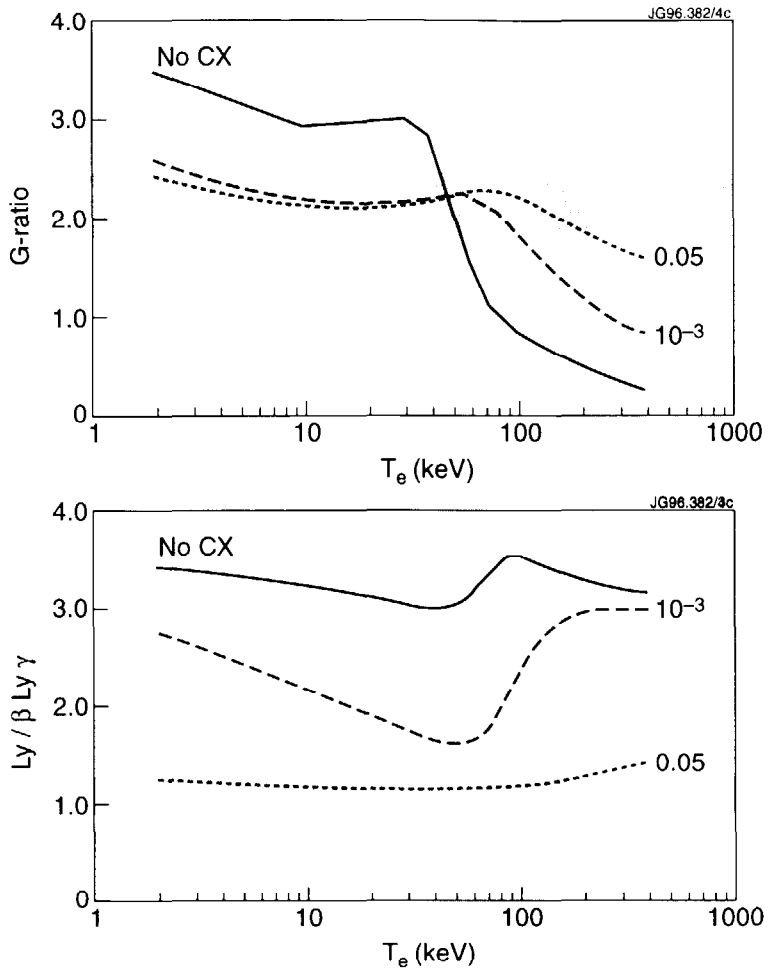

Figure 2 Comparison between observed and modelled line ratios. The spread of the observed ratio is indicated by a shaded region.

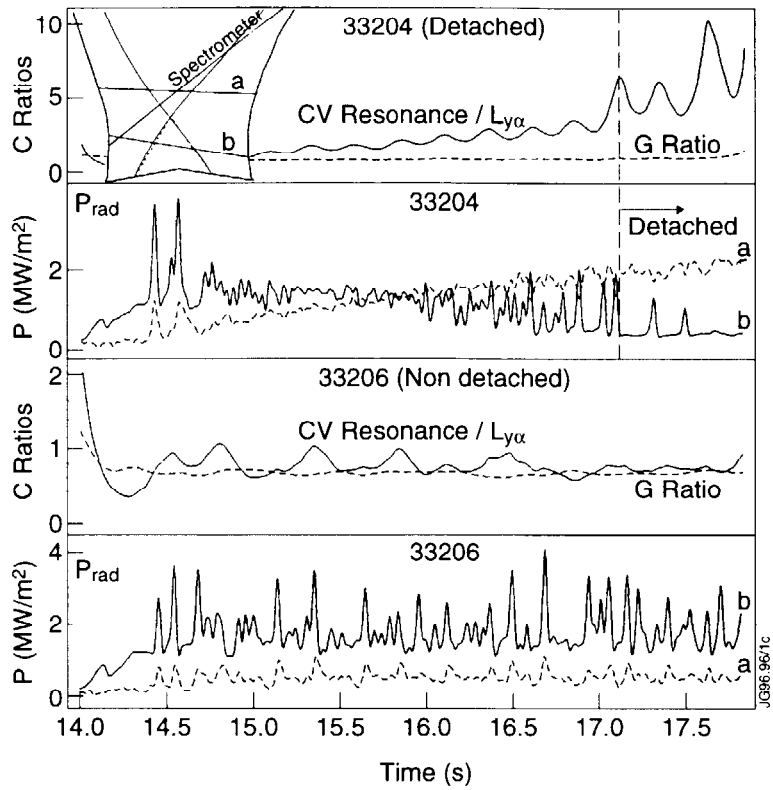

Figure 3 The spectroscopic detachment signature. The modulation of the ratios is due to divertor sweeping. Top shows a detached case with the non-detached on the bottom. Note that the G-ratios have similar values. a and b refer divertor bolometer LOS.

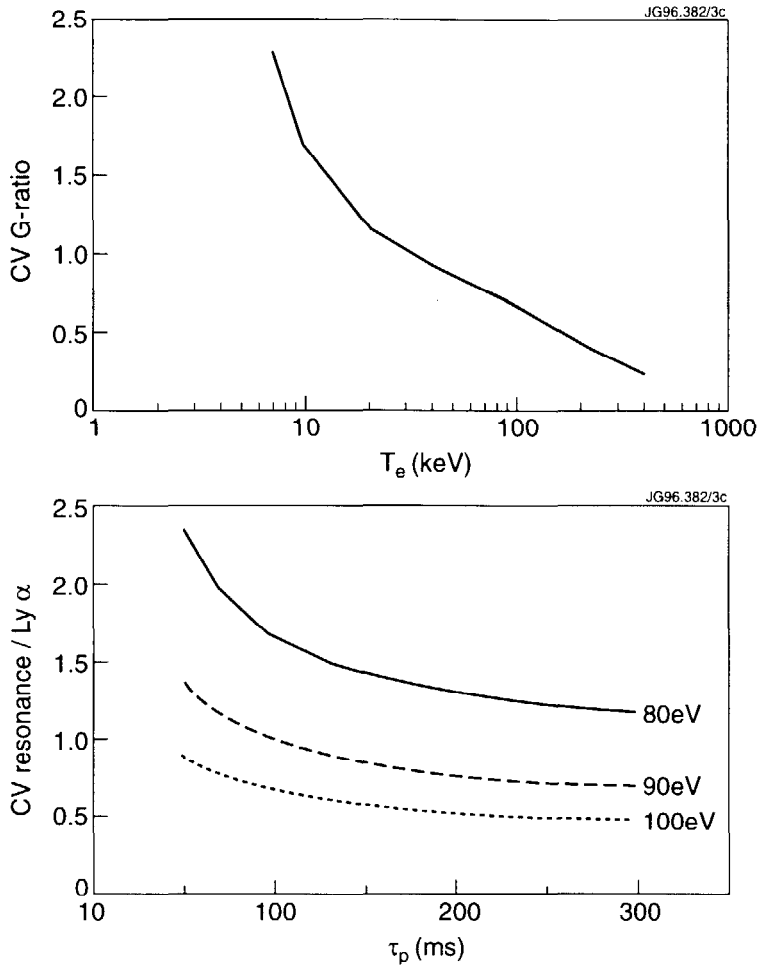

Figure 4 Top: Carbon G ratio in diffusive-ionisation balance equilibrium. The shaded region is the observed ratio. Bottom: C V resonance to C VI Lyman α emission line ratio as a function of confinement time.

Variation of Impurity Transport during ELMy H-modes in JET Plasmas

M G O'Mullane[1], H Chen[2], C Flewin[3], N C Hawkes[4], M von Hellermann,
L Lauro-Taroni, N J Peacock[4]

JET Joint Undertaking, Abingdon, Oxon., OX14 3EA, UK
[1]University College Cork, Ireland,
[2]Imperial College, London, UK,
[3]University College, London, UK,
[4]UKAEA Fusion, Culham, Abingdon, Oxon., UK (EURATOM-UKAEA Fusion Association)

INTRODUCTION

H-mode confinement is breached by Edge Localised Modes (ELMs) expelling particles and energy. One of the features of radiative divertor experiments is the appearance of giant ELMs followed by a series of smaller, grassy, ELMs. These 'compound' ELMs are then followed by a period of quiescent H-mode. The effect on impurity profiles of compound ELMs can be interpreted in terms of a time varying transport model. The effect of the ELMs is seen in the Ne^{10+} distribution inside the transport barrier [1]. During the H-phase an increase of the more highly stripped ions (e.g. Ne^{10+}), inside the transport barrier is accompanied by depletion of lower charge states (e.g. Ne^{5+}) outside the barrier and in the scrape-off layer. The build-up of ion pressure at the transport barrier during this phase is eventually terminated by the ELM. The JET charge exchange diagnostic of edge impurities has been absolutely calibrated. Its space resolution of ~1cm over the 10cm edge region is used to examine changes in the edge impurity profiles in detail. The time behaviour of the transport during ELMy H-mode and its variation as the ELM frequency increases are examined.

CHARGE EXCHANGE MEASUREMENTS OF IMPURITY DENSITY AT THE PLASMA EDGE

The JET edge charge exchange diagnostic (ECX) consists of two sets of opposing viewing chords positioned above and below the magnetic axis intersecting the neutral beams. The time resolution of the instrument is determined by photon statistics; with the large impurity densities of neon used in these experiments (~1.5% of n_e) the uncertainties are relatively low and the time resolution is 20ms or better. Interpretation of the measured intensities involves detailed consideration of the geometry and the neutral beam deposition characteristics.

The H-mode model is characterised by a narrow region of inward convection at the plasma edge – the transport barrier. The location of the barrier is determined by the change in slope of the ion density or ion pressure profiles. The T_i profile does not respond to the ELMs but the density gradient alters significantly [2]. The location of the barrier for an ELMy H-mode discharge is not affected by giant ELMs. In general it remains located at ~7cm inboard of the last closed flux surface (LCFS), as calculated by the equilibrium reconstruction code.

Charge exchange measurements from the main plasma have shown that the light ($2<Z\leq10$) impurities do not accumulate on-axis in H-mode but are peaked at r/a~0.75-0.82 [3], with carbon and neon peaking at the same radius. The ECX measurements confirm the steep gradients at the outer part of the bulk measurements. The off-axis accumulation may be due to a centrifugal contribution to the convective transport as a result of the plasma rotation which is driven by the neutral beam torque. Phenomenologically this requires an outward convection in the model.

TIME DEPENDENT TRANSPORT MODELLING

The SANCO 1.5-D impurity transport code has been used in all simulations. Particle transport is described by diffusive and convective terms with the flux of each ionisation stage given by coefficients which are a function of flux surface (Ψ) and time,

$$\Gamma_z = -D(\Psi,t)\nabla n_z + V(\Psi,t)n_z .$$

The transport functions (D,V) are changed until the transport is consistent with experiment. A limitation of the code is that it is not a closed description of the impurity evolution. The source function of the influx is based on a peripheral ion stage. SANCO uses experimentally measured T_e and n_e profiles. To follow the temperature evolution, fast ECE radiometric measurements of the electron temperature profile, with spatial resolution $\geq$1cm, at the edge, and temporal resolution $\geq$1ms, are employed. The density profiles are from LIDAR measurements.

The behaviour of intrinsic carbon shows the time evolution of the change in impurity profiles following the L-H transition and the build-up of impurities in quiescent H-mode. The transition is simulated by an abrupt change in transport at a time determined by the drop in $D\alpha$. The width and depth of the barrier were adjusted until there was agreement between the simulated and experimental C^{6+} ion densities (Figure 1). The simulations were constrained to match the absolute CIII emission. The experimental observations of a steady ramp-up of C^{6+} inside the transport barrier and a near constancy outside arise naturally from the simulations.

In ELM-free H-mode there are no gross disparities, in the time evolution of impurity emission, between the main vessel and the divertor. In ELMy H-mode the source of intrinsic impurities, such as carbon, becomes localised and the SANCO model of a symmetrical influx is

no longer strictly applicable. In a radiative divertor discharge the gas puffing provides a steady source of impurities. The source term is based on the NeVII ($2s^2$ – 2s2p 465.22Å) line since NeVII radiates entirely in the SOL.

Compound ELMs are very suited to studying variations in the transport as they are well spaced. Figure 2 shows the time evolution of Ne^{10+} for a number of chords either side of the transport barrier (at R=3.68m, LCFS at 3.75m). The simulated radial profiles match the experimental profiles across the barrier. In the model the transport is switched from H-mode at the onset of the ELM and remains so for the duration of the grassy ELMs. The transport coefficients used are shown in Figure 3. The simulations show that the convective transport barrier (~1-2cm wide) remains in place during ELMs and the degradation in confinement is from enhanced diffusion only. The increased diffusion is localised to a ~5cm zone inside the LCFS and extending into the SOL. The model predicts a threshold diffusion and a sensitivity to the height of the convective barrier. A diffusion greater than 1.0 m^2s^{-1} at the edge is sufficient to simulate the Ne^{10+} profiles. The barrier sets a minimum velocity for outfluxing impurities with $V(r=a) \sim 15 \pm 2$ m s^{-1}.

TIME INDEPENDENT TRANSPORT MODELLING

With increasing ELM frequency the recovery of the H-mode phase is rapid and an average, or time independent, transport applies. The time variations in transport are smeared out for grassy ELMs and an average transport during the H-mode applies. A long impurity confinement time is one of the characteristics of H-mode. A series of laser ablation experiments were undertaken to measure the Z-dependence of particle confinement time in ELMy H-modes and in Ohmic plasmas. Figure 4 shows the decay times. There is a slight (~20%) increase in confinement in ELMy H-mode compared to ohmic discharges but this is significantly shorter than ELM-free H-mode where up to 4s has been observed. The confinement was found to be independent of Z.

CONCLUSIONS

A model of impurity transport during H-mode shows that the losses caused by compound ELMs are diffusive, suggesting a stochastic model of the ELM. The enhanced diffusion zone extends ~5cm inside the LCFS. Giant ELMs do not breach the convective barrier. Absolutely calibrated measurements of the impurity profiles at the edge have been simulated. The position of the transport barrier does not vary in time. With increasing ELM frequency the confinement degrades although the transport barrier remains. In general during discharges with grassy ELMs an average, time independent, transport is successful in modelling the spectroscopic observations. There is a modest increase in impurity confinement time for this type of H-mode over Ohmic plasmas.

REFERENCES

[1] M G O'Mullane et al., 22nd EPS Conference, III-121 (1995)

[2] N C Hawkes et al., 22nd EPS Conference, III-261 (1995)

[3] M von Hellermann et al., 22nd EPS Conference, II-9 (1995)

ACKNOWLEDGEMENT

This work was partially funded by the UK Department of Trade and Industry and EURATOM.

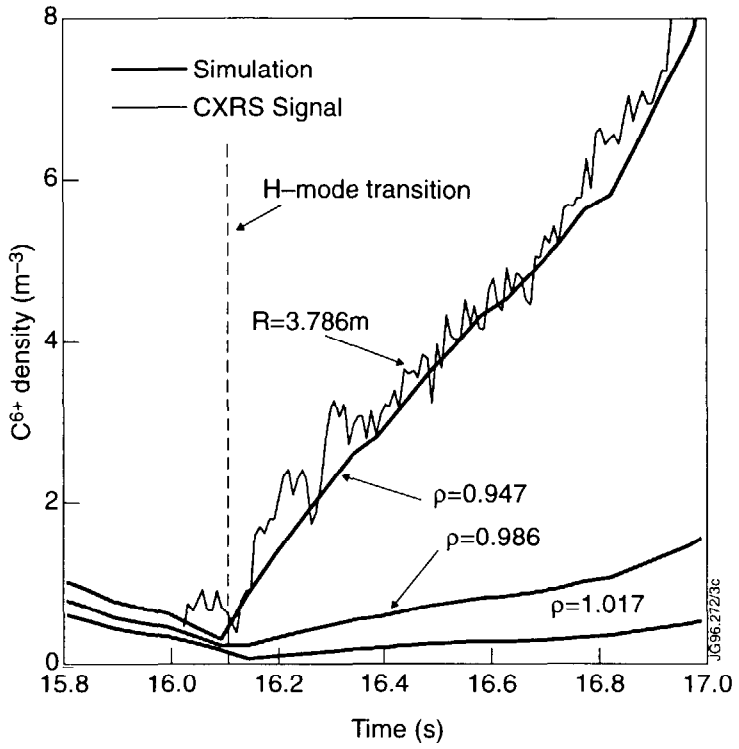

Figure 1 Time dependent transport simulation of fully stripped C^{6+} during the L-H transition. The near constancy of impurities in the SOL and the steady ramp-up inside the barrier are consequences of the switch in transport.

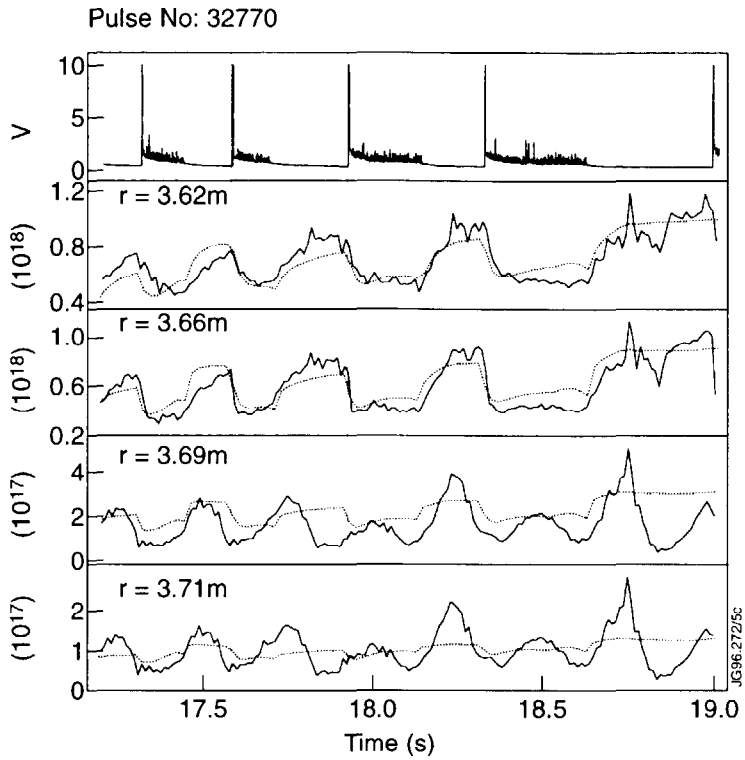

Figure 2 Time evolution of Ne^{10+} inside and outside the transport barrier. The difference between the simulations and measurements in the extreme outer chords arises from the plasma being swept across the divertor which introduces a periodic variation in the SOL position.

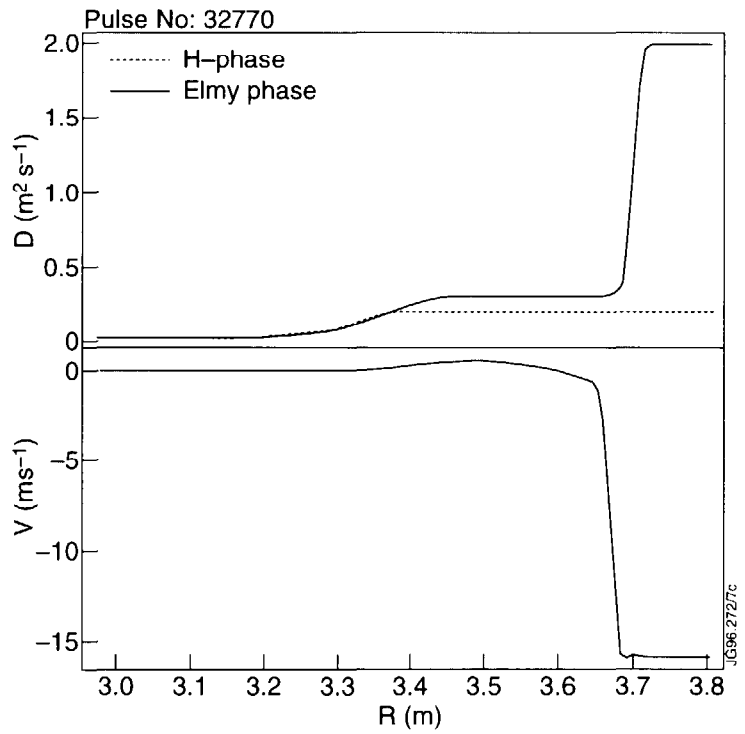

Figure 3 Transport profiles used in the simulation of Ne^{10+} ion profiles during ELMy H-mode. The barrier is at R=3.68m and the LCFS is at R=3.75m.

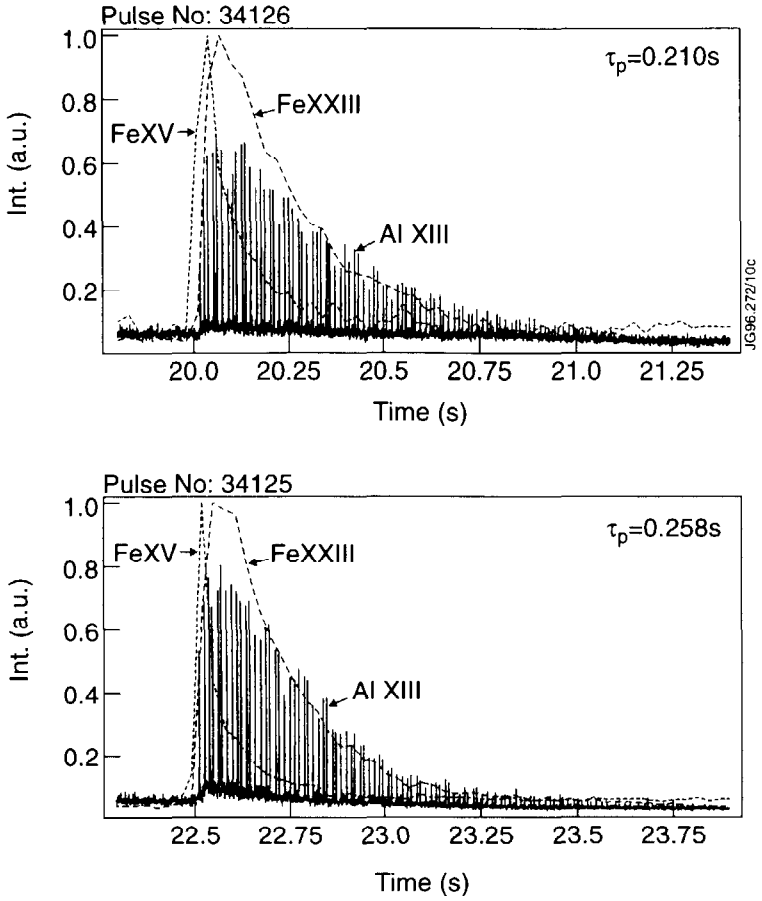

Figure 4 FeXXIII and AlXIII during ohmic (top) and ELMy H-mode (bottom). The aluminium is monitored with a scanning crystal spectrometer and the iron by a normal incidence VUV spectrometer.

Numerical analysis of the heat pulses in JET

V.V.Parail, A. Cherubini, M. Erba, P. Galli*, R. Giannella, L. Porte, A. Rookes, F. Romanelli#, E. Springmann, A. Taroni

JET Joint Undertaking, Abingdon, Oxon OX14 3EA, UK
*Dipartimento di Fisica,Universita Degli Studi di Milano, I-20133, Milano, Italy.
Associazione EURATOM-ENEA sulla Fusione, C.R.E. Frascati, C.P. 65, 00044, Frascati, Roma, Italy

INTRODUCTION.

Predictive modelling of different kind of heat pulses is a powerful tool to test the validity of transport models. The last experimental campaign in JET gave high quality information of the electron temperature evolution during five types of heat pulses: the L-H transition, sawtooth crashes, giant ELMs, cold pulses triggered by laser impurity ablation and slow roll-over. All relatively strong pulses triggered from the plasma edge show a fast global modification of at least the electron heat conductivity which, in principle, permits different interpretations. A first one involves the idea of a critical temperature gradient (or strong profile consistency) [1-3], an other one uses the idea of a global turbulent structures produced by a toroidal or a non-linear coupling of the unstable modes [4-6]. Numerical analysis of above mentioned heat pulses will be presented to assess which of these models is appropriate.

EXPERIMENTAL OBSERVATIONS.

The 94/95 experimental campaign on JET gave examples of heat and cold pulses which were often initiated in the same shot. Figure 1 shows, for example, the evolution of the electron temperature during a cold pulse and subsequent sawtooth crashes for the H-mode shot #31341. The asymmetry in the speed of pulses which propagate inward and outward is clearly seen - the sawtooth crash heat pulse propagates outward in the usual diffusive way, while the cold pulse changes the behaviour of the electron temperature almost instantaneously in the whole outer half of the plasma column. The evolution of electron temperature during giant (type I) ELMs on JET, after a very short MHD phase, was shown to be very similar to that of the cold pulses [7]. Figure 2 shows temporal evolution of the main plasma parameters during the so called slow roll-over, the event which often terminates high performance phase of the hot ion H-mode on JET. All these transient phenomena were analysed in a semi-predictive way with the transport code JETTO, using either a "global" or a critical temperature gradient model of anomalous transport.

TRANSPORT MODELS.

In our analysis we used a modified version of the RLW [2] critical temperature gradient model with:

$$\chi_{e,i}^{anom} = \alpha_{e,i}\chi_{RL}(\nabla T_e - \beta\nabla T_{crit})\theta(\nabla T_e - \beta\nabla T_{crit}) \quad (1)$$

as an example of a critical marginality model. Here T_{crit} defined by $T'_c = \left(\frac{6}{q}\frac{hjB3}{nT1/2}\right)1/2$, $\chi_{RL} = 2(1-\sqrt{\frac{r}{R}}\sqrt{1+Z_{ef}}\sqrt{\frac{T_e}{T_i}}\left[\frac{\nabla T_e}{T_e}+2\frac{\nabla n_e}{n_e}\right]\frac{q^2}{\nabla qB_T\sqrt{R}}$ and numerical coefficients $\alpha_{e,i}$ and β were varied in order to test a different degree of profile consistency. The original RLW model has soft profile consistency with $\alpha_{e,i} = \beta = 1$. Analysis shows however that we should increase $\alpha_{e,i}$ up to ten times in order to be able to get fast propagation of the cold pulses (which corresponds to a strong profile consistency transport model). Simultaneously we should increase coefficient β to reproduce experimental temperature profile.

Our "global" model is based on the assumption that due to either toroidal or non-linear coupling plasma turbulence organises long correlated structures (with the radial correlation length being proportional to the plasma minor radius). In this case the magnitude of the transport coefficients depends not only on the local plasma parameters but also on the source of the turbulence near plasma edge (we will assume that plasma turbulence emerges near the separatrix due to either temperature or pressure gradients and propagates inside with the group velocity of the unstable waves). In order to reproduce such a behaviour, in further analysis we will assume that both electron and ion thermal diffusivities consist of a local gyrobohm term (which could be produced by the ITG instability, for example) and a global bohm-type term (produced by either ballooning or interchange instability near the separatrix) which depends on the relative electron temperature or pressure gradient near the separatrix [7]:

$$\chi_{e,i} = \alpha_{e,i}^{GB}\rho_i\left|\frac{\nabla T_e}{B_T}\right| + \alpha_{e,i}^{B}\left|\frac{\nabla nT_e}{nB_T}\right|a^2q^2\left|\frac{\nabla T_e(r\approx a)}{T_e(r\approx a)}\right| + \chi_{e,i}^{ncl} \quad (2)$$

where $\alpha_{e,i}^{GB}$, $\alpha_{e,i}^{B}$ are numerical coefficients. In a sense the global model is similar to the critical marginality one because the global confinement in both models depends on the plasma quantities near the separatrix. The main difference between the models is that transport properties of the global model are not symmetrical but depend on whether the transient phenomena are initiated near the edge or near the centre of the plasma column. Indeed, if we assume for simplicity that only the electron temperature is perturbed in the course of the heat pulse and that this perturbation is small $\delta T_e/T_e << 1$ we obtain the following equation for the evolution of δT_e:

$$\frac{\partial \delta T_e}{\partial t} \approx div\left\{ \chi_e^{(0)} \frac{\partial \delta T_e}{\partial r} + \frac{\partial \chi_e^{(0)}}{\partial \nabla T_e} \nabla T_e \frac{\partial \delta T_e}{\partial r} + \frac{\partial \chi_e}{\partial T_e(r \approx a)} \nabla T_e \delta T_e(r \approx a) \right\} \quad (3)$$

The first two terms in the right hand side of equation (3) describe the usual diffusive propagation of the heat pulse independently of the localisation of the pulse origin. The last term emerges from the global model and only if the heat pulse is initiated near the plasma edge. It works as a perturbation of the heat source and is distributed over the whole plasma volume. As was discussed earlier, the characteristic time of propagation of such a heat source inward is controlled by the group velocity of the turbulence and it is much faster than the typical transport time $\tau \approx a^2/\chi$.

RESULT OF NUMERICAL ANALYSIS.

We have performed a predictive numerical modelling of selected JET discharges with different kind of the pulses. The selection covers both the heat pulses, initiated near the plasma centre (caused by the sawtooth crash) and pulses initiated near the plasma edge (cold pulse, ELMs, L-H transition and slow roll-over).

Figure 3 compares the result of the numerical simulation of the cold pulse and sawtooth heat pulse with the corresponding experimental evolution from shot #31341. Direct comparison of the change in slope of the simulated electron temperature at different radii at the onset of the pulses shows, that the global model (2) can reproduce the observed asymmetry. The critical marginality model with soft profile consistency underestimates the speed of propagation of the cold pulse while the model with strong profile consistency overestimates the speed of the sawtooth heat pulse.However simulation of slow roll-overs seem to indicate that a combination of the global transport and ITG mode might be at work. The result of the numerical analysis of the central ion temperature evolution during the roll-over with different transport models is shown in Figure 4.

CONCLUSIONS.

In summary, even though the critical marginality models considered here can reproduce some of the features of the global and local transport, they seem to fail to reconstruct the asymmetry in the time scales observed during transient phenomena. A "global" model gives a better agreement with experimental results in these situations. However modelling of the slow roll-over indicates that a combination of the global turbulence, which dominates in the outer part of the plasma volume, and of the local ITG mode, which could be important at mid-radius, might be responsible of the variety of phenomena observed.

REFERENCES.

[1] F. Romanelli, W.M. Tang and R.B. White, Nucl. Fusion 26, (1986), 1515;

[2] P.H. Rebut, P. Lallia, M. Watkins in Plasma Physics and Controlled Nuclear Fusion Research 1988 (Proc. 12th Int. Conf. Nice 1988), Vol. 2, IAEA, Vienna (1991) 191;

[3] W. Dorland et al., 15th Int. Conf. on Plasma Phys. and Contr. Nucl. Fus. Res., Seville, Spain 1994, CN-60/D-P-I-6;

[4] J.W. Connor, R.J. Hastie, J.B. Taylor, Proc. Roy. Soc. London Ser. A 365, 1(1979)

[5] F. Romanelli, F. Zonca, Phys. Fluids, B 5, (1993), 4081;

[6] J.G. Cordey et al., Plasma Phys. and Contr. Fusion, 36, suppl..(7A),(1994), A267;

[7] V. Parail et al., JET-P(95)49, to be published in Plasma Phys. and Contr. Fusion, 1996

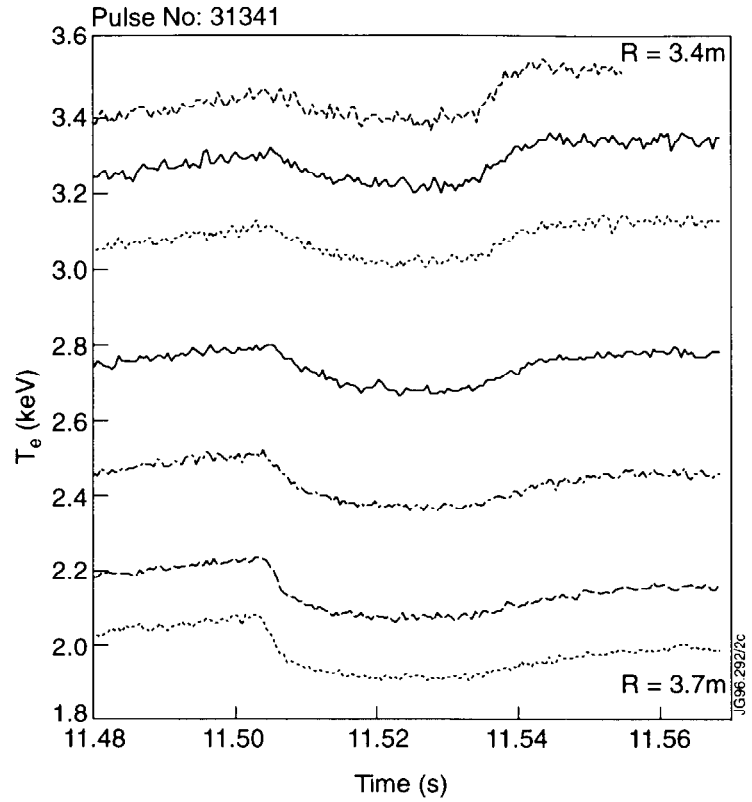

Figure 1. Experimental electron temperature evolution on different radii for the cold pulse followed by sawteeth heat pulses.

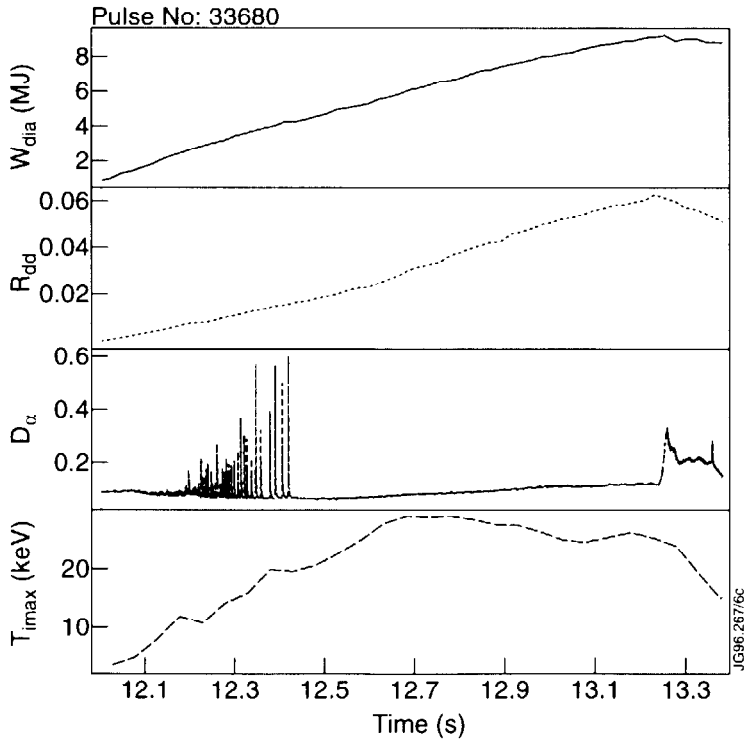

Figure 2. Evolution of the main plasma parameters in the hot ion H-mode which is terminated by the slow roll-over.

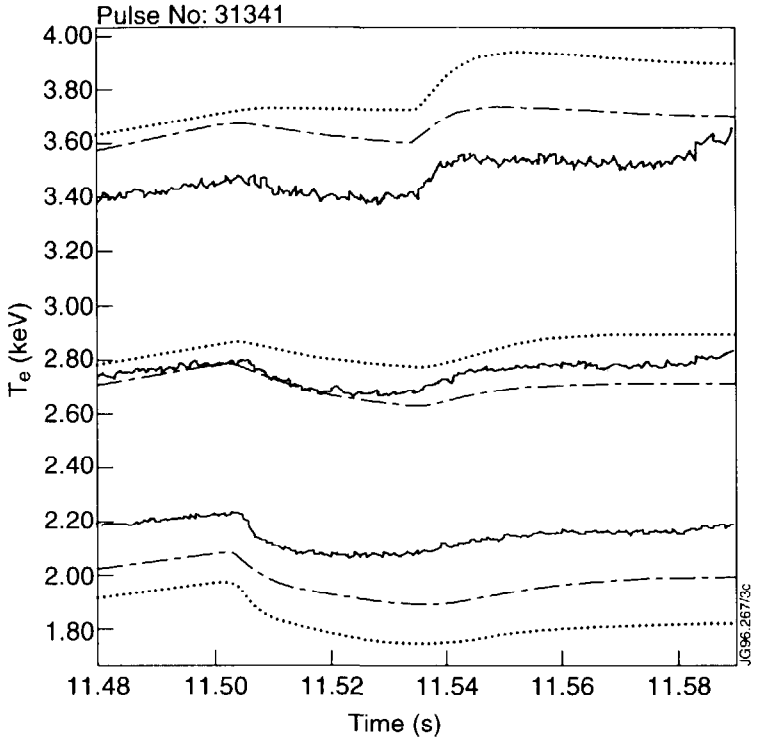

Figure 3. Comparison of the experimental electron temperature evolution (solid lines) with the simulated one: global model- chain, soft profile consistensy - dotted.

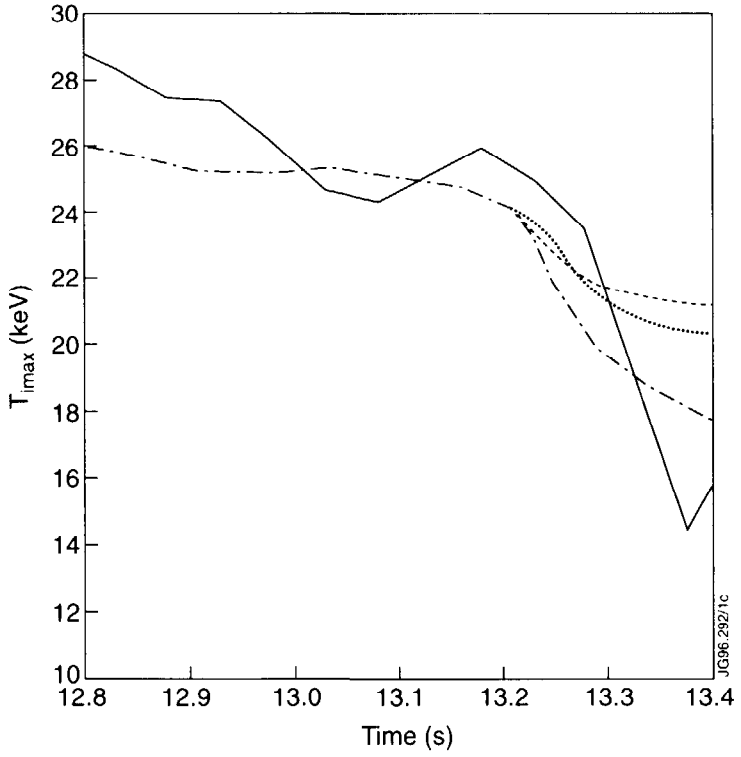

Figure 4. Temporal evolution of the central ion temperature during roll-over: solid- experiment, dashed - global model, dotted- ITG model, chain - combination of global and ITG models.

First Measurements of Gas Balance and Chemical Composition in the Mk I Pumped Divertor Phase of JET using the Gas Collection System

A Rossi, G Saibene, P Kupschus

JET Joint Undertaking, Abingdon, Oxfordshire, OX14 3EA, UK

1. INTRODUCTION

Gas recovery measurements in Tokamaks give direct information both on the short and long term hydrogenic in-vessel wall retention; in particular, the determination of the deuterium vessel inventory is essential to extrapolate to D-T operations, as required for the forthcoming JET D-T campaign and for ITER. The measurement of the chemical species present in the gas released from the Tokamak wall provides data for the gas exhaust collection and reprocessing plant.

The new JET Gas Collection System (GCS) measures the time evolution, absolute amount and chemical composition of the gas released from the JET vacuum vessel in the following modes of operation:

1. Natural thermal wall outgassing, 2. After plasma pulses, 3. During divertor cryopump regeneration, and 4. During glow discharge cleaning.

This paper presents GCS measurements carried out during the 1994/95 JET campaign, and illustrates the effects of the introduction of the JET MARK I pumped divertor on the hydrogenic inventory of the machine.

2. THE NEW GAS COLLECTION SYSTEM FOR JET

The GCS measures the amount of gas (H, D, He and volatile impurities produced into the torus such as hydrocarbons of various stoicheiometry) released from the torus, in all conditions of operation of JET. Moreover, the GCS can analyse the composition of the gas released from the torus and allows on-line sampling for off-line chemical analysis.

During the 1994/95 JET campaign, gas recovery measurements and on line gas analysis were carried out. The short term gas recovery was measured and, at the same time, the gas composition was analysed with a high resolution quadrupole mass spectrometer.

3. EXPERIMENTAL RESULTS (MK I CAMPAIGN 1994/95)

3.1. Gas balance measurements and wall retention measurements

Measurements of the short term gas recovery were carried out during the 1994-95 Mark I Experimental Campaign (graphite and Inconel wall, with Be evaporated coating), both with carbon (CFC) and beryllium divertor tiles.

Figure 2 shows the percentage of gas recovered after non disruptive plasma pulses, when the divertor cryopump is not cooled down. The data are compared to previous JET results [1,2] obtained with a first version of JET Gas Collection System. For the Mk I campaign, the average deuterium recovery varies from 30 to 60% of the input, depending on the total gas input, both for C and Be divertor tiles with T_{tile} = 50°C and T_{wall} = 250°C. These values are comparable to previous JET results for a Be coated machine, with walls at 250°C or 320°C. A detailed analysis of the dependence of the gas recovery on the wall temperature showed that at lower temperature less gas is recovered. This is consistent with the measured D inventory in the JET divertor tiles, determined by post mortem analysis [3]. The D inventory in the X-point tiles is greater than in 1991/92, even though the tile surface was a similar composition. It is believed that the factor that makes the difference is the lower temperature of the tiles.

In figure 3, the gas recovery is plotted as a function of the gas input, for pulses run with and without the cryopump, both for disruptive and non disruptive plasmas. The analysis of the gas released after non disruptive plasma pulses shows no appreciable difference between the case with C and Be divertor tiles. This is in agreement with the observation that no significant change in main plasma parameters and fuelling efficiency was observed between C and Be [4]. One reason why the gas release with C tiles is almost the same as with Be tiles can be that the near-surface layer of the exposed wall is, in both cases, a mixture of C and Be. Such a mixture is produced by the periodic conditioning (with Be evaporation and GDC) and by plasma-wall interactions.

When the cryopump is at LHe temperature (cryopump on), the gas released to the GCS is between 5 to 10 times lower than for pulses without cryopump.

For the cryopump off cases, an enhanced release of gas after disruption is observed. The gas recovered is higher than after non disruptive pulses. This is not the case when the cryopump is cooled at LHe temperature. This can be due to three concurrent causes:

1. The cryopump acts as a strong sink during plasma pulses and less fuel is retained into the walls. 2. The cryopump is pumping the excess gas after the disruption. 3. The wall is depleted in-between pulses more than when the cryopump is off because in the latter case the total pumping speed is lower.

The wall retention after 600 s from the plasma pulse is shown in figure 4. The two cases with and without cryopump are compared.

The net wall retention was calculated from the equation:

$$R_{wall} = Gas_{input} - [Gas_{out}(GCS) + K_{cryo} \times Gas_{out}(GCS)\ ] - Gas_{cryo}$$

$$Gas_{cryo} = S_{cryo} \times \int P_{cryo}(t)\ dt$$

The estimated uncertainty in the calculation of R_{wall} is ± 50%.

$Gas_{out(GCS)}$ is the gas exhausted from the vessel and measured by the GCS. K_{cryo} represents the ratio between the gas pumped by the cryopump and the gas going to the GCS in a 600 s period after pulses. Gas_{cryo} is the amount of gas pumped by the cryopump during the discharge, P_{cryo} the pressure at the cryopump and S_{cryo} the cryopump pumping speed [5].

Globally, within the experimental errors, the increment to the net D wall inventory, after plasma pulses run with the divertor cryopump on, is close to zero for most of the discharges. This result would explain why the amount of gas released from the machine after a disruption is not larger than the gas released after a non disruptive plasma (see figure 3). The apparent wall retention was calculated not including the cryopump effect during plasmas (Gas_{cryo} = 0). The apparent wall retention is much higher than the net wall retention, showing that the particle removal during the X-point phase of the pulse is dominant over the particle removal by thermal outgassing after the plasma.

The net wall retention at low input gas, for pulses with the cryopump on, is generally lower than for the cryopump off case. The discharges with highly negative wall retention (i.e. high wall depletion) at low gas input are identified to be ELMy H-mode, NBI fuelled with an extended X-point phase, during which the recycling gas is compressed into the divertor and efficiently removed by the cryopump. Net wall depletion occurs also at high gas inputs, for long high density L or H-mode plasmas, which are characterised by high neutral pressure in the divertor. This result is in agreement with the observation that the amount of gas pumped by the cryopump during pulses with ELMs or at high density can equal or exceed the gas input [5].

3.2. Gas balance measurements with nitrogen seeding

Nitrogen seeding was used at JET to obtain high radiation in the divertor region and consequent cooling of the plasma reaching the divertor target plates.

From the analysis of pulses run with the cryopump on, it is observed that the output gas (collected over a 600 s period) is further enriched in nitrogen, when compared to the gas input (mixture of nitrogen and deuterium). One explanation is that during the pulse more deuterium is pumped in proportion to nitrogen. This is, nevertheless, in contrast to the result that the composition of the gas in the divertor chamber during the plasma is the same as the input gas [6]. A possible explanation is that the thermal desorption rate after the pulse is higher for nitrogen than for deuterium. This needs further investigation.

4. CONCLUSIONS

1. When the divertor cryopump is off, the results of the gas balance and short term wall retention are in good agreement with results found in previous JET campaigns (1989-92) for a Beryllium coated machine, both for C and Be divertor targets tiles.

2. The cryopump reduces the wall retention after pulses. This implies a low D (and T) inventory, despite the large fuelling required to maintain a set plasma density when the cryopump is on.

3. It is observed that long ELMy H-mode pulses, run with low input gas and NBI heating, deplete the wall from the deuterium reservoir. Net wall depletion occurs also during long high density near detachment L-mode plasmas.

4. For pulses with nitrogen seeding the measured composition of the output gas is different from the input gas, and in particular is enriched in nitrogen.

REFERENCES

[1] R Sartori et al., Journal of Nuclear Materials 176&177 (1990) 624-629.

[2] P Andrew & M Pick, Journal of Nuclear Materials 220-222 (1995) 601-605.

[3] P Coad et al., 14th PSI Conf., France, 1996 to be published in Journal of Nuclear Materials.

[4] D Campbell et al., 14th PSI Conf., France, 1996, to be published in Journal of Nuclear Materials.

[5] G Saibene et al., Europhysiscs Conf. Abstract, vol19c(IV), 1995 465-468.

[6] J Ehrenberg et al., 14th PSI Conf., France, 1996 to be published in Journal of Nuclear Materials.

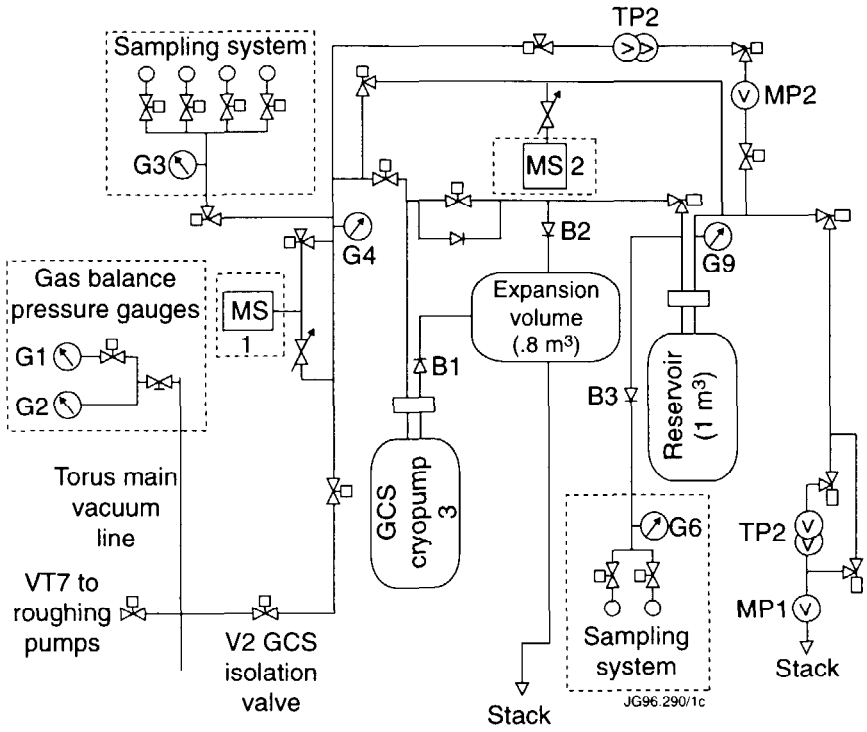

1 – Mass spectrometer for oxygen monitoring
2 – Mass spectrometer for chemical analysis
3 – GCS cryopump (700 barl maximum capacity)
4 – Non return valve (.5barg)

B1 – 5bar bursting disk
B2 – 1.3bar bursting disk
B3 – 5bar bursting disk

G1 – 1mbar Baratron
G2 – 100mbar Baratron
G3 – 1000mbar Baratron
G4 – 1mbar Baratron
G6 – 1000mbar Baratron
G9 – 1000mbar Baratron

TP – turbopump
MP – membrane pump

Fig.1 Layout of the JET New Gas Collection System

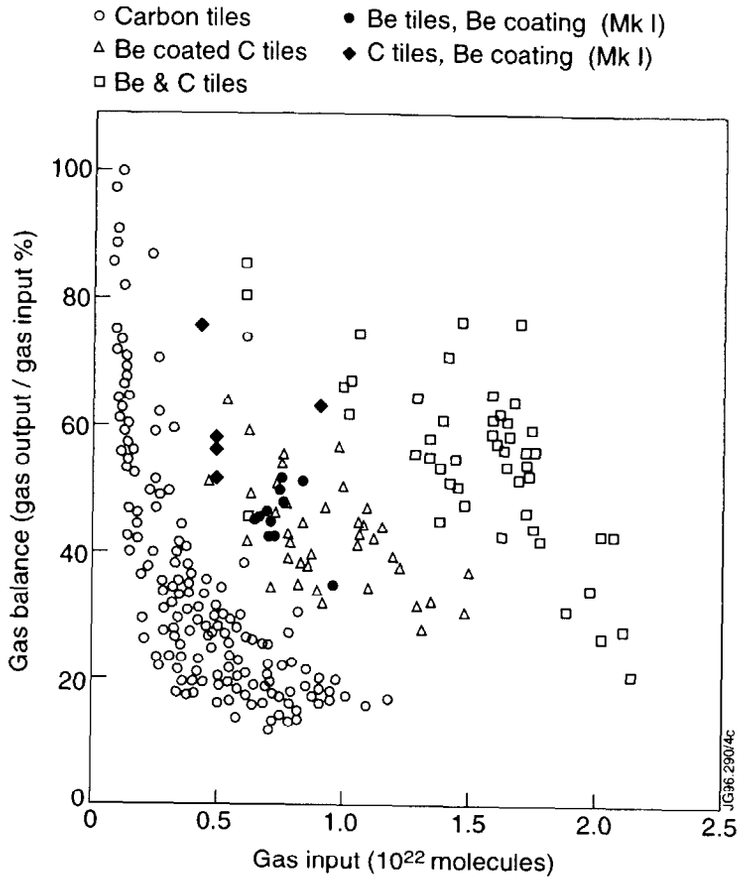

Fig. 2 JET data on the recovery of gas during a 600 s period after the discharge (T_{wall}=250°C and T_{wall}=320°C)

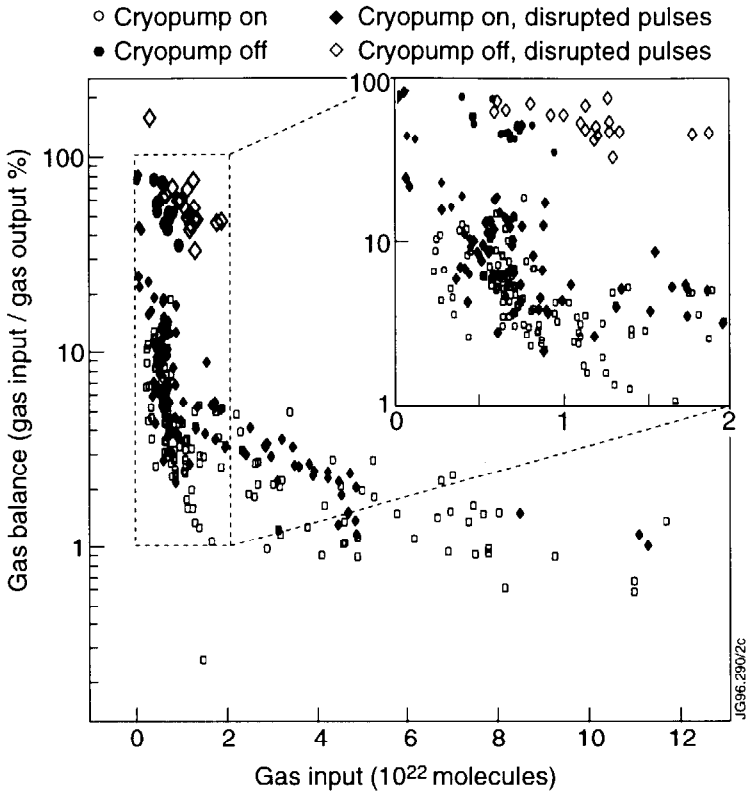

Fig. 3 JET data on the recovery of gas during a 600 s period after the plasma (T_{wall} = 250°C) during the JET MARK I campaign 1994/95. Comparison divertor cryopump on/off.

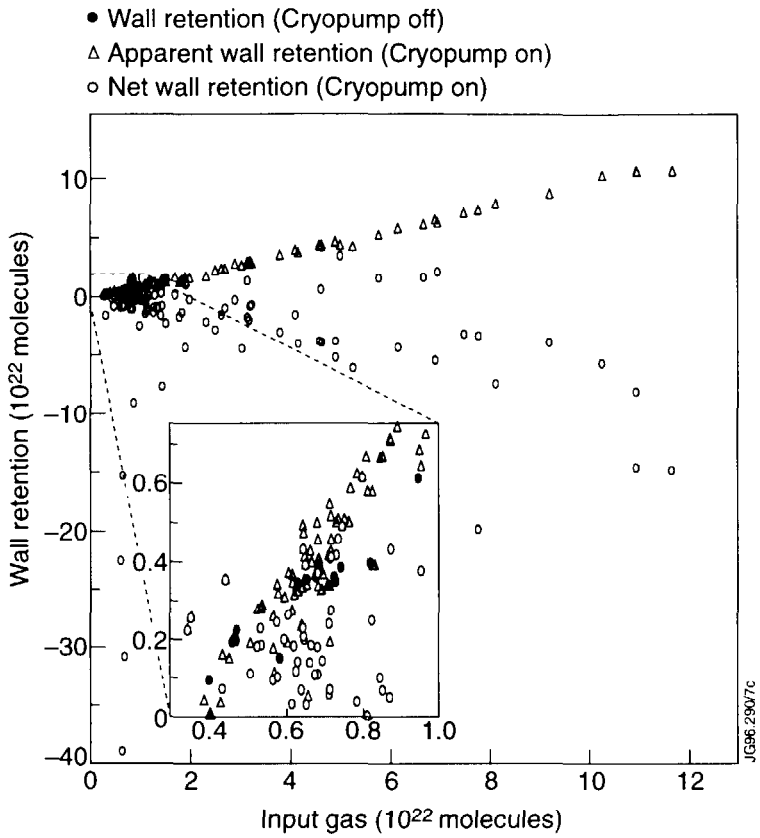

Fig. 4 JET data on the absolute wall retention after 600 s from the plasma pulse for non disruptive pulses. Comparison between divertor cryopump off (± 10%) and on case (± 50%).

A Predictive Study of the JET Mark II Gas Box Divertor

R Simonini, G Corrigan, G Radford, J Spence, A Taroni, G Vlases

JET Joint Undertaking, Abingdon, Oxon, OX14 3EA, United Kingdom

INTRODUCTION

A principal aim of divertor studies at JET is to develop and verify solutions that are relevant for ITER power exhaust and particle control. The Mark II GB divertor was designed specifically to test the ITER Gas Box concept, and is due to begin operation in mid 1997.

The Mark II GB divertor incorporates a flexible design which allows several configurations to be tested. These include horizontal and vertical targets, and an optional septum of as yet unspecified conductance to neutrals. A third possible variant is one which uses a broad, opaque septum to form a double slot divertor.

The EDGE2D/NIMBUS [1] modelling reported in this paper was undertaken to compare the various configurations from an overall performance standpoint.

The perpendicular transport model used is $D_\perp$=0.5 m^2/s, v_{pinch}=7.5 m/s, $\chi_i = \chi_e$ = 1 m^2/s , constant in space, which has been shown to give reasonable simulations of attached L-mode JET plasmas. The Monte Carlo package contains a detailed model of the divertor volume, and includes pumping and by-pass leakage.

EFFECT OF SEPTUM ON A RECYCLABLE IMPURITY

We consider first the case of a deuterium plasma seeded with nitrogen, assumed to be fully recycling. The results are obtained for an equilibrium configuration (I_p=4.5MA), with vertical targets. Fig. 1 shows parts of the computational mesh adopted, with details of the divertor region. In the model, the vessel and the divertor are made of carbon, while the sub-divertor region is made of iron. Sputtering of wall material is inhibited for the runs with nitrogen. We have performed scans of the density at the separatrix mid-plane, n_s, and impurity radiated power, P_{rad}. The required level of P_{rad} is achieved by changing the content of nitrogen through gas puffing. The pumping efficiency of the cryopumps is taken to be 20% for both deuterium and nitrogen. The conductance of the divertor wall to neutrals has been estimated by Monte Carlo calculations [2]. Neutrals entering the by-pass leaks are re-injected at the bottom of the main chamber, while the pumped deuterium is fed back into the SOL from the top of the vessel. Ions diffusing outside the computational mesh toward the vessel are assumed to be transported along field lines and recycled near the divertor shoulders. Boundary conditions at the edge of

the computational domain toward the walls are $\nabla_{\perp}T=0$ and decay length of $\lambda_n=2.5$ cm for temperature and density, respectively.

Table 1 shows relevant parameters for comparing the effects of the presence and shape of the septum for separatrix density $n_s=2\times10^{19}$ m^{-3}, input power $P_i=P_e=5$ MW uniformly into the edge, and impurity radiated power $P_{rad}=6$ MW.

None of the three configurations seems to have a clear advantage over the others. The small differences listed in Table 1 tend to disappear or even change direction at lower density such as $n_s=1\times10^{19}$ m^{-3} or at lower radiation power. Note that the distribution of the radiated power, as expressed by the fraction $P_{rad,sol}$, does not mirror the impurity density distribution (N^z_{sol}/N^z_{tot}) because of the limited temperature range where radiation is effective.

Table 1. ns=2×1019m-3, Pi=Pe=5MW, Prad=6MW, recycling Nitrogen

Symmetry indicators (SOL averages)

Septum	p_{up} (Pa)	$T_{e,up}$ (eV)	p_{out} (Pa)	$T_{e,out}$ (eV)	p_{in} (Pa)	$T_{e,in}$ (eV)
none	292.8	40.5	87.3	5.9	12.5	1.0
opaque	291.2	40.1	85.2	5.7	16.6	1.2
deep V	297.1	40.7	77.2	4.4	39.8	2.1

Particle and power balance

Septum	N^z_{sol}/N^z_{tot} (%)	S^z_{sol}/S^z_{tot} (%)	$P_{rad,sol}$ %	$Z_{eff,max}$ (sol)	N_z/N_i (%)	$\Gamma^{0,i}_{pump}$ ($10^{21}s^{-1}$)	$\Gamma^{0,z}_{pump}$ ($10^{19}s^{-1}$)
none	66.1	12.1	22.3	1.8	0.92	4.0	7.6
opaque	67.2	7.7	17.3	1.7	0.86	4.0	7.6
deep V	74.1	6.1	17.0	1.8	1.19	4.0	15.4

EFFECT OF SEPTUM ON THE INTRINSIC IMPURITY CARBON

In this case, carbon is produced by sputtering. The dominant process is chemical sputtering, for which we have used the model of Ref.[3]. Fig. 2 shows Z_{eff} along the separatrix for the three cases of septum out, septum in, deep V, for $n_s=2\times10^{19}m^{-3}$ and $P_i=P_e=5$MW.

The difference in Z_{eff}, due to additional material sputtered from the carbon structure in the private region, influences the approach to detachment, as illustrated in Table 2. While the mid-plane temperature is nearly the same for the three configurations (about 40 eV), the carbon concentration N_z/N_i increases from 3.7% to 8.8% to 19%, and radiation from 6 MW to 8 MW to 9 MW. In the deep V case, the plasma is fully detached. Note that even though the content of C is much higher, the radiated power is not much higher, again a consequence of the narrow

range of temperatures effective for radiation. A fully detached plasma may not be useful since the SOL becomes more and more transparent to neutrals.

Table 2. Approach to detachment induced by carbon, $n_s=2\times10^{19}m^{-3}$, $P_i=P_e=5MW$

Septum	Γ^i_{target} (10^{23} s^{-1})	$P_{c,target}$ (MW)	$P_{H,rad}$ (MW)	$P_{H,cx}$ (MW)	P_{rad} (MW)	N_Z/N_i (%)
none	3.1	2.4	0.3	0.8	6.3	3.7
opaque	1.7	0.8	0.3	0.5	8.0	8.8
deep V	0.9	0.4	0.2	0.4	8.8	19.4

However, these results depend drastically on the model assumed for chemical sputtering, which is subject to large uncertainties. We have assessed the effect of reducing chemical sputtering by a constant factor. In particular, for the sake of comparison with nitrogen, we have reduced the sputtering yield for carbon to 57% of that given in Ref.[3] so as to radiate 6 MW. While most parameters barely differ, there is a difference in the level of impurities necessary to radiate the required power (N_z/N_i equals 0.86% with N and 3.6% with C), and the density distribution is also different (N^z_{sol}/N^z_{tot} equals 67% with N and 38% with C). This is due, at least in part, to the broader radiation efficiency of N as a function of temperature.

The carbon sputtered from the main chamber is not the main cause of SOL contamination. When the sputtering is artificially switched off everywhere except in the divertor, in the case of no septum P_{rad} decreases from 6.3 MW to 5.9 MW, the impurity concentration from 3.7% to 3.3% and the maximum of Z_{eff} from 2 to 1.8.

VERTICAL VS. HORIZONTAL TARGETS

Another geometrical configuration being considered is that with horizontal targets (Fig. 3), for which again the septum makes little difference. It is found however that the horizontal configuration tends to enter less easily into the regime of detachment than the vertical one, by requiring a larger amount of seeded impurity to radiate (1.3% vs. 0.86% for $n_s=2x10^{19}$ and $P_{rad}=6MW$ with opaque septum), since the recycling of D neutrals from the vertical targets toward the separatrix tends to produce a wider region where radiation is effective. As a consequence, the larger amount of seeded nitrogen required in the horizontal target configuration produces Z_{eff} = 2.0 at the outer mid-plane at the separatrix, whereas Z_{eff} =1.7 in the vertical one.

The vertical configuration has also the obvious advantage of a wider spreading of the heat load over the target plates. This is especially important at high power. Fig. 4 compares the heat loading along the outer target for $n_s=2\times10^{19}m^{-3}$ and $P_{rad}=3$ MW. We note that the ratio of peak

heat loads between the horizontal and vertical targets is worse than that expected from the consideration of the change in wetted target surface alone.

CONCLUSIONS

For given n_s and P_{rad}, the presence or the shape of the septum does not influence appreciably most hydrogenic plasma parameters. For a recycling impurity introduced to increase radiation, the septum details likewise have little effect on impurity content. The shape of the septum does affect, however, the content of an intrinsic impurity such as carbon, affecting the approach to detachment and core contamination. Little difference is found between carbon and nitrogen for fixed P_{rad}, except for the fact that more C than N is required to radiate the same amount. There is not enough D flow, resulting from pumping and leakage, for impurity entrainment in the divertor, the low level of C retention, in particular, being mainly due to transport and not to the sputtering from the vessel wall outside the divertor. These conclusions hold for both vertical and horizontal targets, but in addition the horizontal targets have to sustain a much higher peak heat load. In any case, no solutions have been found with simultaneous detachment, high radiated power fraction and retention of impurities for Mark II GB in JET.

REFERENCES

[1] R Simonini, G Corrigan, G Radford, J Spence, A Taroni, Contrib. Plasma Phys. 34(1994)368

[2] E Deksnis, private communication

[3] A Pospieszczyk, et al., Proc. 22nd EPS Conf. 19-II(1995)309

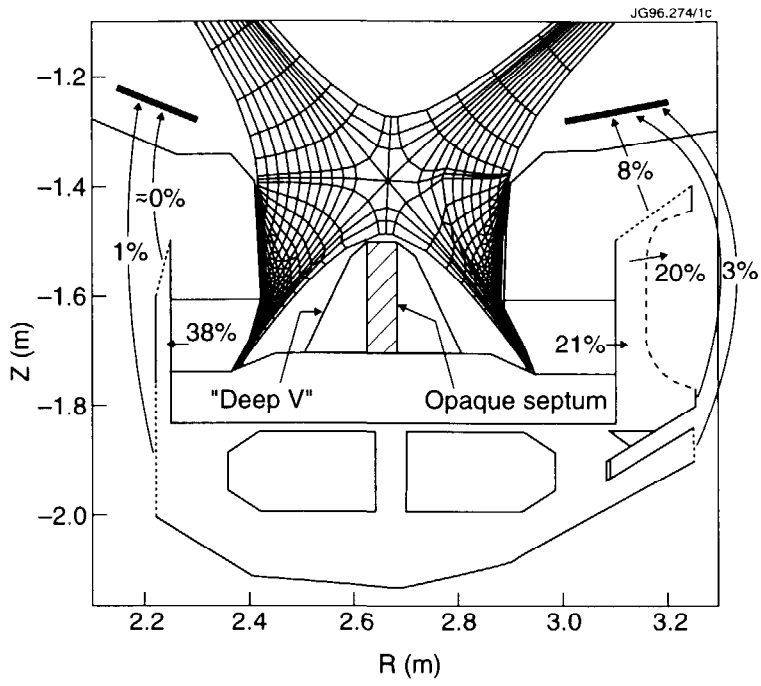

Fig.1. Vertical GB geometry, showing the three septum configurations, pumping and leakages

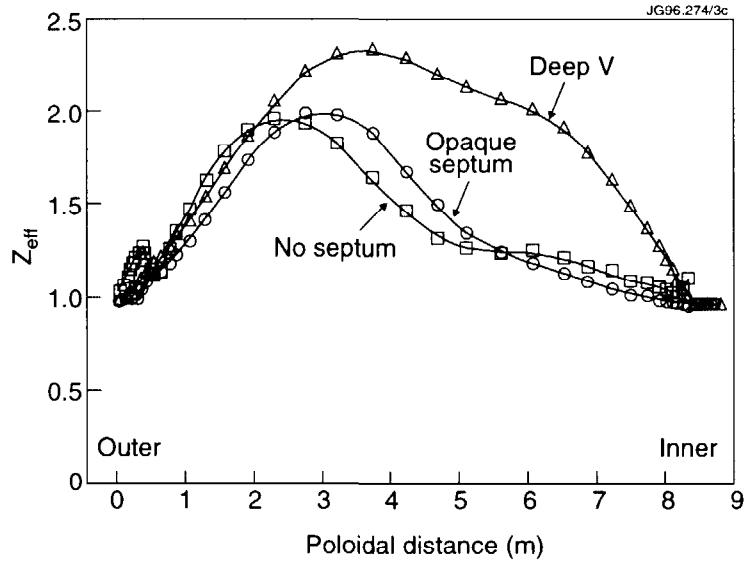

Fig.2. Poloidal profiles of Z_{eff} at separatrix with carbon as the radiating impurity for the three septum configurations. $n_s=2\times10^{19}m^{-3}$, $P_i=P_e=5MW$

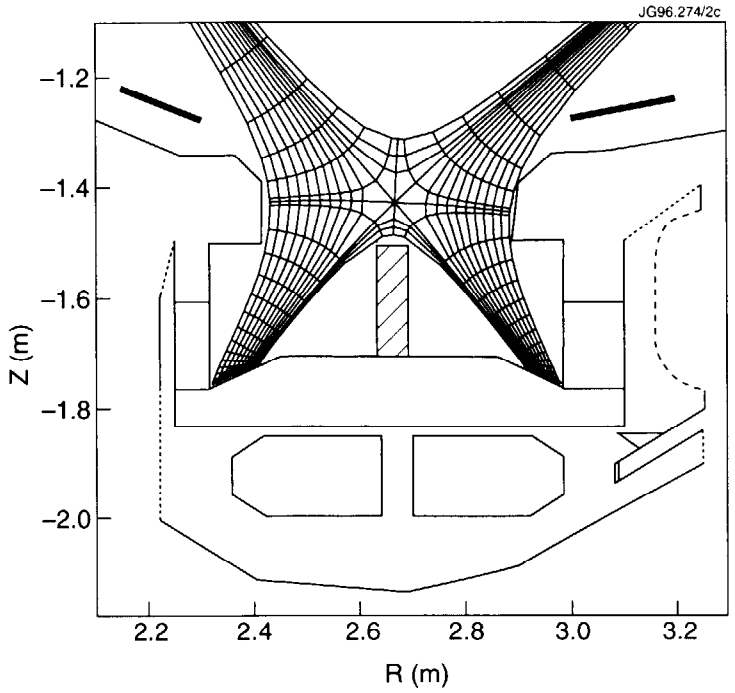

Fig.3. Horizontal GB divertor configuration

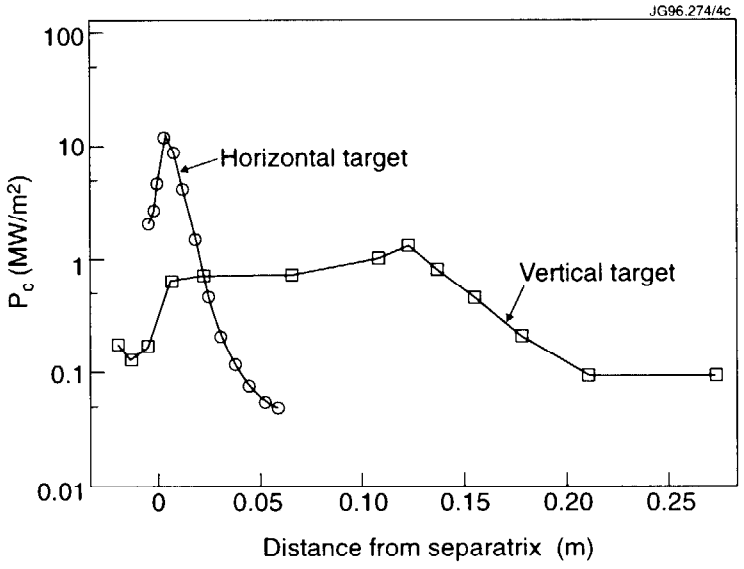

Fig..4. Heat loading on the outer divertor plate for the vertical and horizontal configurations, with nitrogen, $n_s=2\times10^{19}m^{-3}$, $P_i=P_e=5MW$, $P_{rad}=3MW$

Transport Modelling with a Combined Core and Edge Code

A.Taroni, A.Cherubini, G.Corrigan, H.Guo, G.K.McCormick, G.J.Radford,
R.Simonini, J.Spence, E.Springmann

JET Joint Undertaking, Abingdon, OX14 3EA, United Kingdom

INTRODUCTION

Transport of energy and particles in Tokamaks is usually studied separately for the region inside the last closed flux surface (separatrix) and for the edge region. This implies that modelling of the plasma core is replaced by boundary conditions in edge transport codes and modelling of the plasma edge is replaced by boundary conditions in core transport codes.

However there are problems where such a splitting can be inadequate and it would be desirable to study transport in a global way, from the centre to the divertor targets. Examples of such problems are the L-H transition, ELMs, and other phenomena that appear to imply sudden modifications of transport coefficients over a wide plasma region correlated to modifications of the plasma edge [1].

On a longer time scale, of the order of the energy or particle confinement time, or even in steady state, transport studies in the plasma core can benefit from a global approach. This happens each time that particle and energy source or sink terms cannot be accurately measured or simulated without properly simulating the plasma edge. Examples are transport of hydrogen isotopes in all regimes and evaluation of charge exchange losses in the hot ion regime[2].

NUMERICAL APPROACH

In developing the JET code for global transport studies we aimed to include all features routinely used in $1^1/_2$D core transport codes and 2D edge transport codes, such as sophisticated transport models for the plasma core, proper evaluation of power input terms, connection to existing data bases and well developed post-processors for the analysis of results and quantitative comparison with experiments. Another important requirement was the possibility to simulate transients on any time scale of interest without a big overhead in computer time.

Such considerations led us to couple the $1^1/_2$D core transport code JETTO to the EDGE2D/NIMBUS plasma/neutrals 2D transport code for the edge, by means of an adaptation of the so called fractional steps technique.

In essence the method reduces to enforcing continuity of density and temperatures (n, T_e and T_i), and of the corresponding total particle and energy fluxes (Φ, Q_e and Q_i) at a chosen

interface, by imposing proper boundary conditions to each code at each time step. Namely, in JETTO:

$$n_J^n = n_E^{n-1} \quad , \quad T_{e,J}^n = T_{e,E}^{n-1} \quad , \quad T_{i,J}^n = T_{i,E}^{n-1}.$$

In EDGE2D/NIMBUS:

$$\Phi_E^n = \Phi_J^{n-1} \quad , \quad Q_{e,E}^n = Q_{e,J}^{n-1} \quad , \quad Q_{i,E}^n = Q_{i,J}^{n-1}.$$

Here the superscript n indicates the time step, while the subscripts E and J refer to the codes and poloidal averages of the quantities are used at the interface in EDGE2D/NIMBUS.

Continuity of neutral profiles and fluxes is also enforced in order to have a consistent evaluation of particle sources.

Other combinations of boundary conditions are possible and have been tested. The important point is that at the interface one code receives a variable or flux from the other and gives back the corresponding flux or variable. This procedure ensures continuity of all relevant quantities with sufficient accuracy by simply running both codes with time steps typical of EDGE2D/NIMBUS, avoiding extra iterations at each time step. As a result the coupled code is very robust and requires less than 10% additional computer time with respect to the stand alone EDGE2D/NIMBUS.

A series of tests showed that transients related to initial conditions not properly matching at the interface are washed out on a time scale shorter than the typical time τ_{sol} required by the Scrape Off Layer (SOL) to reach steady state in EDGE2D/NIMBUS runs ($\tau_{sol} \approx 30$ ms for typical JET discharges). The time evolution following these transients is consistent with the time scales expected from SOL and core physics. Moreover, large differences in the initial conditions of the SOL, which correspond to small differences in the initial conditions of the global problem, result in small differences at the interface and in the global solution after a time $\approx \tau_{sol}$. This is consistent with the overall problem being well posed and numerically stable. Therefore transients with a fast evolution (time scale $\leq \tau_{sol}$) require a pre-run of the coupled codes to obtain properly matching steady state or quasi-steady state (i.e. changing on a time scale of the order of the global confinement times) initial conditions. On the other hand transients on a time scale $> \tau_{sol}$ can be studied starting from initial conditions not accurately matching at the interface.

Very slow plasma evolution, on the time scale of the core energy or particle confinement time, and steady state situations can be studied assuming that the edge region follows a series of quasi steady states. These are obtained by running the coupled codes for relatively short time intervals ($\approx\tau_{sol}$) at chosen times during the evolution of the plasma core.

EXAMPLE OF MODELLING WITH THE COMBINED CODE

As an example of the application of the combined code in a non stationary situation we present results of a simulation of the ohmic phase immediately following the X-point separatrix formation and preceding neutral beam injection in the JET shot 32919.

During this phase, lasting about half a second and normally preceding JET hot ion H-modes, the average plasma density $<n_e>$ strongly decreases (fig. 1) supposedly due to particle absorption by the divertor targets.

In our simulation the particle absorption has been modelled by imposing a difference between the outgoing plasma flux and the influx of neutrals at the targets approximately equal to the rate of change dN/dt of the core plasma particle content N. The corresponding absorption rate $\approx$ 1.4 10^{21} s^{-1} (out of $\approx$3.5 10^{22} s^{-1} ions reaching the divertor targets) is about ten times larger than the flux of neutrals to the divertor pump, as computed by NIMBUS.

This very crude model, which does not take into account the actual dynamics of the particle absorption nevertheless gives a reasonable simulation of the $<n_e>$ evolution (Fig. 1).

For the energy transport model in the core plasma (from the centre to the interface with the boundary region less than 5 mm inside the separatrix) we used a combined Bohm-gyro-Bohm model [1] including a 'non local' dependence of the Bohm-like term on $L_{Tea}=<\nabla T_e/T_e>_{\rho>0.8}$. Results of this model are particularly sensitive to the electron temperature T_{ea} at the interface. This temperature is computed, not prescribed from experimental traces.

We also assumed an empirical effective particle diffusion coefficient D^{eff} which is of the order of the heat diffusivity χ in the central part of the discharge. However the ratio D^{eff}/χ needs to be decreased as the normalised minor radius ρ increases, in order to provide a reasonable simulation of the slope of the experimental density profile with the flux of neutrals across the interface computed by EDGE2D/NIMBUS ($\Phi_0 \approx 4\ 10^{21}\ s^{-1}$). This result could possibly be an indication of an inward particle flux term strongly increasing towards the plasma boundary.

The core boundary values resulting from the model have been used as constant transport coefficients in the region beyond the separatrix. However an explicit inward pinch velocity such that $V/D=15m^{-1}$ had to be added in this region for a proper simulation of the probe measurements reported in [3].

Simulated and experimental values of temperature and density profiles in the plasma core are given in Fig 2. Figs 3 and 4 show computed and experimental values of parallel ion saturation current and electron temperature at the external divertor target.

The power fluxes into the SOL are a result of the simulation ($P_e \approx 0.8$MW and $P_i \approx 1.1$MW) and slowly diminish with time as $<n_e>$ decreases and the electron temperature increases. The density at the interface n_{ea} is also a result of the simulation and it appears to decrease with time together with $<n_e>$. However this implies a decreasing ion saturation current

at the targets, which does not seem to be supported by probe measurements. This result might indicate that in this case D^{eff} should become larger as $<n_e>$ diminishes.

We conclude from the results obtained so far that the combined JETTO/EDGE2D/NIMBUS code is a powerful tool to simulate tokamak discharges in steady state and time dependent situations over the entire plasma cross section, from the centre to the divertor targets.

By eliminating ad hoc (and sometimes 'convenient') assumptions at the interface between core and boundary regions this code provides a very tough and complete test for transport models, including the effect on the boundary of transport assumptions in the core and viceversa.

REFERENCES

[1] V.V.Parail et al., JET report JET-P(95)49, to appear in Plasma Physics and Controlled Fusion.

[2] A.Cherubini et al., This Conference.

[3] G.K.McCormick et al., 12th PSI Conference, St. Raphael, France, 20-24 May 1996.

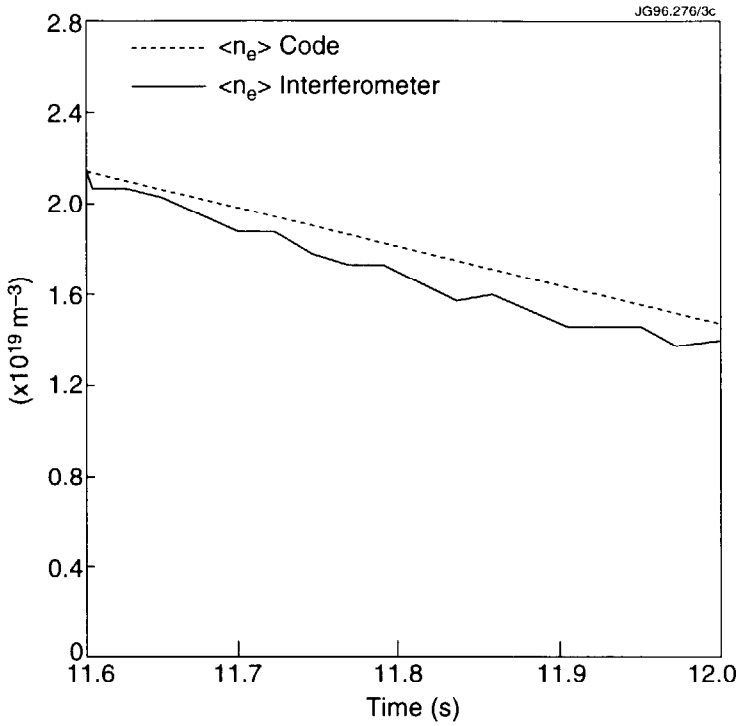

Fig. 1 Experimental and computed time evolution of the average density in JET pulse 32919 before NBI heating.

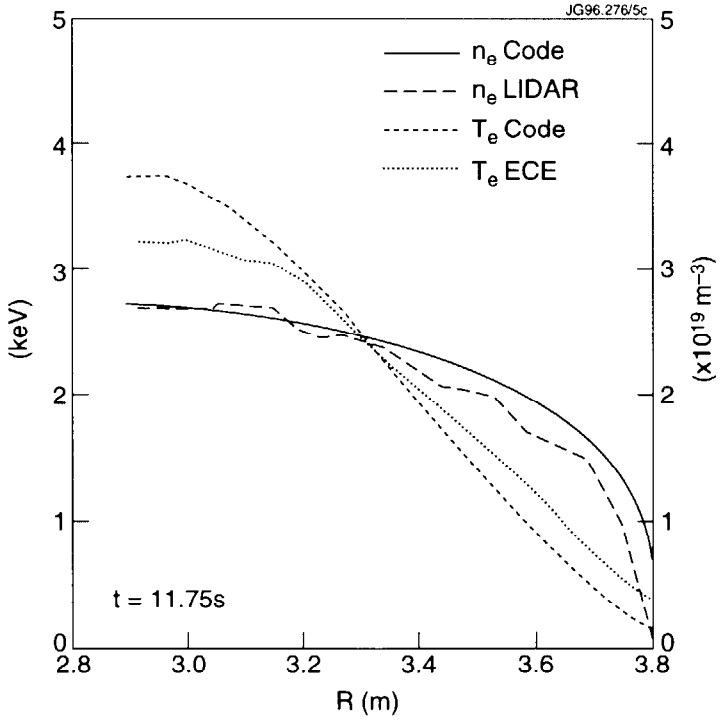

Fig. 2 Experimental and computed electron density and temperature profiles in the plasma core at t=11.75 s.

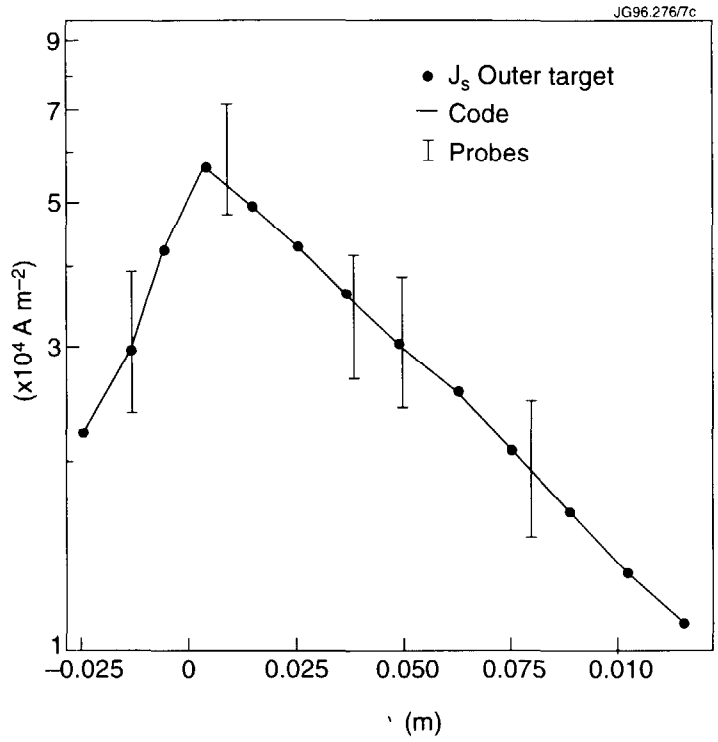

Fig. 3 Experimental and computed ion saturation current at the outer divertor target at t=11.75 s.

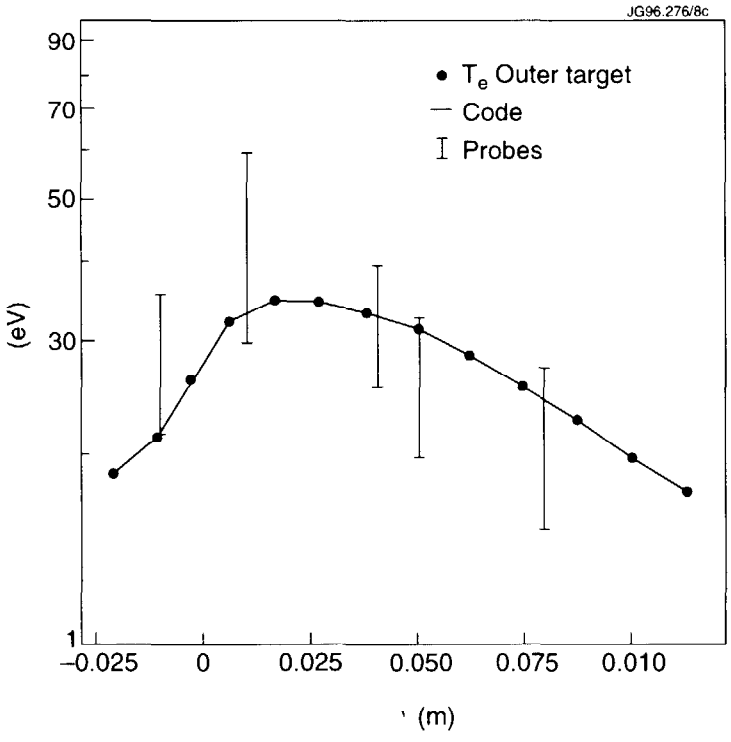

Fig. 4 Experimental and computed electron temperature at the outer divertor target at t=11.75 s.

Ballooning Instabilities in the Scrape-Off-Layer of Diverted Tokamaks as Giant ELM Precursors

R.A.M. Van der Linden, W. Kerner, O. Pogutse, B. Schunke.

Jet Joint Undertaking, Abingdon, Oxfordshire OX14 3EA, UK

ABSTRACT

The linear stability of the SOL to ballooning modes is studied using the reduced MHD model and applying the ballooning approximation to the perturbations. Particular attention is focused on the role of the X-point in the stability analysis and on the potential role of SOL ballooning instabilities as precursors to giant ELMs.

INTRODUCTION

The edge region of tokamaks is a main factor determining the macroscopic behaviour and performance characteristics of the entire plasma. Instabilities in the Scrape-off-Layer (SOL) are believed to generate micro-turbulence leading to enhanced transverse transport. Thus, a quantitative analysis of the stability of the SOL is crucial for understanding phenomena like the L-H transition and ELMs, and for determining the dependencies of quantities like the SOL width on the discharge parameters. In this paper, the stability of the SOL with respect to ballooning modes is studied. Since SOL field lines are open, the periodicity constraint that complicates the ballooning mode representation inside the separatrix is replaced by *`line-tying'* boundary conditions at the target plates. In the ideal MHD model applied here these target boundary conditions might be expected to exert a significant *stabilising influence*. However, on flux surfaces close to the separatrix the X-point effectively shields the plasma from the target plates and removes the stabilising effect. Since the *`magnetic well'* is strongly stabilising *inside* the separatrix and pressure gradients are very large just *outside* the separatrix, the SOL region may become unstable first, acting as a trigger to the release of energy from inside the separatrix.

MODEL

We use orthogonal flux coordinates (ρ, ω, φ) with metric $ds^2 = h_\rho^2 d\rho^2 + h_\omega^2 d\omega^2 + R^2 d\varphi^2$ to describe the magnetic field geometry near the separatrix. Using the reduced MHD equations and the eikonal representation for the perturbations [1]:

$$f(t,\rho,\omega,\varphi) = \tilde{f}(\rho,\omega)exp\left[\gamma t + in\int_{\omega_0}^{\omega} q(\rho,\omega')d\omega' - in\varphi\right],$$

with $nq >> 1$ yields the ballooning equation (here formulated in terms of the electric potential)

$$B_\varphi\left(\frac{B_\omega}{h_\omega B_\varphi}\frac{\partial}{\partial\omega}\right)\frac{1}{B_\varphi}\left(\frac{nq}{h_\omega}\right)^2\left(1+\zeta^2\right)\left(\frac{B_\omega}{h_\omega B_\varphi}\frac{\partial}{\partial\omega}\right)\tilde{\phi} - \gamma^2 c_A^{-2}\left(\frac{nq}{h_\omega}\right)^2\left(1+\zeta^2\right)\tilde{\phi}$$
$$-\frac{\mu_0}{RB_\varphi}\left(\frac{nq}{h_\omega}\right)^2\frac{1}{h_\rho}\left(\frac{1}{h_\rho}\frac{\partial}{\partial\rho}\frac{R}{B_\varphi} - \zeta\frac{1}{h_\omega}\frac{\partial}{\partial\omega}\frac{R}{B_\varphi}\right)\frac{dP_0}{d\rho}\tilde{\phi} = 0,$$

where $q(\rho,\omega) = \dfrac{B_0 h_\omega}{B_\omega R}$ is the safety factor, and $\zeta(\rho,\omega,\omega_0) = \dfrac{h_\omega}{h_\rho}\dfrac{1}{q}\dfrac{\partial}{\partial\rho}\displaystyle\int_{\omega_0}^{\omega} q d\omega'$ is the shear. We can apply the model to an experimental configuration, or use an analytical two-wire current model which allows high accuracy and makes it possible to separate individual effects. The metric coefficients and magnetic field in the (straight) two-wire model are given by:

$$h_\rho^2 = h_\omega^2 = h^2 = \frac{y_0^2}{4}\frac{exp(2\rho)}{\left[1-2exp(\rho)cos(\omega)+exp(2\rho)\right]^{1/2}},$$

$$B_\omega(\rho,\omega) = \frac{B_{\omega 0}(\rho)}{h_\omega R}, \qquad B_\varphi(\rho,\omega) = \frac{B_{\varphi 0}R_0}{R}.$$

The separatrix is located at $\rho = 0$, while the X-point is given by $\omega = 0, 2\pi$. We define the dimensionless quantities

$$\tilde{\beta} = \frac{\mu_0}{B_{\varphi 0}^2}\frac{dp_0}{d\rho} \qquad \text{and} \qquad S_0 = \frac{1}{q(\rho,\pi)}\frac{\partial}{\partial\rho}q(\rho,\pi).$$

Qualitatively, the results obtained for the experimental configuration and for the analytical model are very similar. This is illustrated in figures 1 and 2, where the (dimensionless) growth rate is plotted as a function of ω_0 for typical cases.

The strong variation of the growth rates near the X-point reflects the strong variation of the equilibrium quantities. The characteristic feature that *identical* maximum growth rates are found at three points (one near the midplane and one on each side of the X-point) is due to the non-monotonic behaviour of $\int\frac{\partial q}{\partial\rho}$, as explained in detail in Kerner et al. (1996) [2].

STABILITY ANALYSIS OF THE EDGE REGION IN JET DISCHARGES

Experimentally it has been found that the duration of the ELM-free period can be increased by stronger shaping of the magnetic configuration, as shown in figure 3. This agrees with the higher critical gradient for the ballooning instability displayed in figure 4. It is also clear from figure 4 that $\tilde{\beta}_{crit}$ is lower in the SOL than inside the separatrix.

STABILITY ANALYSIS OF A TWO-WIRE MODEL OF THE SEPARATRIX REGION

In figure 5 the influence of shear on the marginal stability point $\tilde{\beta}_{crit}$ is shown. For small values of ρ we find the linear dependence $\tilde{\beta}_{crit} = a(S_0) + \rho b(S_0)$. Close to the separatrix shear is stabilising, but further out the dependence becomes non-monotonic. Thus the global effect of shear depends strongly on the natural mode width (e.g. due to FLR effect). Not shown here is that shear also affects the position where the most unstable solution is found. When the height of the X-point is varied (keeping the configuration fixed but increasing the distance of the target plates) it is found that close to the separatrix the height of the X-point has no significant effect on the critical gradient, i.e. the target plates are effectively shielded by the X-point (see Kerner et al. for more details). The eigenfunctions indicate that the perturbations of physical quantities (e.g. $\delta B_\rho \sim \frac{\partial^2 \phi}{\partial \omega^2}$, $\delta v_\rho \sim \frac{\partial \phi}{\partial \omega}$) are localised near the X-point.

DISCUSSION

We have shown that the critical gradient for ideal ballooning modes in the SOL is lower than that just inside the separatrix. The X-point has a strong influence on the stability of the SOL (mainly by shielding the upstream plasma from the target plates), and in particular we have found that the perturbations of physical quantities are localised near the separatrix in the X-point region (some localisation near the midplane is also possible). The effect of shear is generally stabilising for modes that are strongly localised (i.e. with narrow mode width), but for larger mode widths shear may destabilise instead. The stability characteristics of the tokamak edge region are compatible with the ELM model proposed by Pogutse et al. [3]. In this model, the ballooning instability in the SOL is conjectured to act as precursor for giant ELMs. Because of the localisation the ballooning instability in the SOL destroys the magnetic X-point geometry and this makes hot plasma from inside the separatrix come into contact with the wall. The thus generated impurity influx then triggers the instability inside the separatrix (the main macroscopic event). Finally, the expelled plasma layers are diffusively refilled. This model leads to an estimate for the ELM frequency

$$f \propto \frac{P_{in} B_0}{I^3 \Delta_P{}^{1/2}}$$

As shown in figure 6, the predicted linear dependence on input power agrees with the experiment. An inverse dependence on input power is also obvious, but the exact scaling needs to be further investigated.

REFERENCES

[1] J. Connor, R. Hastie, and B. Taylor, Proc. R. Soc. (London). Ser. A365 (1979) 1.

[2] W. Kerner, O. Pogutse, R.A.M. Van der Linden and B. Schunke, submitted to Plasma Physics and Controlled Fusion.

[3] O. Pogutse, J.C. Cordey, W. Kerner, and B. Schunke, Proc. 22nd EPS Conf. on Controlled Fusion and Plasma Physics (Bournemouth, 1995), Vol III p.277.

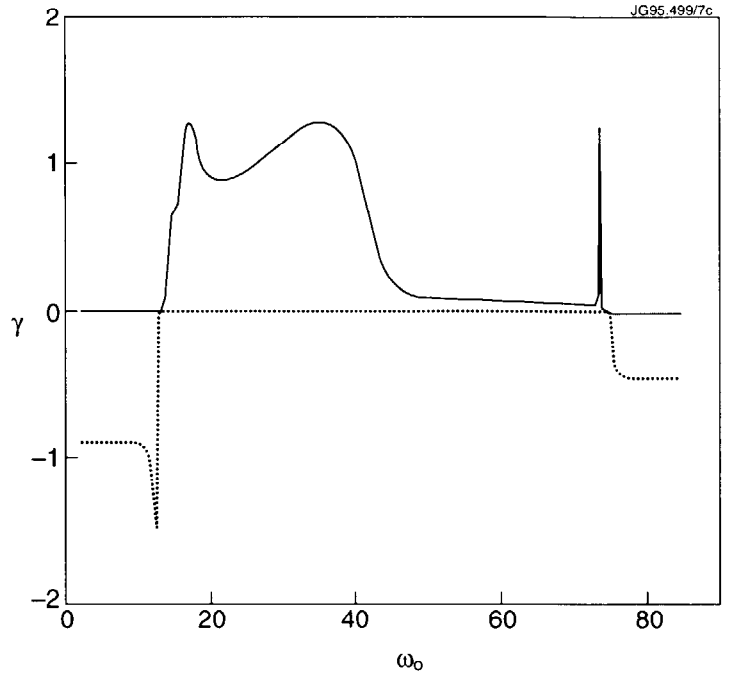

Fig.1: Growth rates for JET experimental configuration (pulse 31300).

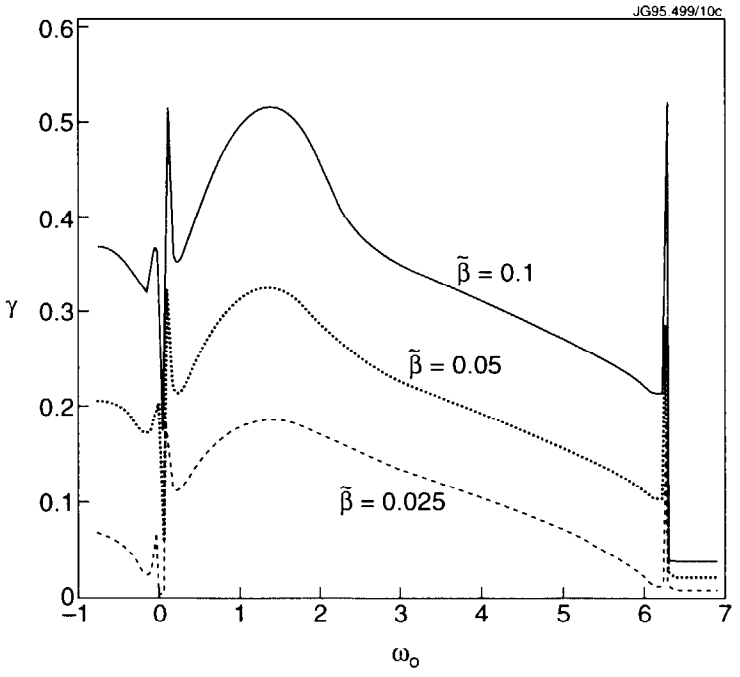

Fig.2: Growth rates for analytical model (S_0=0).

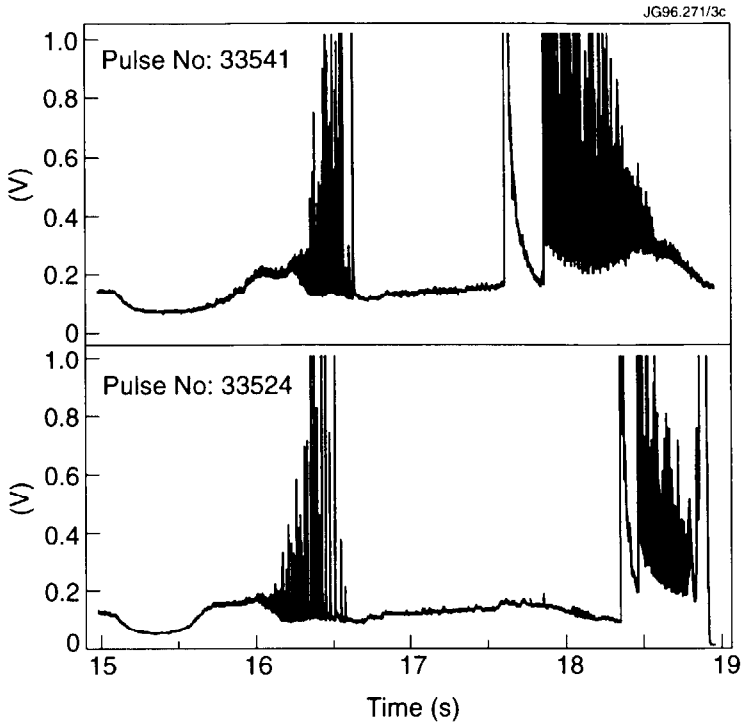

Fig. 3: Elm behaviour of two discharges with different shaping (D_α signal).

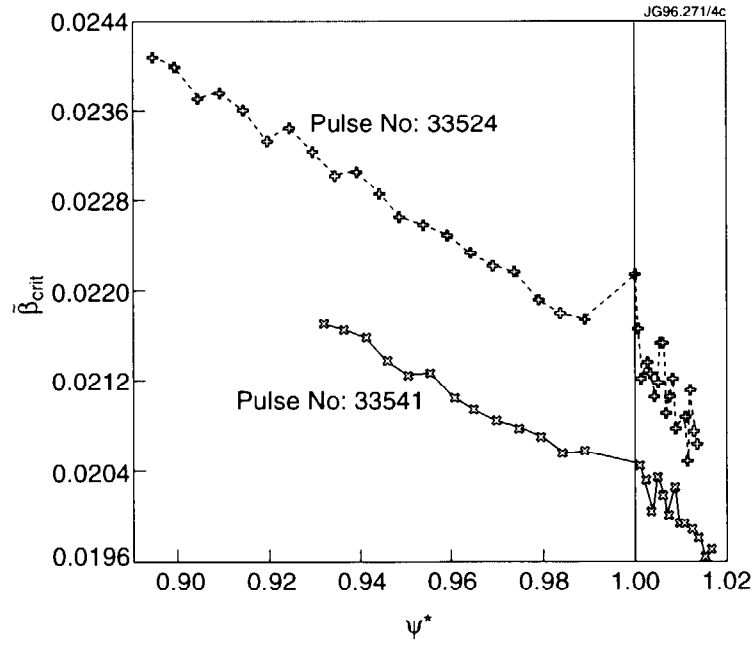

Fig. 4: Calculated $\tilde{\beta}_{crit}$ for these discharges

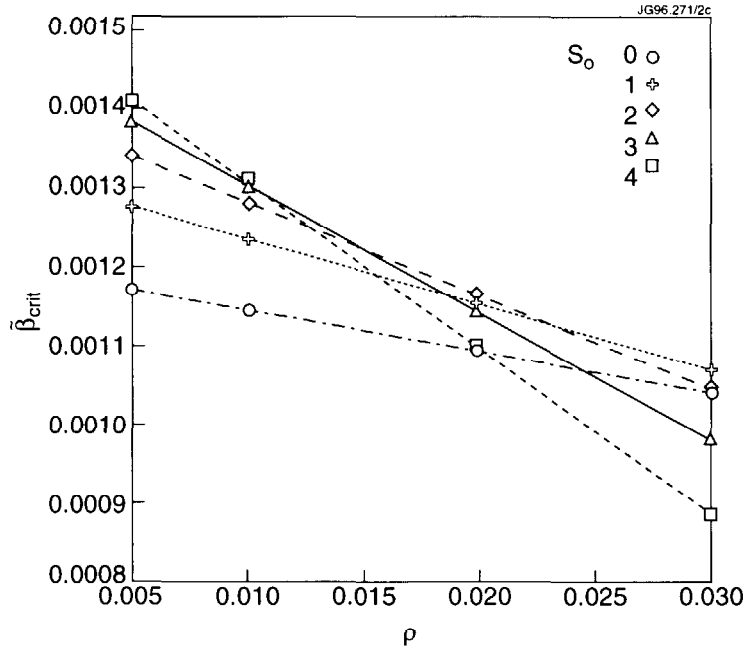

Fig. 5 Dependence of $\tilde{\beta}_{crit}$ on shear S_o

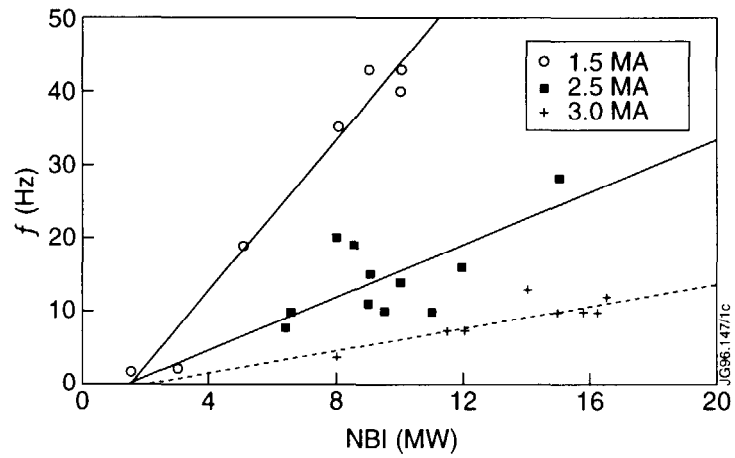

Fig. 6 Experimental dependence of ELM frequency on input power.